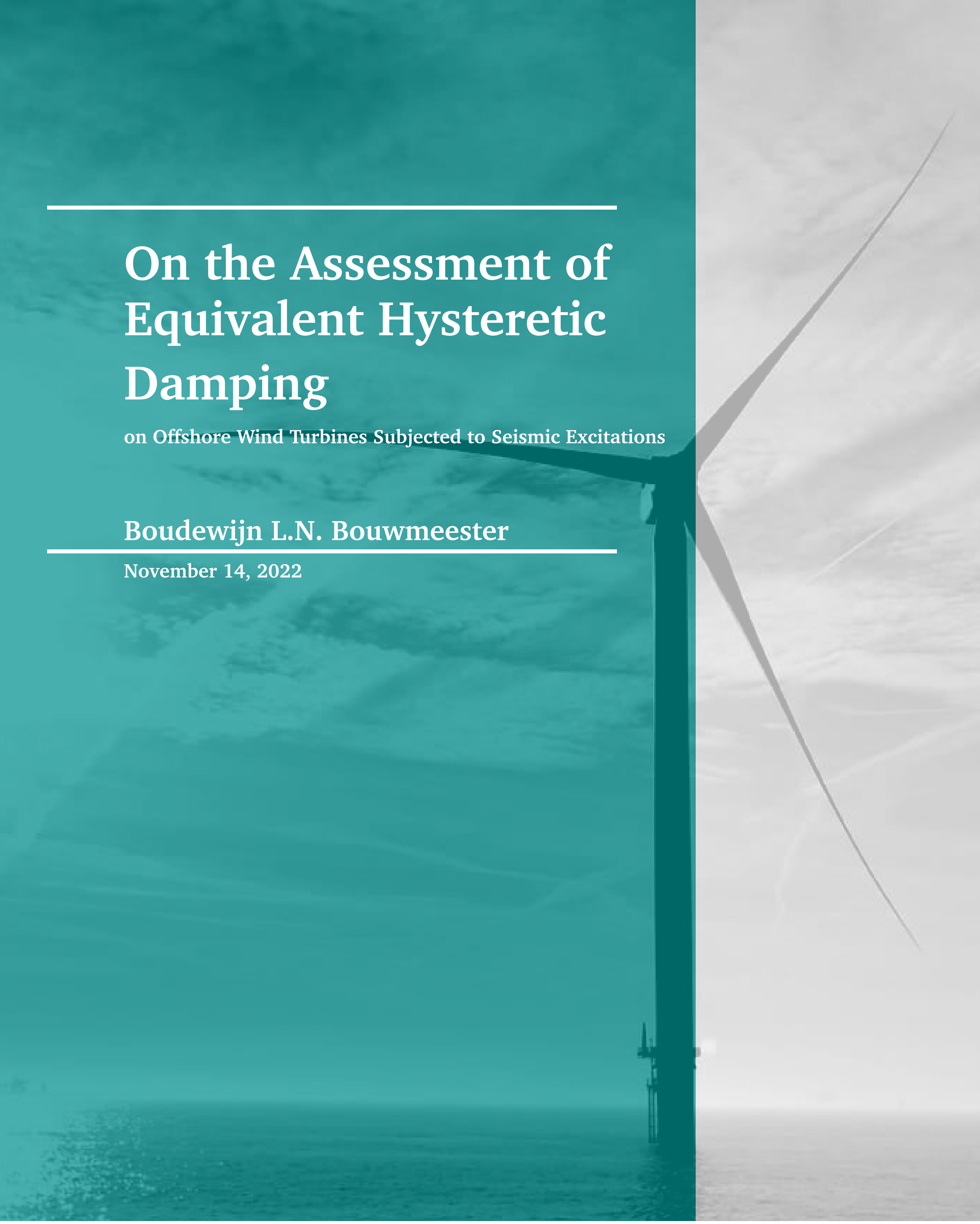

On the Assessment of Equivalent Hysteretic Damping

on Offshore Wind Turbines Subjected to Seismic Excitations

Boudewijn L.N. Bouwmeester

November 14, 2022

On the Assessment of Equivalent Hysteretic Damping on Offshore Wind Turbines Subjected to Seismic Excitations

Master of Science Thesis

Author:	Boudewijn L.N. Bouwmeester	4982215
Committee:	Dr. Ir. A. Tsouvalas	TU Delft - Chairman
	Dr. Ir. F. Pisanò	TU Delft
	Ir. S. Panagoulias	TU Delft & Siemens Gamesa Renewable Energy
	Ir. C. de Winter	Siemens Gamesa Renewable Energy

November 14, 2022

TU Delft Delft University of Technology

SIEMENS Gamesa RENEWABLE ENERGY

Abstract

The increasing global demand of renewable and clean energy has led to the exponential growth, development, and interest in the offshore wind energy industry and expansion towards earthquake-prone areas. Offshore wind turbine structures, typically supported by a tubular monopile foundation, are increasing in size to meet the increasing human demands. In the constant ongoing debate in search of a balance between design accuracy and efficiency, general consensus is yet to be found in search of accurate yet simplified representation of soil-pile interaction. A Winkler foundation principle has shown to be a good compromise regarding this discussion but current knowledge is mainly based on (pseudo-static) small soil-strain inducing wind- and wave load-cases. Adopting this principle, the soil-structure interaction mechanism is represented by local lateral soil reactions (springs with distributed stiffness in mechanical formulation). Strong ground shaking induces shearing and volumetric variation of the soil particles. Through hysteresis the soil material exhibits energy dissipation: *hysteretic damping*. Accounting for hysteresis is considered computationally more demanding than when the soil continuum is assumed elastic but this is an assumption which only holds when soils undergo very small soil strains.

This thesis explores the amount of energy dissipated as a result of hysteresis during seismic response of an offshore wind turbine and the applicability of such damping in a local linear visco-elastic manner. To assess the seismic response, an equivalent one-dimensional Finite Element Model was developed in *OpenSees* [31]. In order to obtain insight in this nonlinear energy-dissipation mechanism associated with the hysteretic offshore wind turbine model under seismic excitation, a Python code was developed that calculates the energy dissipation of each load-cycle separately. The developed energy dissipation assessment algorithm is effective in application of arbitrary hysteretic response and unloading-reloading rules.

The hysteretic nature of the soil-pile interaction springs in question are calibrated against the widely applied *API* [3] *p-y*, force-displacement curves. Unloading-reloading rules are specified to define the load-cycles. Boulanger et al. [5] describes such unloading-reloading rules for pile application under seismic loading and is directly applicable in OpenSees under the name of *PySimple1*. The applicability of these backbone curves and unloading-reloading rules remains questionable in application of rigid monopile foundations. Despite not representing the accuracy of true soil-monopile interaction, obtained results in this research may support the exploration of innovative unloading-reloading rules.

The developed energy dissipation algorithm is proven to be a powerful tool in identifying the amount of energy dissipation over a total timeseries. Reasonable agreement in peak (maximum observed), Ultimate Limit State, deflection and bending moment seismic response at mudline and tower top has been found between a hysteretic supported model and equivalent elastic models using a single (load-dependent and depth-dependent) equivalent damping coefficient in parallel with each soil spring. Representing the hysteretic energy dissipation mechanism using viscous dampers with constant damping coefficients has therefore proven to be an effective modelling strategy to account for the damping mechanism of plastic unloading-reloading rules without accounting for hysteresis. The effectiveness of an equivalent elastic modelling strategy reduces when the response undergoes substantial permanent plastified displacements. A typical property which is unable to be simulated under the application of an elastic modelling strategy.

Acknowledgements

This thesis, with topic proposed by Siemens Gamesa Renewable Energy and further defined in collaboration with Delft University of Technology, is in partial fulfilment of the requirements for the degree of Master of Science in Structural Engineering: department of engineering structures at the faculty of Civil Engineering and Geosciences. It marks the end of my time as a student at Delft University of Technology. This work would not have been possible without the help and expertise of others and therefore I would like to thank a few persons for their collaboration in this work.

First and foremost, I would like to thank my committee members. From the TU Delft side I want to thank Apostolos Tsouvalas and Federico Pisanó. Apostolos, thank you for introducing me into the complex yet interesting world of structural dynamics and structural response to earthquakes. Also, thank you Federico for your input, insightful ideas and helpful guidance.

Special thanks to my daily supervisors at Siemens Gamesa Renewable Energy: Stavros Panagoulias and Corine de Winter. Stavros and Corine, thank you for our weekly meetings and constructive criticism which helped shaping the end result. Thank you for being patient and for comforting me when I was so impatient for results. I want to thank you both but also Col and Pim for being there when I needed most and felt lost during this process. It means a lot to me. I also want to say thanks to Pim, Joris, and Sachin for hosting bi-weekly student meetings which have been very helpful.

Finally, I want to express my gratitude to all my friends and family who I have bored with my - not so easy understandable - research topic. Thank you for your ongoing support and sympathy. And, of course, I want to thank Fleur for your ongoing support. Your admiring enthusiasm and compassion is what kept me going.

Boudewijn L.N. Bouwmeester
Delft, November 2022

Contents

List of Figures

List of Tables

Chapter 1

Introduction

1.1 Offshore Wind

The increasing global demand of renewable and clean energy has led to the exponential growth of development in the offshore wind industry. Because of a smoother overall surface, wind quality is better at sea than on land. Therefore, it ensures a greater and more reliable power production, allowing for the use of larger turbines and is less disturbing for the public. The offshore wind industry is mainly located in North-Western Europe but alongside the increasing demand in clean and renewable energy, the number of proposed and planned wind farms is increasing rapidly. The proposed and planned locations for new offshore wind farms are expanding accordingly towards seismically active regions. While current designs are increasing in height and rotor diameter, the seismic performance of offshore wind turbines still has not been investigated thoroughly. Investigation is thus necessary to reach more reliable and cost-effective design methods for these structures against strong ground excitations.

1.2 Offshore Wind Turbine Support Structures

Figure 1.1 indicates common foundation types supporting the offshore wind turbines. The monopile foundation is by far the most common foundation concept. Its application is mostly justified because it has demonstrated to be an economical choice at shallow water depths [11], it is well suited for mass-fabrication and the installation method, based on conventional impact driving, is robust in most soil conditions [24]. Next to that, the use of tubular sections has its structural advantages due to equal bending stiffness in all directions, fatigue resistance and generally good dynamic behavior.

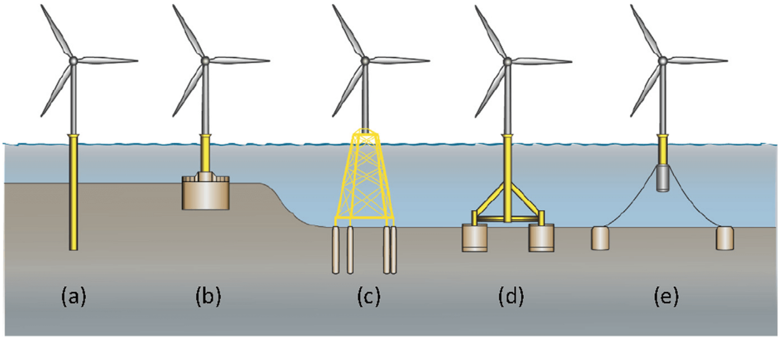

Figure 1.1: Common foundation types used in offshore wind turbine design: (a) monopile, (b) monopod, (c) jacket structure, (d) tripod, (e) floating wind turbine [26].

As the offshore energy market is increasing, wind turbine dimensions increase to meet these increasing demands. Large monopile foundations of about 8m in diameter in shallow waters are currently state of the art [59]. Alongside new proposed larger designs this monopile diameter is gradually increasing and the extension to deeper waters is starting to be made. Since the cost of the monopile foundation could reach levels up to 35% of total cost [26] it is obvious that the monopile foundation design should receive critical attention. Kallehave et al. [24] estimated that by improving the current conventional design methods for offshore wind turbines supported by monopile structures the potential savings can be up to 25% by reduction of steel tonnage. This would mean that better assessment could lead to substantial total cost reduction.

1.3 Design Considerations

Offshore wind turbines are long and slender structures with most mass concentrated at the top (represented by the nacelle, hub, and blades) and are therefore sensitive structures in terms of dynamics. For the North-Western Europe concentrated market it is assumed that environmental loads such as wind- and wave-loads are predominant for the design considerations. Expansion towards seismic prone regions includes earthquake loading as new - possibly dominant - load-case to which the offshore wind turbine is subjected. There exist no detailed guidelines about earthquake design for offshore wind turbines because of the mostly North-Western Europe concentrated current market. There exists only little experience and knowledge of the application of offshore wind farms in seismic active regions and even less about regions probable to strong seismic motions.

Earthquake loads are extremely cyclic and complex. A typical time history of an earthquake acceleration response includes the amplification of many frequencies and many different magnitudes of amplitude. Earthquake ground shaking induces not only horizontal loads through the soil onto the monopile but vertical loads as well. The natural frequencies of the offshore wind turbines in the vertical direction are significantly higher compared to the lateral direction: typically, between 4-7 Hz which often coincides with the (vertical) peak spectral values of earthquakes [26]. This makes them vulnerable even to moderate ground shaking. Vertical ground shaking could possibly be one of the governing design cases as the vertical excitation from an earthquake can produce severe vertical accelerations in the upper parts of a wind turbine [28, 27]. Although horizontal and vertical response is coupled if the seismic loading activates nonlinear soil behavior and can occur simultaneously with wave- and wind-loading, the two directions are often treated as separate design cases.

1.4 Damping

Damping is considered the energy dissipation of a material (or system) under cyclic stress and causes a system to gradually stop moving over time. In fact, a system would oscillate forever once it is excited without any source of damping but, in reality, there almost always exists some damping (energy loss) in vibratory systems. The more damping is present in a system, naturally, the shorter the time to force the system response to become stationary. In most practical situations reference is made towards *viscous damping* which is proportional to the velocity of the mass of the system in question.

1.4.1 Soil Damping

Soil damping is known to affect and reduce both the soil motions as well as the structural response through dynamic soil-structure interaction. Clear guidelines on the application of the amount of soil damping are limited. Derivation on the amount of damping as a result of cyclic nonlinear, plastic/inelastic (hysteretic) behaviour of soils generally relies on simplified sets of unloading- and reloading rules where an overestimation of damping is observed under large soil-strains compared to measurement data. General consensus is yet to be reached for accurate nonlinear unloading-reloading sets in the simulation of soil-monopile interaction because the mechanism is complex and holds many components. Uncertainties increase rapidly when a seismic event is considered. Lastly, nonlinear models are computationally expensive. Industry therefore adopts equivalent linear analyses where the soil stiffness is linearized to be constant. The nonlinear soil damping is then simplified and applied in a linear viscous damping: *equivalent (hysteretic) damping*.

1.5 Motivation & Scope

The understanding of the dynamic response of monopile supported offshore wind turbines subjected to seismic loads is key to reach reliable and efficient designs for the expansion towards areas prone to (strong) earthquakes. Soil-structure interaction is a complex process, especially during strong seismic motions. The dynamic response is best captured using a full nonlinear three-dimensional Finite Element time domain formulation: a continuum model. This formulation requires extensive modelling considerations and is computationally expensive. A one-dimensional Winkler foundation is found to be a reasonable compromise in describing the structural lateral response while notably increasing convenience and computational speed.

Time domain analysis, evaluating and updating the structural response at each (user-specified) timestep, is typically used in practice to determine offshore wind turbine response to a seismic event. Nonlinear uncoupled *P-Y* (pre-defined force-displacement paths) springs along the embedment depth are used in a one-dimensional Winkler foundation to account for the soil resistance. The depth-dependent free-field soil column excitiation as a result of seismic shaking is then imposed onto the supports of the structural model. The accuracy of capturing 3D soil-structure interaction using 1D uncoupled lateral springs is questionable, but its limitations are well documented from which several extensions have been provided to incorporate 3D soil-structure interaction components in a 1D model formulation [51, 7, 4, 49]. One soil-structure interaction component specifically, foundation damping and more specifically: soil hysteretic damping (prone damping component during strong ground shaking), has still not been investigated thoroughly while it is assumed to be capable of significantly alleviating seismic loads. Hysteretic modelling shows great potential in the simulation of unloading-reloading paths (hysteretic loops) while still holding on to the convenient Winkler principle. General consensus is yet to be reached on correct unloading- and reloading rules related to a monopile foundation and simulation of unloading- and reloading paths for every load-cycle in a strong dynamic process can be very time-consuming. Therefore, the use of linear elastic models (unloading-reloading along the same load-path) are generally preferred by the industry and the energy dissipation mechanism is applied in an equivalent manner. Recommended practice [12] prescribes the application of local soil hysteretic damping on offshore wind turbine structures under seismic excitations where a single damping value is representative for the total analysis duration. However, the approach in describing and applying equivalent viscous damping is based on rigorous assumptions and is not tailored to arbitrary load-paths subjected to permanent displacements and unloading- and reloading rules which deviate from recommended practice. No information is obtained of the time-dependent nature of energy dissipation. Knowledge in equivalent elastic analysis with equivalent hysteretic damping for offshore wind turbine structures subjected to seismic excitations remains therefore limited.

Considered the above, the focus will be on the response of offshore wind turbines and in particular on the soil-structure interaction mechanism represented by local springs. The focus lies on the lateral response only and only on the large-strain / displacement regime considering that damping originating from nonlinearities is assumed to be prone. Increasing the reliability of values of soil damping within the large-strain regime will be expected to result in more efficient designs. Yet, this topic has been widely researched throughout literature [14, 36, 2, 23, 29, 44, 52, 55, 58, 61, 60] with focus primarily on innovative sets of unloading-reloading rules and/or initial load paths (so called p-y curves) and will therefore considered to be outside the scope. Furthermore, pore pressure effects like liquefaction will not be considered. In the equivalent 1D model developed to conduct the analyses, the rotor-nacelle assembly and blades are simplified in a single top mass and top inertia where its additional dynamic effects are neglected resulting in no differences in operational state (either idling or operational). At last, the scope is limited on the ultimate limit state of the structure (ULS) leaving the main discussion limited to observed peak response.

1.6 Objective

The application of equivalent damping in support of elastic analyses is currently adopted by the offshore wind turbine industry because general consensus for accurate unloading-reloading rules during strong seismic excitations is yet to be reached and hysteretic modelling tends to be computationally expensive. In-house software of Siemens Gamesa Renewable Energy is no exception to this elastic modelling with an equivalent damping strategy. Either applied on a local spring level or applied on global structural level. However, current strategy of equivalent soil damping is not based on seismic excitations. Because hysteretic modelling is usually omitted completely, investigation is necessary of its implication on the seismic response of an offshore wind turbine structure with main focus on the beneficial soil damping effects. Additionally, more investigation is considered to be necessary to understand the limits and the implication on the dynamic response of an equivalent damping strategy when subjected to seismic excitations.

To increase our knowledge of soil damping in the large-strain regime during a seismic event the main objective of this thesis is therefore to answer the following question:

How to establish an engineering method that assesses soil material damping during seismic motions in the large-strain regime and integrate this into an equivalently damped dynamic offshore wind turbine model?

Achievement of this main goal requires intermediate objectives to be accomplished:

- What characterizes the soil-monopile interaction mechanism and what components are relevant to the soil material damping?

- What is the industry standard approach for soil-pile interaction mechanism and how is soil damping applied?

- How to formulate a one-dimensional model for seismic analysis and how to implement this in a Finite Element model formulation?

- How to capture the amount of dissipated energy by hysteresis and amount of equivalent damping in a nonlinear hysteretic offshore wind turbine model subjected to lateral seismic excitations?

- How does an offshore wind turbine model supported by hysteretic springs compare with a model supported by (linear) elastic springs and equivalent dashpots?

1.7 Outline

In order to answer the aforementioned objectives, this thesis is structured as follows:

- **Chapter 2:**
  Essential theoretical background relevant to an offshore wind turbine supported by a monopile foundation subjected to seismic excitations. The fundamentals of soil modelling, dynamics of hysteretic systems, soil-structure interaction, and the foundation damping mechanism will be discussed based on conclusions drawn by previous research.

- **Chapter 3:**
  Formulation of the time domain 1D distributed Winkler based Finite Element model for seismic analysis. Investigation and calibration of the specific soil-structure interaction element to be used and time incremental lateral response validation.

- **Chapter 4:**
  Description and formulation of equivalent viscous damping and energy dissipation techniques including formulation and validation of the method to be applied based on a single degree of freedom system.

- **Chapter 5:**
  Numerical analyses of the offshore wind turbine model. Eigenproperties of the structure, description of the considered input motions, and performance analysis of the effective equivalently damped elastic models for a single harmonic and seismic load case. In conclusion, the relation towards recommended practice is discussed.

- **Chapter 6:**
  Conclusions, and recommendations for further work.

Chapter 2

Theoretical Background

2.1 Fundamentals of Soil Modelling

Soil globally represents different behaviour under different amplitudes of strain. Therefore, the soil response is generally classified in domains of shear strain amplitude. Earthquake loads are highly cyclic and complex from nature. A typical time history of an earthquake response includes multiple frequencies and multiple different magnitudes of amplitude hence a complex waveform. Under a single seismic input signal, it is therefore no exception that this complex waveform can induce different and multiple ranges of constitutive soil behaviour. The main tools for soil classification is by the means of a shear strain dependent *shear modulus reduction curve*, generally used as direct input in constitutive soil models. The soil resistance is visualized over shear strain amplitude derived from a monotonic *backbone curve* which presents the shear strain versus shear stress response. This typical shear stress-strain relationship is presented hereafter in Figure 2.1. Until the soil reaches its peak shear strength, the shear stress increases with gradual descending rate. This relationship is known as the shear modulus reduction (curve): indicating the soils' secant stiffness over shear strain amplitude.

In the small-strain regime, shear strains (often) less than the linear threshold: $\gamma_l \sim 10^{-5}$, the soil generally exhibits linear elastic behaviour. The shear modulus acts as a constant maximum and damping as a constant minimum: unloading-reloading follows the same path and is linear. In fact, soils undergo volumetric variation and inelastic response even when subjected to small strains. At these low deformations / small strains the nonlinear behaviour of soils remains limited and is therefore

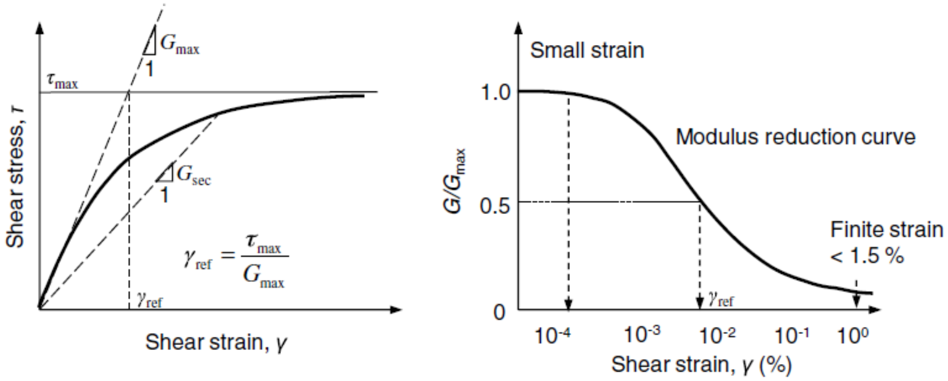

Figure 2.1: Monotonic *backbone* shear response [14].

often neglected (and regarded as elastic). Note that in Figure 2.1 a different range of values is presented than the aforementioned threshold. This already indicates that site-specific soil properties can vary notably and must be carefully evaluated, preferably by means of laboratory testing. For shear strains above the volumetric threshold: generally $\gamma_v \sim 10^{-4}$, the soil exhibits non-negligible volumetric variation. The volumetric variation can induce substantial nonlinearity resulting in different load-paths (divergent of a single backbone relationship) in a non-monotonic load-case. This cyclic, nonlinear, plastic behaviour is often also referred to as hysteresis. Severe consequences of soils undergoing large strain cyclic response are permanent displacements or liquefaction. Liquefaction is a typical consequence of pore-pressure effects which start building up from the volumetric threshold in cohesionless (sandy) soils (no capacity in standing on its own). Because of (fast) volumetric variations, pore water can move freely through the soil particles. If the pore pressure exceeds the soil skeleton pressure, the soil starts behaving like a fluid and the soil shear strength is lost completely.

2.1.1 Inelastic, Hysteretic Soil Behaviour

The cyclic nonlinear plastic/inelastic unloading-reloading behaviour of soils can be referred to as hysteresis. One cyclic unloading-reloading loop, also referred to as hysteretic loop, is visualized in Figure 2.2.

Experiments have shown that when soils undergo large deformations, such as those induced by earthquakes, their behaviour deviates from linearity, and inelastic

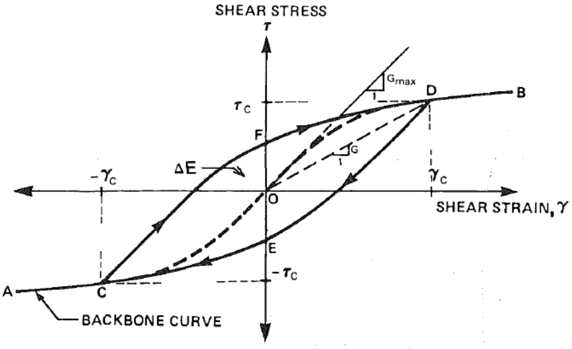

Figure 2.2: Hysteretic loop: fist-cycle stress-strain curve [52].

effects can no longer be ignored [25]. Therefore, to properly model the (strong) seismic, cyclic strain-dependent behaviour of the soil, full nonlinear plastic models, also referred to as hysteretic models, must be used. A plasticity model described by the Masing rules is well-known and commonly used to describe such hysteretic behaviour for soil models. The Masing model assumes that unloading and reloading paths are scaled and/or inverted replicas of the backbone curve: $\tau = f(\gamma)$. Masing's rule for unloading or reloading is defined as:

$$\frac{1}{2}(\tau - \tau_c) = f\left[\frac{1}{2}(\gamma - \gamma_c)\right] \tag{2.1}$$

With (τ_c, γ_c) as the load reversal points. This nonlinear model remembers the previous strain history, but is rate independent, since the path does not depend on the deformation speed and the model is completely defined by its initial load path. The aforementioned hysteretic soil response in Figure 2.2 is constructed under application of the well-known Masing rules. The original rules only describe response under (pseudo-static) harmonic loading. To describe the full range of strain-dependent multi-harmonic unloading and reloading, Pyke [38] describes an extension to the Masing rules:

1. *"The unloading-reloading curves should follow the backbone curve if the previous maximum stress is exceeded."*

2. *"If the current unloading/reloading curve intersects the curve described by a previous load cycle, the stress-strain relationship follows that of the previous cycle."*

2.1.2 Hysteretic Damping

Providing this hysteresis mechanism, another essential quantity can be distinguished: hysteretic damping. Under the criterium that constitutive behaviour is modeled hysteretic, the material exhibits energy dissipation. The amount of energy dissipation is directly related to the area enclosed by the unloading-reloading paths of the hysteretic loop (indicated by ΔE in Figure 2.2). This specific energy dissipation mechanism is no exception in the case of (large-strain) cyclically loaded soils. Generally, an equivalent critical damping ratio ζ is used to indicate the amount of energy dissipation over shear strain amplitude.

2.2 Dynamics of Hysteretic Systems subjected to Ground Motion

Dynamic analyses of structures are commonly carried out through Finite Element Analyses (*FEA*). During Finite Element Analysis the structure is discretized into multiple elements and nodes where individual Finite Elements can be visualized as a small piece of a structure for which we know the relationship between displacement, strain, stress, and forces.

2.2.1 Dynamics of Linear SDoF Systems

The dynamic behaviour of the mass-spring system under a single harmonic force may be considered as a fundamental knowledge, which helps understanding the behaviour of the system under a force of arbitrary time signature because in fact, any (time-dependent) arbitrary force can be represented as a superposition of harmonic forces. The dynamics of a system subjected to a ground motion can be described using a single node carrying a single degree of freedom: *Single Degree of Freedom (SDoF)* system, Figure 2.3. Essentially, a total structure couples' multiple nodes connected by elements creating a Multi Degree of Freedom (*MDoF*) system.

Following Newton's second law, the balance of forces acting on the mass, an equation of motion is found for the single degree of freedom system:

$$m\ddot{u}(t) + c\dot{u}(t) + ku(t) = -m\ddot{u}_g(t) \tag{2.2}$$

$\ddot{u}(t), \dot{u}(t), u(t)$: are the relative acceleration, velocity, and displacement, respectively;

m: is the mass of the system;

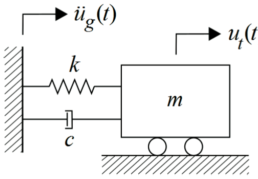

Figure 2.3: Mass-spring-dashpot system subjected to ground excitation [47].

k: is the (linear) spring stiffness;

c: is the viscous damper coefficient;

$\ddot{u}_g(t)$: is the applied ground excitation (in acceleration).

In the case of a time-dependent force, $F(t)$, directly applied on the mass, the equation simplifies to:

$$m\ddot{u}(t) + c\dot{u}(t) + ku(t) = F(t) \tag{2.3}$$

Free Vibrations
The free vibration response is an indicator of the viscous damping present in the system. If the external force is removed at an arbitrary point in time, the right-hand-side of equation 2.3 simplifies further in $F(t) = 0$ yielding a linear homogeneous second order differential equation which can be solved analytically. Upon solving this differential equation, the roots of the characteristic equation hold the property to indicate the corresponding decay of vibrations after load removal. The following relevant cases are discussed:

1. Overdamped: the roots are real valued and the damping coefficient is too large relative to the spring stiffness: $c^2 - 4mk > 0$;
2. Underdamped: the roots are complex valued: $c^2 - 4mk < 0$;
3. Critically damped: $c^2 = 4mk$, $c_{crit} = 2\sqrt{km}$.

In the case of overdamping the free-”vibration” response returns a so called aperiodic motion: after load-removal the mass gradually creeps back towards equilibrium. In the case of underdamping the oscillatory motion free-vibration response decays with exponential amplitude. For the critical damped case the same general aperiodic motion as for overdamping is found. From the critical damping relationship a so-called (linear) critical damping ratio is found, equation 2.4.

$$\zeta = \frac{c}{c_{crit}} = \frac{c}{2\sqrt{km}} \tag{2.4}$$

Metrikine et al. [34] claims that in practice for most situations it is safe to assume that most systems are underdamped: $c << c_{crit}$ where the corresponding free-vibration decays harmonic according:

$$u(t) = A_0 e^{-\zeta \omega_0 t} sin(\omega t + \phi) \tag{2.5}$$

Forced Vibrations
Consider the single degree of freedom system to be excited by an arbitrary harmonic sinusoidal force: $F(t) = F_0 sin(\omega t)$. Searching for a harmonic solution in the frequency-domain in the form of $u(t) = Im[\tilde{U} e^{i\omega t}]$ yields the following expression for the complex amplitude of vibrations:

$$\tilde{U} = \frac{1}{-\omega^2 m + i\omega c + k} F_0 = \tilde{G}(\omega) F_0 \tag{2.6}$$

Taking the identified cases of damping and its characteristics into mind, the ratio of the amplitude of the steady state vibration and the corresponding 'static deflection' $\frac{|\tilde{U}|}{F_0/k}$ yields the dynamic amplification factor directly indicating the dynamic response of a damped single degree of freedom system which is visualized in Figure 2.4 (a). It holds a substantial amount of information from which the following observations can be made:

- when the ratio of forcing frequency to the natural frequency $\frac{\omega}{\omega_0}$ is small, the steady state amplitude converges to that of the static displacement $F_0/k = 1$ regardless of the amount of damping in the system;
- as damping is increased in the system phase lag decreases: resonance occurs at $\omega_r = \omega_0 \sqrt{1 - 2\zeta^2}$;
- when the ratio of forcing frequency to the natural frequency $\frac{\omega}{\omega_0}$ is large the dynamic amplification $\tilde{G}(\omega)$ converges towards zero regardless of the amount of damping in the system;
- when the forcing frequency ω is relatively close to the natural frequency ω_0 of the system the steady-state amplification tends to increase rapidly. The amount

of damping strongly controls the amount of peak amplification. Beyond the critical damping region, namely the overdamped region, the magnification function has no maximum i.e. no peak which means no dynamic amplification is possible if the system is overdamped (and only a maximum of F_0/k can be achieved) [34].

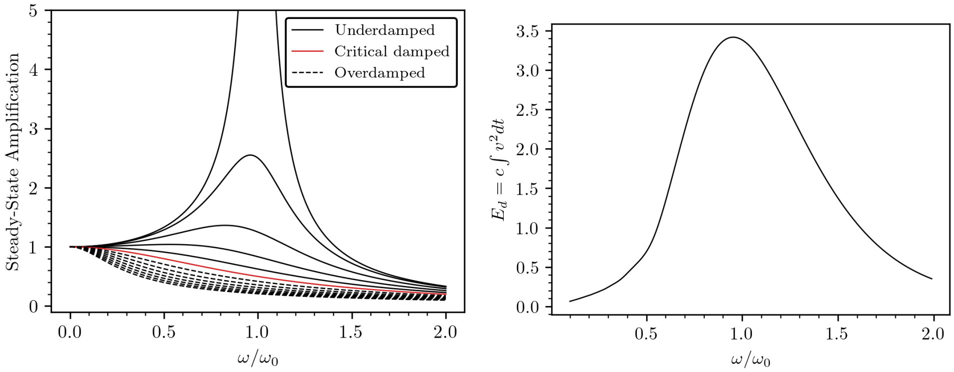

(a) Magnification factor $\frac{|\tilde{U}|}{F_0/k}$ for $F_0/k = 1$

(b) Energy dissipated by a viscous dashpot for an underdamped system

Figure 2.4: Single degree of freedom characteristics

Upon integration of the viscous dashpot force: $\int c\dot{u}(t)du$, the relation of energy dissipation for the viscous damper is found. Using this relation, one could plot the dynamic amplification in terms of energy dissipation and find that, for underdamped systems, the amplification of energy dissipation is again highest around $\omega = \omega_0$. Figure 2.4 (b) visualizes the frequency-dependent energy dissipation response to a unit sinusoidal force for an underdamped unit single degree of freedom linear system.

2.2.2 Nonlinear SDoF Subjected to Ground Motion

The equation of motion of a nonlinear system under a seismic applied motion is presented as follows:

$$\begin{aligned} m\ddot{u}(t) + f_d + f_s &= -m\ddot{u}_g(t) \\ f_d &= c\dot{u}(t) \\ f_s &= f\left(u(t), \text{sign}(\dot{u}(t))\right) \end{aligned} \tag{2.7}$$

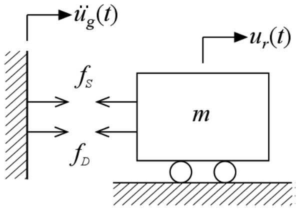

Figure 2.5: Nonlinear SDoF system subjected to ground motion [47].

The system is characterized by a (linear) damping force and a (nonlinear) restoring force where the latter is a function of time and the sign of velocity response. All nonlinear characteristics (including the hysteretic damping mechanism of interest) are hidden within this restoring force. The restoring force at timestep t^{i+1} is defined as: $f_s^{i+1} = f_s^i + k^T(u^{i+1}(t) - u^i(t))$, or in words: the force at timestep t^{i+1} equals the force at time step t^i plus the tangent stiffness times the relative displacement increment in that specific timestep.

Iwan-Masing Model

Experiments have shown that the transition from elastic to plastic is not incidental but happens generally smooth. This smooth transition can be achieved by a specific parallel mechanism first described by Iwan [21]. By using the Iwan-model in a dynamic system, Masing type hysteresis is achieved following the same set of rules but then applied in mechanical formulation. The mechanical formulation and its response is visualized in Figure 2.6.

The behaviour of the Iwan-model can be captured by the continuous change of instantaneous tangent stiffness:

$$k^T = \begin{cases} K_0 \left[1 - \left| \frac{f_s^{i+1}}{F_y} \right|^N \left(\frac{1}{2} + \frac{1}{2}\text{sign}(f_s^{i+1} du) \right) \right], & |f_s| < F_y \\ 0, & |f_s| \geq F_y \end{cases} \tag{2.8}$$

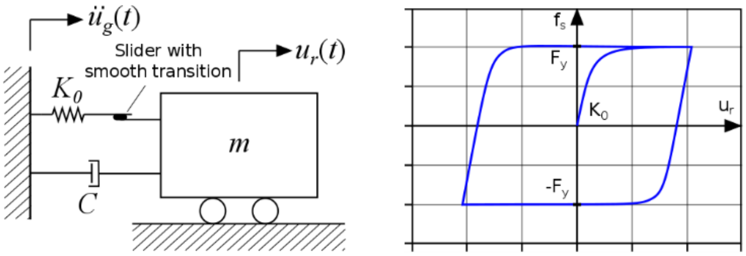

Figure 2.6: Visualization of the Iwan-model providing smooth hysteresis [47].

N is a parameter that controls the smoothness by directly defining the number of elements in parallel.

2.2.3 Seismic Analysis of Nonlinear MDoF Systems

Generally speaking, equation 2.7 can only be solved numerically. Despite full accuracy is possible this is an onerous task, especially when many degrees of freedom are involved. Due to the nonlinear nature of the stiffness (in multi degree of freedom formulation: a stiffness matrix), the stiffness varies over time implying the need to update the stiffness matrix every time instance. In earthquake design codes it is well-known practice to repeat analyses for multiple sets of input ground motions and directions [47] which is a time consuming process. The dynamic response is often computed using simplified methods of analysis opposing the computationally demanding full nonlinear time history analysis. Tsouvalas et al. [47] discusses two common simplified nonlinear analysis methods in relation towards seismic design. The following simplified strategies will be discussed briefly:

1. Equivalent elastic analysis using a behaviour factor: q;
2. Modal pushover analysis

During the first strategy, instead of designing for elastic forces, the design is based to withstand reduced forces through introduction of this reduction factor q. Application on a multi degree of freedom system is questionable. The value of the factor varies per vibration mode and the principle of superposition of the response for each vibration mode does not hold for nonlinear systems. In application of the second strategy, the displacement pattern of a pushover analysis is substituted by that of an arbitrary modeshape computed by a (linear) eigenvalue analysis. However, because of nonlinear stiffness in nonlinear systems, the modes of vibration vary over time.

2.3 Soil-Structure Interaction (SSI)

The dynamic response of the offshore wind turbine structure is affected by the procedure in which the 'free-field' soil is coupled with the monopile structure: the soil-structure interaction (SSI) mechanism. For an accurate representation of dynamic response, it is necessary that the soil-structure interaction mechanism is accurately accounted for. Soil characteristics and therefore the soil-structure interaction mechanism considered in design contributes to most of the uncertainties in the design [6]. Mainly because the mechanism involved behaves nonlinear. It is proven that the influence of soil-structure interaction on the response of the offshore wind turbines is significant [10] even possibly capable of reducing earthquake loads by as much as 10% [26] if captured accurately. De Risi et al. [11] concluded that the lack of proper soil-structure interaction modelling leads to an overestimation of the seismic capacity of about 60% and 70% of the serviceability limit state and ultimate limit state, respectively.

2.3.1 Aspects of Soil-Structure Interaction

The cyclic soil behaviour and soil-structure interaction for monopile foundations approximately follows Masing-type behaviour under small soil strains/deformations but accuracy decreases when soil strain/deformation increases. To increase accuracy and understanding of the hysteretic models to be applied in the soil-structure interaction mechanism the response must incorporate additional mechanisms. PISA [4, 7] carried field tests to study soil-structure interaction effects under cyclic loading. The following effects were observed having direct effect on the unloading-reloading loop shape:

- rate effects resulting in an increased foundation capacity at fast load rates;
- ratcheting (asymmetric cyclic loading);
- and gapping (gaps occurring between soil and pile: contact with the soil is lost and consequently the soil stiffness is lost).

Furthermore, [9] suggests the following observation: stiffness degradation under increased vibration amplitude, and [30] presents the effect of strength deterioration under increasing displacement amplitude of cyclic loading for soft clays. On top of that, it is important to mention that 3D to 1D modelling in current industrial approaches oversimplifies the failure mechanism occurring for rigid monopiles due to effects of pile diameter and aspect ratio [54].

2.3.2 Typical Industrial Practice of Foundation Design

The design of monopile foundations is mostly performed using the so-called *p-y method* based on a series of 1D spring elements along the monopile embedment depth. This is a distributed element model (also commonly referred to a Winkler foundation model) where uncoupled springs couple the free-field soil with the structure, and, in that way accounting for the soil-structure interaction mechanism. The spring properties are generally defined using a set of soil reaction curves: depth varying free-field soil response in the form of nonlinear elastic p (force) – y (displacement) curves directly specifying the load-path (and stiffness) of the springs. The p-y method is visualized in Figure 2.7.

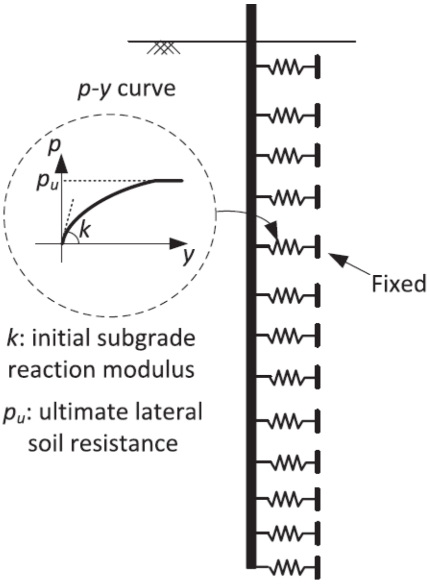

Figure 2.7: Schematic of the spring method used in practice for static analysis of laterally loaded single piles [40].

The industry mainly follows the DNV [12] standard which has adopted the p-y approach from the oil & gas industry: American Petroleum Institute (API) [3]. Here, research was conducted on long and slender (flexible) piles (typically pile diameters of 0.6m) whereas large monopile foundations of about 8m in diameter in shallow waters are currently state of the art [59]. Rigid monopiles activate a whole different (more global instead of local [51]) response compared to more slender piles where for the latter the effects of pile diameter and aspect ratio are of no significance.

These reaction curves are no physical representation of the soil-structure interaction but merely a description of the static lateral (1D) resistance. The method should therefore be adopted with care as its limitations and the applicability to rigid monopile foundations under cyclic loading is well questioned [51, 7, 40, 39, 61, 54, 41]. Static pushover analysis using a 3D continuum model is generally used to determine p-y curves of higher accuracy to be used in the Winkler approach applicable to rigid monopile foundations. It is demonstrated that under the application of ground shaking API p-y curves are considerably different from ones obtained from a continuum model because the initial slope and ultimate resistance is poorly predicted [41]. In the derivation of p-y curves, load-paths derived based on cone-penetration tests (CPT) have shown great potential in the simulation of more realistic soil-pile interaction for laterally loaded piles in cohesionless soil under static loading where [45] validates such formulation against a full-scale wind turbine.

p-y **Method for Cyclic Loading**

For the case where equilibrium has been reached under cyclic loading, the ultimate capacity of p-y curves is reduced by an empirical reduction factor because cyclic loads cause deterioration of lateral bearing capacity [3]. Reese et al. [42] describes the same procedure but approaches the multiplication of a loading-type coefficient $\overline{A}_s$ or $\overline{A}_c$ (static/cyclic) for depth to diameter ratio z/D graphically which may be computed from figure 3.24 in [42]. In the case of soft clay (cohesive soil) the degradation varies over depth which is highest around the ground surface and decreases linearly until a critical depth is reached. Beyond this critical depth, failure occurs in a different mode: from wedge failure at shallow depths to flow failure beyond the critical depth threshold. The backbone relation changes over increasing deflection amplitude y and depth z. After a certain displacement the reaction force remains constant: the soil-pile system tends to stabilize if equilibrium is reached under cyclic loading. This effect is in literature often denoted as *shakedown*. Because the approach represents the cyclic loading using an equivalent monotonic/static approach, it is unable to provide any information about mechanisms occurring during cyclic and dynamic soil-structure interaction including the effects of soil material damping. These mechanisms are mostly related to the soil behaving as a plastic material but, instead: using the approach API [3] prescribes, the soil state is assumed elastic (material returns to its original state when force is removed). The tendency of this method to under-predict the ultimate lateral resistance, combined with the relatively large displacement required to mobilize the ultimate resistance, are the principal causes of the traditional approach to give a conservative estimate of overall pile response for wave- and wind-loading [7]. Since these empirical factors are based on slow cyclic loading, they are therefore prone to erroneous results applied to strong cyclic loading [40].

2.3.3 3D to 1D Considerations

The soil-monopile mechanism is in fact a 3D environment which is nonlinear. The p-y curve approach is merely a description of lateral 1D resistance and therefore, the reliability of these p-y curves is well questioned. The diameters of state-of-the-art monopile foundations are way beyond the original field tests conducted for API regulation. In terms of cyclic response and (even more severe) strong dynamic response the influence of the 3D to 1D soil-structure interaction mechanism simplification yields even more uncertainties compared to a static load-case. As described in 2.3.2, often a 3D continuum model is used to determine more accurate p-y curves based on a rigid monopile foundation. However, it is time-consuming to build many 3D FE models for many wind-turbines in a wind farm. The soil stratum can be complicated in areas like Japan and varies from site to site [54] resulting in different site-specific dynamics.

The simplifications in the 3D to 1D mechanism form the basis of the convenience of the current industrial practice of foundation design conform the p-y method. The simplifications can be very extensive and it is therefore very important to know and assess the limitations of the preferred foundation design method. Despite attempts have been made in formulating analytical expressions to account for shortcomings in current recommended pile design [54, 59], general consensus is yet to be reached in the application of design standards and are therefore not considered further.

2.4 Foundation Damping

Foundation damping – dissipation of energy from structure (monopile) to the environment (soil) through radiation of elastic waves and soil material damping – plays an important role in the design process as it limits the response amplitude over time. An accurate representation of the offshore wind turbine foundation damping, and therefore soil-structure interaction, is necessary for efficient designs. Foundation damping is found to have the highest contribution to the overall damping when the turbine is idle or when the side-side motion (parallel to the rotor diameter) is considered [29]. During operating conditions, it is considered to have the second largest contribution. Considering its significance in contribution, increasing its accuracy potentially holds great value to reach more cost-effective designs.

2.4.1 Soil Material / Hysteretic Damping

Soil material damping is arguably the most important contributor to foundation damping [29]. It is the result of energy dissipation within the soil mass due to friction, sliding and structural rearrangement of the soil medium originating from the soil nonlinear behaviour, making it a nonlinear source of damping. It is dependent on the soil shear strain and generally insensitive to frequency or rate of loading.

An equivalent critical damping ratio is typically used to support elastic analysis to characterize the energy dissipation in soils. The equation is expressed as a function of the energy dissipated over one load cycle E_h (directly related to the loop area) and the maximum stored elastic energy (or maximum potential energy) stored during the cycle E_p.

$$\zeta = \frac{1}{2\pi}\frac{A_{loop}}{ky^2} = \frac{1}{4\pi}\frac{E_h}{E_p} \tag{2.9}$$

In equation 2.9 the stiffness term k and amplitude displacement term y can be related towards soils using $k = G$ and $y = \gamma_c$ (Figure 2.2). The strain-dependence of the damping mechanism (and shear modulus) is visualized in Figure 2.8. The secant stiffness decreases and equivalent damping ratio increases gradually over increasing strain amplitude. The energy quantities, E_h and E_p are indicated by the shaded and hatch pattern, respectively. At large strain/deformation the damping ratio ζ is significantly overestimated up to a value of 60% whereas experimental results have shown geometric soil damping ratios of approximately 20-30% under large values of strain/displacement [36]. In Figure 2.9 the overestimation of equivalent damping is visualized as a result of the application of equation 2.9 on hysteresis computed using Masing rules.

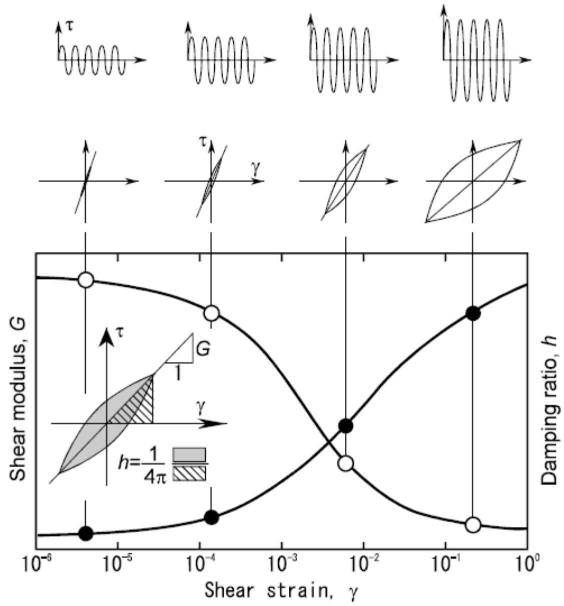

Figure 2.8: Hysteresis visualized over different strain amplitudes [56]

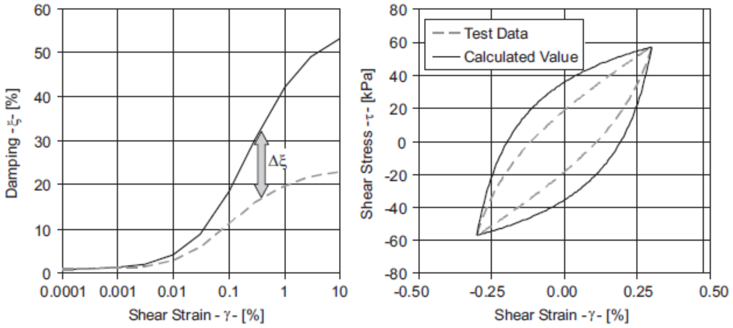

Figure 2.9: Overestimation of hysteretic damping by Masing rules [36].

2.4.2 Radiation Damping

Whenever the monopile foundation moves against the surrounding soil, stress waves originate at the contact surface and spread outward. These waves carry away some of the energy transmitted by the foundation into the soil. Its behaviour is found to be comparable with viscous damping [18]. The magnitude of the radiation damping depends mainly on the frequency of excitation, geometry of soil-foundation system, mode of oscillation, and the stress-strain characteristics of the soil. It is found to be important at high frequencies $(> 1Hz)$ which makes it in potential an important contributor to the damping of seismic loading. Radiation damping is generally of small influence and often neglected for vibrations in the horizontal direction because the loading frequency of wind- and wave-loading and fundamental frequency in the lateral direction is typically below $1Hz$. For lateral strong seismic loading, damping originating from soil nonlinearities is found to be prone [56, 60] on which literature concludes that the contribution of radiation damping is thought to be negligible during strong seismic (laterally-focused) motions.

2.4.3 On the Topic of the Classical Equivalent Viscous Damping Ratio

The process of representing equivalent viscous damping is not easily applied to arbitrary nonlinear systems [22, 19]. This makes its applicability questionable to evaluate soil-structure interaction. On top of that, it holds some debatable assumptions in its derivation:

- the theory is considered for a single single degree of freedom system only, making the direct application debatable in a multi degree of freedom system (Winkler foundation model in question) where the nodal response is coupled;

- the steady-state displacement (and therefore velocity) is assumed perfectly harmonic (e.g. $u(t) = Ucos(\omega t - \phi)$);

- considering the assumption above, the hysteretic loop in question is completely symmetrical and perfectly elliptical whereas it is generally known that this does not hold for a seismic load-case;

- plasticity effects (permanent displacements) are disregarded: the mean of oscillation is assumed around zero displacement;

- the energy dissipated by the viscous damper E_d (2.4 (b)) considered over one load cycle for a nonlinear system is derived based on a critical damping coefficient related to a linear system;
- evaluating the integral in Figure 2.4 (b) will result in energy dissipated by a linear viscous damper that is proportional with respect to the excitation frequency [19]. Damping originating from hysteresis is generally insensitive to frequency (2.4.1). To overcome frequency dependency it is assumed that the excitation is harmonic with the same frequency as the natural frequency of the system ($\omega = \omega_0$);
- throughout literature, often the area under a linear secant stiffness is used to specify the maximum potential energy E_p, i.e. the stored energy is taken to be square-proportional to the displacement for every loop to be considered which is inexact in the case of highly nonlinear behaviour.

It seems apparent that in the simulation of highly nonlinear seismic response, the use of the classical equivalent damping ratio ζ in the form presented in equation 2.9 yields little reliability in accurate values equivalently accounting for the hysteretic damping mechanism during stochastic excitations. Each of the aforementioned assumptions must be carefully taken into mind because the procedure is not always applicable in arbitrary elastic analyses. On top of that, one must not forget that the theory upon which the derivation is based does not include additional soil-structure interaction components discussed in 2.3.1 and 2.3.3.

2.4.4 Recommended Practice of Foundation Damping in Seismic Design

DNV [12] prescribes that the application of foundation damping, both hysteretic and radiation, when using time-domain analyses may be represented by a series of dashpots connecting to the same nodes as the soil reaction springs. The equivalent viscous damper coefficients may be approximated as the sum of the two components. In that way, the hysteretic soil damping contribution is accounted for on a local scale (per soil spring). The soil hysteretic damping contribution may be applied in terms of a percentage of critical damping in seismic design practice. To determine the amount of hysteretic damping contribution, is then referred to equation 2.9 which may be applied in parallel with secant stiffness linear elastic soil springs. Practically, for each individual soil-structure interaction component equivalently damped linear analysis may be supported by secant stiffness and equivalent damping curves: Figure 2.8.

This is a procedure which is well applied in one-dimensional site response analysis (shear wave propagation to bedrock shaking, [16]). Upon application of an iterative procedure (as it is not possible to determine the maximum level of strain before the analysis is completed) convergence can be found somewhere on the specific target curves. Furthermore, upon recognizing that when using the (extended) Masing rules the hysteretic damping contribution is physically overestimated compared to laboratory testing: using a widespread of dynamic test results [37, 36] present a reduction factor which effectively reduces the amount of damping to a level which is close to measurement data. It must be clear that when the implemented soil springs are fully nonlinear and inelastic, the hysteretic damping term shall always be omitted [12].

In the turbine manufacturing industry logarithmic decrement damping is also frequently used to apply damping on a global level instead. A percentage of critical damping is applied per mode of vibration. Such logarithmic decrement is typically found in either time-domain or frequency-domain strategies under so called 'rotor-stop' tests. Here, the offshore wind turbine is shut down and subsequent decaying movement is measured. While the amount of damping present is dependent on soil- and structural characteristics, typical numerical and experimental data shows 0.8-1.5% critical damping in the first bending mode originating from the soil [50, 13].

2.5 Random Vibrations

The randomness of the earthquake signal can be addressed by statistical methods: in terms of probability. During the application of statistical and stochastic methods on dynamically loaded structures, the loads are often schematised by so-called stationary ergodic processes. Such a procedure often thrives on the assumption that a stochastic load is a summation of sine functions with random phase angle (2.2.1).

Earthquake response analysis is generally done in the frequency-domain using variance spectra [1]. A variance spectrum represents the total variance of a signal and can be considered as a summation of the contributions of the several Fourier components [1]. Conducting analyses within the frequency-domain provides significant computational gain compared to time-domain analysis. This solution strategy is however limited to linear analyses. A linearization procedure is therefore required when used in solving nonlinear dynamic systems.

Chapter 3

Beam on Winkler Foundation Model

In reality, a total structure will experience 3-dimensional excitation under a seismic load-case (2.3.3). On top of that, each loading direction and structural response interact and influence each other. Considering the scope of this research: the main point of interest is the lateral response only, which is thought to be most dominant in design for Offshore Wind Turbines. It is common practice to assess structures by discretization of the physical problem into a Finite Elements (2.2). To assess equivalent hysteretic damping originating from the soil-structure interaction mechanism between the soil and monopile supported offshore wind turbine structure due to (lateral focused) seismic response, a 2-dimensional Finite Element model is developed. OpenSees (the Open System for Earthquake Engineering Simulation) [31] enables users to create finite element applications for simulating the response of structural and geotechnical systems subjected to earthquakes and is adopted in this study as tool to approximate the structural behaviour.

3.1 Monopile Supported OWT and Site Characteristics

3.1.1 Soil Characteristics

The effect of soil layering is that the overburden pressure of overlying soil layers will influence the resistance of the layers beneath. In order not to underestimate the soil resistance of a dense layer overlying a light one or underestimate the soil resistance of a light layer overlying a dense one the soil reactions must be altered to incorporate the soil layering effect. To incorporate these effects, Georgiadis et al. [42] presents a method to correct the capacity of the p-y curves applicable to a Winkler foundation soil-pile interaction model. The method is based on determining an equivalent depth where the layer beneath would have started if the layer would have been the same material holding the same properties as the layer above. For realistic soil resistance and, therefore, (more) realistic structural response the layering effect must be incorporated. Though, for educational purposes it is chosen not to incorporate the effect as the main focus of interest lies within the dynamic soil-pile interaction response mechanism following this initial static soil reaction curve. The following educational soil profile is considered to investigate the beam on hysteretic Winkler foundation model response:

Layer	Soil Type	z_{top} $[m]$	z_{bot} $[m]$	γ' $[kN/m^3]$	ϕ $[deg]$	c_u $[kPa]$	PI [%]
1	sand	0	-2.5	8	35	-	-
2	sand	-2.5	-4.5	8	40	-	-
3	clay	-4.5	-9.5	6.5	-	70	30
4	clay	-9.5	-14.5	6.5	-	80	30
5	sand	-14.5	-24.5	8.5	40	-	-
6	sand	-24.5	-50	8.5	37	-	-

Table 3.1: Sand overlying Clay overlying Sand: Mixed Soil Profile

3.1.2 OWT Characteristics

The turbine properties presented hereafter will be discretized to approximate the structural behaviour. The foundation and tower structural geometry and properties are based on *Siemens Gamesa Renewable Energy 8.0 MW: SG 8.0-167 DD* as reference offshore wind turbine. Simplification has been made in the behaviour of the turbine model as added mass for contained soil / water is not included and the behaviour of the machine (RNA + blades) is approximated as a single lumped point mass at tower top. Also, foundation and tower are assumed perfectly tubular without cross-sectional discontinuities on the surface and the connection between monopile foundation and tower is assumed to be completely rigid. The monopile foundations' outer diameter considered is $7.5m$. Additional relevant structural and geometric characteristics are presented in Table 3.2. The model focuses on the fore-aft motion only hence $J = I_{xx}$ but considering the RNA is modeled as a lumped mass/inertia, the difference is only present in amount of inertia considered.

	L $[m]$	E $[kg/ms^2]$	G $[kg/ms^2]$	m $[kg]$	J $[kgm^2]$
Foundation	83.69	2.1E11	8.1E10	-	-
Tower	88.82	2.1E11	8.1E10	-	-
Top Mass	-	-	-	4.5E4	6.5E7

Table 3.2: Geometric Characteristics of Foundation and Tower

3.2 Structural Modelling

The structure is divided into many elements (Timoshenko beam elements: 3.2.1) which are joined by nodes where degrees of freedom (DoF's) are defined. In the current study, which is chosen to be limited to an in-plane two-dimensional problem, the number of degrees of freedom at the nodes is limited to 3: $\mathbf{x}(t) = [\mathbf{u}_y, \mathbf{u}_z, \phi]$.

The governing set of coupled equations describing the dynamic response of the total discretized nonlinear multi-degree of freedom structure yields for uni-axial ground excitation:

$$\mathbf{M}\ddot{\mathbf{x}}(t) + \mathbf{C}\dot{\mathbf{x}}(t) + \mathbf{f}_s(\mathbf{x}(t), \text{sign}(\dot{\mathbf{x}}(t)), t) = -\mathbf{M}\mathbf{r}\ddot{u}_g(t) \tag{3.1}$$

Equation 3.1 describes the systems' total mass matrix $\mathbf{M}$, linear damping matrix $\mathbf{C}$, and stiffness term and couples them through the total translational, velocity, and acceleration degree of freedom vector $\mathbf{x}(t)$. The right-hand-side of the equation describes the in-plane seismic force input with vector $\mathbf{r}$ being an influence factor linking the corresponding ground motions to the correct mass degree of freedom. Solving the coupled set of equations is an onerous task because the nonlinear stiffness contribution is updated each time step and can therefore generally only be solved numerically. For reference purposes, in the linear elastic case the total stiffness term $\mathbf{f}_s(\mathbf{x}(t), \text{sign}(\dot{\mathbf{x}}(t)), t)$ will simplify to $\mathbf{K}\mathbf{x}(t)$.

The total mass matrix $\mathbf{M}$ with size [NDoF x NDoF] is described by the global translational $\mathbf{M}_t$ and rotational mass (inertia) $\mathbf{M}_\theta$:

$$\mathbf{M} = \begin{bmatrix} \mathbf{M}_t & \mathbf{0} \\ \mathbf{0} & \mathbf{M}_\theta \end{bmatrix} \tag{3.2}$$

Additional structural damping is set to zero for ease of calculation. The total linear (velocity proportional viscous) damping matrix $\mathbf{C}$ with size [NDoF x NDoF] is therefore $\mathbf{0_{NDoFxNDoF}}$ which implies the *null matrix* (all entries are zero) in the case without any source of velocity proportional viscous damping meaning without any viscous dashpots applied (2.2.1). Matrix entries will be nonzero in the degrees of freedom where viscous dashpots would have been present.

The total stiffnes matrix $\mathbf{K}$ with size [NDoF x NDoF] is described by the (linear) structural geometry of the structure: the bending and shear resistance of the structure providing bending and shear resistance to the element $\mathbf{K}_g$, and the stiffness component from the foundation springs $\mathbf{K}_f$, respectively. The latter is updated each timestep when the foundation springs behave nonlinear.

$$\mathbf{K} = \begin{bmatrix} \mathbf{K}_{tt} & \mathbf{K}_{t\theta} \\ \mathbf{K}_{\theta t} & \mathbf{K}_{\theta\theta} \end{bmatrix} + \begin{bmatrix} \mathbf{K}_{tt,f} & \mathbf{0} \\ \mathbf{0} & \mathbf{0} \end{bmatrix} \tag{3.3}$$

3.2.1 Timoshenko Beam Theory

The offshore wind turbine foundation and tower constitutive behaviour is captured using elastic Timoshenko beam elements connecting nodes. The choice for the application of Timoshenko beam theory over Euler-Bernoulli beam theory follows from the fact that the equations for the beam theory in question is based on both shear (transverse deflection $y(z,t)$) and bending deformations (cross-sectional rotation $\phi(z,t)$). The choice is substantiated because the effect of shear deformation and of rotational inertia may not be neglected as the foundation and tower geometry is characterized as a 'thick beam' exhibiting shear deformation under bending.

The governing system of equations of motion present themselves after coupling of the kinematic, constitutive and equilibrium relationships:

$$\rho A \frac{\partial^2 y}{\partial t^2} - q(z,t) = \frac{\partial}{\partial z}\left[GA\kappa\left(\frac{\partial y}{\partial z} - \phi\right)\right] \tag{3.4}$$

$$\rho I \frac{\partial^2 \phi}{\partial t^2} = GA\kappa\left(\frac{\partial y}{\partial z} - \phi\right) + \frac{\partial}{\partial z}\left(EI\frac{\partial \phi}{\partial z}\right) \tag{3.5}$$

Where:

ρ: is the density of the Timoshenko beam material;

GA: is the shear stiffness which is the product of G, the shear modulus and A, the cross-sectional area;

κ: is a cross-sectional dependent shearing coefficient;

EI:is the bending stiffness of the Timoshenko beam which is the product of E, the Young's Modulus and I, the area moment of inertia;

y: is the corresponding lateral pile deflection.

Euler-Bernoulli bending is obtained by approaching the limit case of $GA\kappa = \infty$, or in words: rigid shear stiffness. Pure shear is obtained by approaching the limit case of $EI = \infty$, or in words: rigid in bending. Implementation in OpenSees is conveniently achieved by specifying E, G, A, I, A_{vy}, and m where the latter two represent the cross-sectional shear area and the mass per length, respectively. Hutchinson et al. [20] prescribes a formulation of the cross-sectional dependent κ value applicable to Timoshenko beam theory. Though, throughout subsequent results the value of $\kappa = 0.52$ is adopted.

3.3 Dynamic Soil-Pile Interaction Spring Element

There have been many attempts in search of hysteretic rules with increased accuracy in the large-strain regime even with research directly related to pile applications. Although, most research is still based on long and slender piles. Boulanger et al. [5] describes the numerical implementation of soil-pile interaction under dynamic loading while holding on to the p-y curve Winkler approach. A nonlinear, dynamic p-y spring element was developed that can model a range of desired p-y behaviour. The nonlinear p-y element suggested follows conceptualized behaviour consisting of elastic $(p - y^e)$ (representing response far from the structure), plastic $(p - y^p)$, and gap components $(p - y^g)$ (latter two representing response near the structure) placed in series where a dashpot which is placed in parallel with the elastic component. This represents the simulation of radiation damping behaviour. The dynamic spring element is formulated as such that the gap components (in the form of a drag- and closure spring) are only of influence if a gap has been formed in its previous load cycle. For the implementation of the Boulanger element in OpenSees (using the *PySimple1* material model) the viscous damper is placed across the entire material, but the viscous force is calculated as proportional of the component of velocity that developed in the far-field elastic component of the material to the displacement in the total element. This still correctly causes the viscous damping term to become zero during load increments along a fully formed gap where physically speaking the contact with soil is lost. Using this approach, the radiation dashpot force is not considered in solving for compatible forces and displacements, only after which results in a more computationally stable approach. Consequently, by placing the dashpot in series with the elastic component (as its implementation in OpenSees, Figure 3.1) instead of in parallel (as formulated by [5]) representing the Maxwell model and Kelvin-Voigt model, respectively results in a different formulation of deformation over time and is expected to produce excessive damping forces under large strains.

The element is described using the p-y behaviour of each component. The total p-y element represents:

$$\begin{aligned} p &= p^{e(lastic)} = p^{p(lastic)} = p^{g(ap)} \\ p^{g} &= p^{d(rag)} + p^{c(losure)} \\ y &= y^{e} + y^{p} + y^{g} \end{aligned} \tag{3.6}$$

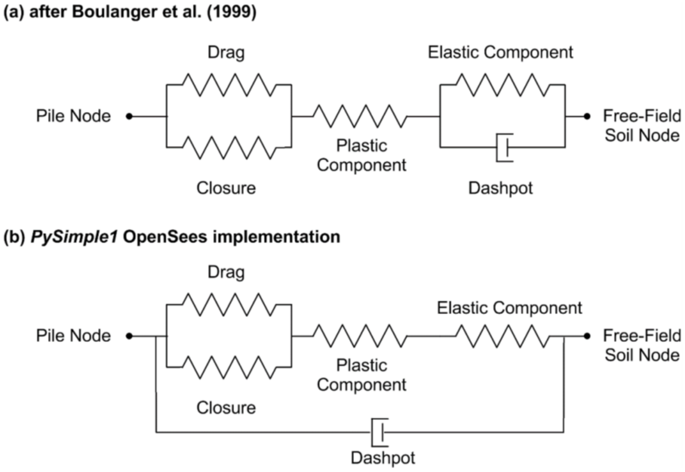

Figure 3.1: Boulanger element and its implementation in OpenSees: PySimple1 [48].

3.3.1 Backbone p-y and Global Cyclic Response

Before any signs of a gap, the dynamic spring element is characterized by a nonlinear backbone curve that represents its initial load-path. The backbone curve of the dynamic spring element is distinguished in a 'far-field' elastic region and a 'near-field' plastic region in accordance with the mechanical formulation of the spring element. The initial elastic region is characterized by the region where the plastic spring is defined to behave rigid:

$$-C_r p_{ult} < p < C_r p_{ult} \tag{3.7}$$

Meaning, the load at yield point p_0 is defined by:

$$p_0 = C_r p_{ult} \tag{3.8}$$

The linear far-field spring $(p - y^e)$ is described by:

$$p = C_e \frac{p_{ult}}{y_{50}} y^e \tag{3.9}$$

Beyond this initial elastic region, the nonlinear region of the backbone curve is described by the plastic spring component $(p - y^p)$:

$$p = p_{ult} - (p_{ult} - p_0) \left[\frac{c y_{50}}{c y_{50} + |y_p - y_0^p|} \right]^n \tag{3.10}$$

Where p_{ult} = the ultimate resistance of the p-y material in current loading direction; $p_o = p$ and $y_o^p = y_p$ at the start of the current plastic load cycle. Unloading and reloading is achieved by updating the reversal point (p_o, y_o^p) starting with the last soil resistance value of the elastic spring and corresponding elastic pile displacement. In subsequent loading cycles; c = a constant to control the tangent modulus at the start of plastic yielding; n = an exponent to control the sharpness of the $(p - y^p)$ curve; and y_{50} = the displacement at which 50% of the ultimate capacity p_{ult} is mobilized in monotonic loading. Lastly, C_e denotes the stiffness factor for the initial elastic region of the backbone curve. Values of p_{ult}, y_{50}, c, n, C_e, and C_r are used as such to approximate the shape of different p-y backbone relations.

The shape of the load paths / hysteretic loops is influenced by the gap component (in the form of a drag and closure spring in parallel) in the dynamic spring element after mobilization of the initial load path. The closure spring component $(p^c - y^g)$ allows for smooth transition in the p-y behaviour as the gap opens and closes and is described by:

$$p^c = 1.8p_{ult} \left[\frac{y_{50}}{y_{50} + 50(y_0^+ - y^g)} - \frac{y_{50}}{y_{50} + 50(y_0^- - y^g)} \right] \tag{3.11}$$

Where y_o^+ = a memory term for the positive side of the gap; and y_o^- for the negative side. Initial values are set as: $y_{50}/100$ and $-y_{50}/100$, respectively. The factor of 1.8 brings p^c up to p_{ult} during initial loading to y_o^+ and y_o^-.

The nonlinear drag spring component $(p^d - y^g)$ is described by:

$$p^d = C_d p_{ult} - (C_d p_{ult} - p_0^d) \left[\frac{y_{50}}{y_{50} + 2|y^g - y_0^g|} \right]^n \tag{3.12}$$

Where C_d = the ratio of the maximum drag force to the ultimate resistance p_{ult}; $p_o^d = p^d$ and $y_o^g = y^g$ at the start of current loading cycle. The gap development and lateral response is visualized in Figure 3.2.

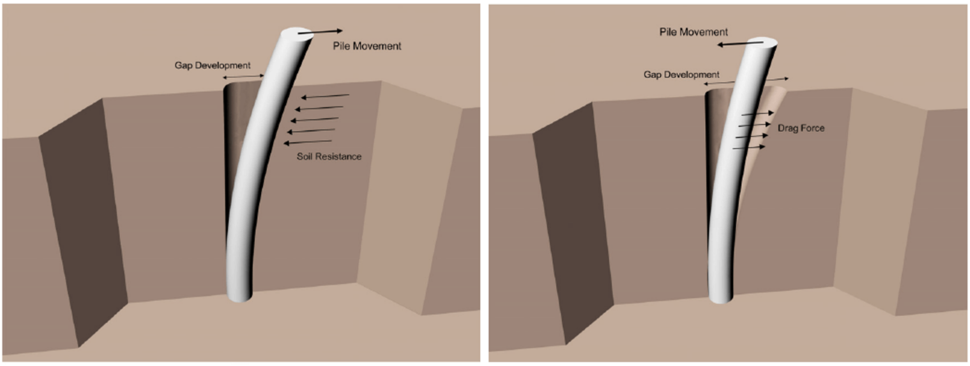

Figure 3.2: Gap development under lateral loading [33].

The dynamic spring element can be classified in terms of its restoring force relationship to relate its properties in terms of dynamics of a hysteretic system. This has been presented earlier by specifying its tangent stiffness relationship in 2.2. The elastic, plastic, closure, and drag spring components, equations 3.9, 3.10, 3.11, and 3.12, respectively can each be classified in terms of its tangent stiffness after rewriting the force-displacement (p-y) relationships:

$$k^e = C_e \frac{p_{ult}}{y_{50}} \tag{3.13}$$

$$k^p = \frac{n \, \text{sign}\,(\dot{y}\,(t))\,(p_{ult} - p_0)}{|y^p - y_0^p| + c y_{50}} \left[\left(\frac{c y_{50}}{|y^p - y_0^p| + c y_{50}} \right)^n \right] \tag{3.14}$$

$$k^c = \frac{1.8 p_{ult} \frac{y_{50}}{50}}{\left(\frac{y_{50}}{50} - y^g + y_0^+\right)^2} - \frac{1.8 p_{ult} \frac{y_{50}}{50}}{\left(\frac{y_{50}}{50} - y^g + y_0^-\right)^2} \tag{3.15}$$

$$k^d = \frac{2n\left(p_0^d - C_d p_{ult}\right)}{y_{50} + 2\left|y^g - y_0^g\right|}\left(\frac{y_{50}}{y_{50} + 2\left|y^g - y_0^g\right|}\right) \tag{3.16}$$

The total nonlinear spring stiffness yields:

$$k^g = k^d + k^c \tag{3.17}$$

$$k = \frac{1}{\frac{1}{k^e} + \frac{1}{k^p} + \frac{1}{k^g}} \tag{3.18}$$

In the gap region the closure spring takes no load, and the total soil resistance will only be governed by the drag spring. At the end of the region, the gap component represents rigid behaviour by reaching infinite stiffness: $k^g \rightarrow \infty$.

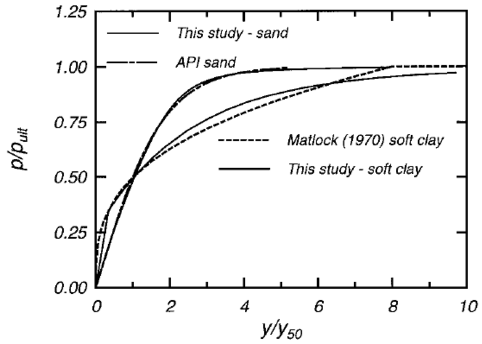

Figure 3.3: Hard-coded approximation p-y curves of Boulanger element [5]

Unfortunately, the implementation of the element in OpenSees using PySimple1 yields limited freedom in defining the shape of these backbone curves through direct input parameters. Through defining a soil type (soft clay or sand) two specific sets of hard-coded parameters are available for the user defining the shape of the curve leaving just two parameters for direct input by the user: p_{ult} and y_{50}. Conveniently enough such an approach is consistent throughout literature. Design codes, such as API [3], prescribe the shape of the p-y curve to represent a specific soil type from which the user calculates the values of p_{ult} and y_{50} through provided equations. Though, the hard-coded implementation leaves even a bigger drawback in simulating accurate soil-pile interaction response. The backbone curve shapes for soft clay and sand, approximating Matlock [30] and API [3], respectively, are of when equilibrium is reached under static loading since there is no sign of empirical reduction of ultimate resistance (2.3.2). The hard-coded approximation of static p-y curves is visualized in Figure 3.3.

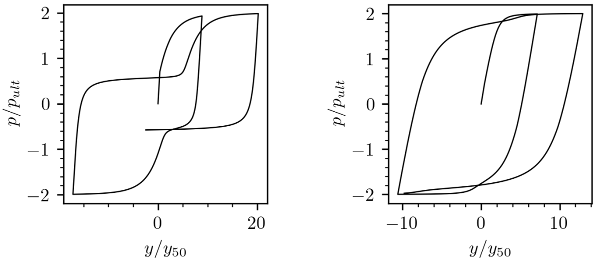

(a) Global response for clay (b) Global response for sand

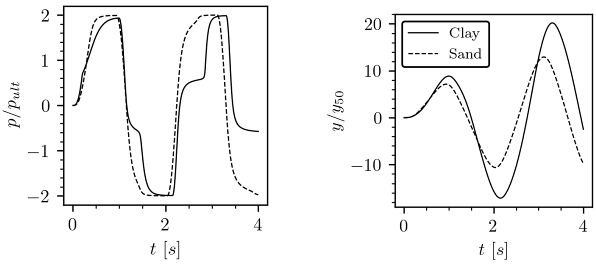

(c) Reaction force (d) Displacement response

Figure 3.4: Overview of the global response for hard-coded sets of clay and sand

The (normalized) global cyclic response of the PySimple1 material object to a unit sinusoidal force is visualized in Figures 3.4. Ater following the initial load-path, the influence of the gap spring component by means of drag-resistance parameter C_d is visible: within a fully mobilized gap only a maximum of $C_d * p_{ult}$ soil resistance is possible. In return, the closure spring component ensures that the stiffness increases again before reaching the ultimate capacity. The effect is slightly visible for sand as the recurring loops return a slightly different stiffness than its initial load-path after reaching p_{ult}. This effect can be described as a numerical effect of the drag force resistance parameter C_d that affects the cyclic stiffness, and does not represent the physical effects of gapping. Though, the drag force resistance parameter influence is only mobilized after the ultimate capacity is reached in a previous load-cycle. because of the plasticity in the element, more displacement needs to be mobilized in subsequent load cycles to again reach the full ultimate capacity p_{ult}.

On the Limited Applicability

The Boulanger element formulation and its implementation in OpenSees by the name of PySimple1 is setup as such, that the backbone curve approximates a short-term static load-case and therefore, there is no strength degradation in terms of cyclic loading. Where cyclic loading for sand is represented by an empirical reduction factor A to reduce the amplitude of p (chapter 2.3.2) (shape of the curve remains the same), cyclic loading for clay is represented in a somewhat more complicated approach as the ultimate capacity of the material decreases linearly over y. This mechanism of decreasing p over increasing y is not found in the static representation of the backbone p-y in Figure 3.3 and therefore not found in the hysteretic loops in Figure 3.4. As a result, p is overestimated for high amplitudes of y and in turn, the overall area of the loop is overestimated as well leading to a physical overestimation of equivalent hysteretic damping ratio (compared to experimental lab-results: $\approx 20 - 30\%$, 2.3.1). Incorporating soil strength degradation will lead to substantial increase in pile response when compared to the case with static p-y curves [33, 32]. Also, there are no signs of rate effects and no ratcheting effects. In terms of geometric soil-pile behaviour one could say that the PySimple1 element is mainly designed to incorporate the effects of gapping. The results obtained seem consistent with the conclusions of research conducted by [41] on the performance of the Boulanger element under seismic loading. Additionaly, the author concluded that both the acceleration response spectra and the obtained hysteretic loops are significantly different from a reference (verified against two different centrifuge tests) continuum model. Yet, the author concludes that the maximum bending moment along the pile shaft is acceptably predicted for the Winkler approach with Boulanger elements.

Taking the aim of this thesis in consideration (which is on the assessment of a method on finding and applying equivalent hysteretic damping without the application of hysteresis in itself), the simulation of more accurate unloading-reloading paths compared to measurement data (and more accurate backbone, initial load-paths) are considered to be outside the scope. As well as accurate values of soil damping compared to measurement data. Nonetheless, it is crucial to be aware of the limitations of any applied reference soil-structure interaction element in order for any results to make sense. Taking the element limitations into account, the choice of taking the PySimple1 material model as reference element is still substantiated because the element is calibrated against the throughout literature heavily applied and researched API regulation and is therefore thought to be a strong basis of comparison and assumed to be a strong stepping-stone towards any set of backbone plus unloading-reloading rules.

3.3.2 Identification of Parameters

User-Defined Parameters

1. Soil Type: The implementation of the dynamic spring element in OpenSees currently enables the user to use two different sets of soil types each representing two different sets of fixed parameters: c, n, C_e, and C_r to approximate the backbone relations as presented in Figure 3.3 for sand, drained conditions ($c = 0.5$, $n = 2$, $C_e = 0.542$, and $C_r = 0.2$) and soft clay, undrained conditions ($c = 10$, $n = 5$, $C_e = \frac{1}{8C_r^2}$, and $C_r = 0.35$), respectively under static/monotonic loading conditions. This leads to limited options for the user in defining the material properties through backbone relations as the shape of the curves is hard coded into the OpenSees material object.

2. Ultimate Capacity $\mathbf{p_{ult}}$: The user has the freedom to specify the ultimate capacity of the p-y material which directly indicates the reaction force magnitude of the p-y backbone curve which the specified soil type is approximating. Increasing/decreasing the parameter increases/decreases the stiffness of the material in the process. The proposal of Matlock [30] is used for defining the ultimate capacity of soft clay and the method according API [3] for defining the ultimate capacity for sand since the p-y relationships are approximated using the hard-coded values specified under the soil type above. For clay the ultimate capacity is described by:

$$
\begin{gathered}
p_{u1} = \left(3 + \frac{\gamma'}{c_u} z + \frac{J}{D} z\right) c_u D \\
p_{u2} = 9 c_u D \\
p_{ult} = \min\left(p_{u1}, p_{u2}\right)
\end{gathered}
\tag{3.19}
$$

Where:

D: is the pile diameter;

$\gamma\prime$: is the effective unit weight of soil;

c_u: is the undrained soil shear strength;

z: is the depth from ground surface;

J: is a constant with values ranging $0.25 \leq J \leq 0.5$ determined by field testing. Matlock et al. [30] indicates that 0.5 is used to represent soft clay (as found from field tests conducted in the Gulf of Mexico) from which the PySimple1 element is calibrated against. Lower values of J indicate more stiffer clay's.

For sand the ultimate capacity is described by:

$$\begin{aligned} p_{u1} &= (C_1 z + C_2 D)\,\gamma' z \\ p_{u2} &= C_3 D \gamma' z \\ p_{ult} &= \min\left(p_{u1}, p_{u2}\right) \end{aligned} \tag{3.20}$$

Here, the constants C_1,C_2,C_3 may be determined graphically from figure 6.8.6-1 [3]. For numerical implementation, the ultimate capacity may also be determined numerically:

$$\begin{aligned} p_{u1} = A\gamma' z \Bigg[& \frac{K_0 z \tan\phi \sin\beta}{\tan(\beta-\phi)\cos\alpha} + \frac{\tan\beta}{\tan(\beta-\phi)}\left(D + z\tan\beta\tan\alpha\right) \\ & + K_0 z \tan\beta\left(\tan\phi\sin\beta - \tan\alpha\right) - K_a D \Bigg] \\ p_{u2} = A\gamma' z & \left[K_a D\left(\tan^8\beta - 1\right) + K_0 D \tan\phi \tan^4\beta\right] \\ p_{ult} = & \min\left(p_{u1}, p_{u2}\right) \end{aligned} \tag{3.21}$$

Where:

K_0: equals the coefficient of earth pressure at rest generally taken as $K_0 = 0.4$;

ϕ: equals the friction angle of the sand in radians;

$\beta = \frac{\pi}{4} + \frac{\phi}{2}$;

$\alpha = \frac{\phi}{2}$;

$K_a = \tan^2\left(\frac{\pi}{4} - \frac{\phi}{2}\right)$ to denote the active earth pressure.

3. Displacement at 50% Ultimate Capacity: $\mathbf{y_{50}}$: The displacement at which 50% of the ultimate capacity of the p-y material has been mobilized is specified as direct input of the material model. The parameter has direct effect on the shape of the backbone curve as the ultimate capacity of the material is reached at a lower/higher displacement amplitude if the value is decreased/increased, stretching the backbone curve over displacement amplitude. As the material model is setup as such that it provides initial elastic behaviour, the duration of linear elastic behaviour increases accordingly. The proposal of Matlock [30] is used for defining the y_{50} displacement of soft clay and method according API [3] for defining the y_{50} displacement for sand since the p-y relationships are approximated using the hard-coded values specified under the soil type above. For clay, the y_{50} displacement value is described by:

$$y_{50} = 2.5\epsilon_{50} D \tag{3.22}$$

Here ϵ_{50} is the strain which occurs at one-half of the maximum stress on a laboratory stress-strain curve. A value may be assumed in the range of: $0.005 \leq \epsilon_{50} \leq 0.020$ representing stiff/brittle clays for low values and soft clays for high values. Matlock et al. [30] indicates that $\epsilon_{50} = 0.010$ is probably satisfactory for most purposes and the Boulanger element was calibrated for $\epsilon_{50} = 0.005$ based on published laboratory tests [5]. For sand, the y_{50} displacement value may be taken as:

$$y_{50} = \frac{A p_{ult}}{kz} \operatorname{arctanh}\left(\frac{0.5}{A}\right) \tag{3.23}$$

The value for the subgrade modulus k is given by graph in [3]. However, [43] presents the following equations to find a value in a numerical manner based on a curve-fitting procedure for both below the water table and above, respectively:

$$\begin{aligned} k &= 10.237 D_r^2 + 12.498 D_r \\ k &= 4.7541 D_r^2 + 90.106 D_r \end{aligned} \tag{3.24}$$

Here, D_r is the relative density which may be approximated by another formulation based on curve fitting:

$$D_r = 1643206.6\phi^5 - 5083287.6\phi^4 + 6275860.5\phi^3 - 3865226.8\phi^2 + 1187798.4\phi - 145708.4 \tag{3.25}$$

4. **Drag Resistance Within Fully Mobilized Gap: $\mathbf{C_d}$:** The user can specify the drag force resistance of the p-y material within a gap in terms of $C_d * p_{ult}$ to simulate the formation of a gap between the soil and pile. The parameter only has influence on the gap component (in terms of drag and closure) within the dynamic spring and has therefore no effect on the initial load path. Increasing/decreasing the drag resistance parameter has notable effect on the shape of the hysteretic loops as increasing/decreasing the drag resistance parameter increases/decreases the magnitude of soil resistance after mobilization of a full gap. Only the drag force (which is less than the soil resistance) can be taken by the soil layers when the pile starts moving in the previously created gap. This result leads to a so called "bow-tie shape" (Figure 3.4) if no resistance within a gap to no sign of a gap if the parameter is increased to ≥ 1.0. Increasing the value increases therefore the amount of energy dissipation by the material after the formulation of this gap. Memarpour et al. [32]

claims that the drag coefficient has no important effect on overall peak pile response results.

5. Viscous Damping Term to Simulate Radiation Damping: $\mathbf{c}$: The user is given the option to include viscous damping to simulate the effect of radiation damping. If no value is specified, then the default of zero damping is used meaning no influence of the viscous damper and no influence of radiation damping. Because hysteretic damping originating from the nonlinear plastic soil state is assumed to be prone, the Radiation damping contribution is disregarded throughout this thesis.

Hard-Coded Parameters

The parameters discussed here are not directly defined as input by the user but are fixed values hard coded within the PySimple1 material object. As the user can define the soil type – soft clay or sand – these soil types come with a specific set of parameters that ultimately defines the shape of the backbone curve.

6. Tangent Modulus Constant: $\mathbf{c}$: The tangent modulus constant has direct influence on the nonlinear portion of the backbone curve: the plastic spring. Through increasing the value, the shape of the curve returns softer behaviour in the plastic region and through decreasing of the value stiffer behaviour. The parameter must not be confused with the initial tangent modulus of the nonlinear portion of the backbone curve as that is defined by its tangent stiffness: k^p at $y^p = y_0^p$.

7. p-y Curve Sharpness Constant: $\mathbf{n}$: The variation of the sharpness constant of the p-y curve returns roughly the same behaviour as the tangent modulus constant. One noticeable difference is that the ultimate capacity p_{ult} is reached at a later displacement while lowering the value of the constant compared to the tangent modulus constant.

8. Linear Far-Field Spring Constant: $\mathbf{C_e}$: Varying the linear far-field spring constant has direct effect in terms of increasing/decreasing the constant linear elastic initial stiffness portion of the backbone p-y curve. Consequently, the load at yield point p_0 is reached at different values for displacement due the varying initial stiffness k^e. The parameter yields from great importance as the shape of the hysteretic loops are directly related to this linear initial stiffness: a higher initial stiffness results in a much greater loop area as the loop shape is mostly characterized by its initial load-path.

9. Rigidness Region Plastic Spring Constant: $\mathbf{C_r}$: As the region in which the dynamic spring is defined to behave plastic is defined by the region presented in equation 3.7 and the load at yield point p_0 is therefore directly related to this parameter it is clear that by increasing the rigidness region plastic spring constant parameter, the linear elastic region is stretched over force and displacement amplitude. It must be obvious that by increasing the linear-elastic path in the initial load-path, the damping mechanism occurring from hysteresis remains absent as long as the plastic spring behaves rigid.

3.3.3 Calibration of Soil Springs for Dynamic Analyses

Through the soil- and structural properties presented in 3.1 and the identified procedure in 3.3.2, the dynamic springs representing the soil-pile interaction mechanism can be calibrated. The main point of focus are the direct user-input parameters. The two specific sets (sand and clay) of hard-coded parameters approximate the throughout research heavily used API and Matlock curves (Figure 3.3). On top of that, working with the OpenSees source code and implementing own code is a tedious and time-consuming process. Therefore, the hard-coded parameters will remain untouched.

Calibration of User-Input Parameters

Conveniently enough, OpenSees provides an command (PySimple1Gen) constructing PySimple1 material objects along the embedment depth of the pile structure where values for p_{ult} and y_{50} are determined on basis of input soil and pile properties like the approach described in 3.3.2, hereafter denoted as the “API” approach as described in [3]. [3, 30, 42] all provide procedures in determining those two parameters for the two soil types directly available for implementation (though, all these p-y approaches are calibrated against slender piles). For numerical implementation, equations 3.19, 3.21, 3.22, 3.23, 3.24, and 3.25 are adopted. The approach in determining the drag coefficient in simulating the gapping behaviour between the soil and pile C_d is less systematic as this is site specific and therefore, generally found using field-testing in the simulation of soil-pile interaction. As the sand material type represents drained conditions, it is assumed that the sand has no capacity in standing on its own and no potential in forming a gap. The total force across the p-y material is restricted to p_{ult} in magnitude so the value of $C_d = 1.0$ is adopted for baseline analyses for sand. Back-calculated p-y curves from centrifuge experiments suggest that $C_d \approx 0.3$ would be reasonable for soft clay [5] and will therefore be adopted for the baseline analyses. Because the Boulanger element was calibrated for $\epsilon_{50} = 0.005$ based on published laboratory tests, this value is adopted for baseline analyses. Because the hard-coded p-y formulation represents a short-term static load-case, the procedure in formulating the PySimple1 spring input properties focuses solely on the static properties to be considered in the equations mentioned above. For reference, a total overview is given of all identified parameters relevant in specifying the tangent stiffness in dynamic reponse, equation 3.18:

Soil Type	p_{ult}	y_{50}	C_d	c_{rad}	c	n	C_e	C_r	J	K_0	ϵ_{50}
1: Clay	eq. 3.19	eq. 3.22	0.3	0.0	10	5	1.02	0.35	0.5	-	0.5%
2: Sand	eq. 3.21	eq. 3.23	1.0	0.0	0.5	2	0.542	0.2	-	0.4	-

Table 3.3: Overview of PySimple1 parameters

Resulting Sets of Layered *p-y* Curves

Considering the soil characteristics presented in 3.1.1, and geometry input as presented in 3.1.2 the embedded (depth-dependent) nonlinear hysteretic PySimple1 springs can be calibrated using the numerically implemented equations as specified above. Following the depth dependent soil characteristics, the total depth-dependent p-y curve set directly related to the depth-dependent spring stiffness can be visualized and is presented in Figure 3.5.

The spring stiffness increases under increasing embedment depth (decreasing z relative to the mudline) as a result of the increasing ultimate spring capacity. It is noticeable that the clay soil layers return a constant value of y_{50} because of a constant ϵ_{50} input (equation 3.22 is depth independent) originating from laboratory testing and a substantially higher value compared to that of the sand layers. This indicates that sand is a much stiffer layer compared to that of clay. Considering the results presented above, the resulting sets of layered and depth-dependent p-y curves can be visualized in Figure 3.6. Here, the reaction force p versus lateral displacement y is plotted over embedment depth z.

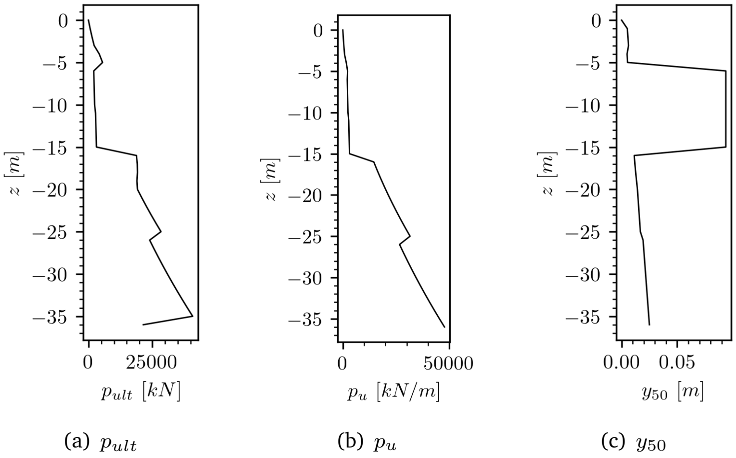

(a) p_{ult} (b) p_u (c) y_{50}

Figure 3.5: Overview of corresponding input parameters of embedded soil springs

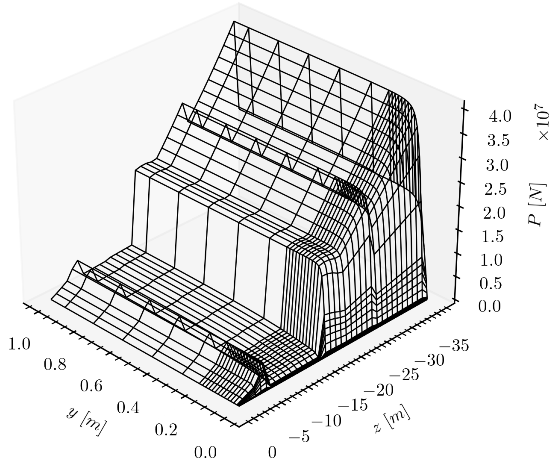

Figure 3.6: Overview of p-y sets based on soil- and OWT characteristics

3.4 Time Incremental Pushover Validation

BHawC (Bonus Horizontal axis wind turbine Code) is used to compare and verify the global lateral response of the equivalent OWT model created in OpenSees. For this exercise any additional aeroelastic loads are excluded. The BHawC analysis used the same geometric and constitutive parameters defined in the OpenSees analysis (3.1 and 3.3.3). Response is compared upon application of both a lateral force and bending moment just below mudline. The loads are gradually increased from $t = [10, 550]s$ with total analysis duration of $600s$. The situation presented in Table 3.4 is investigated where both force and bending moment are applied just below mudline: $z = -1m$. The result is found in Figure 3.7. Overall, the agreement between the OpenSees and BHawC analyses verifies that the OpenSees implementation is capable of returning sensible results for laterally-loaded pile simulations.

$F_{y,0}$ $[N]$	$F_{y,1}$ $[N]$	$M_{x,0}$ $[Nm]$	$M_{x,1}$ $[Nm]$
10	26700000	10	1200000000

Table 3.4: Load Characteristics of Pushover Validation

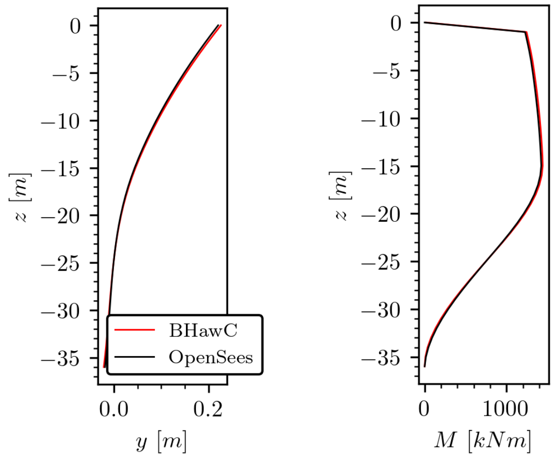

(a) Lateral displacement (b) Bending Moment

Figure 3.7: Overview of the lateral pushover response

Chapter 4

Equivalent Viscous Damping

Recommended practice specifies that whenever the implemented soil-structure interaction springs are **not** fully nonlinear and inelastic, the application of nonlinear hysteretic damping may be simplified and linearized to support linear elastic analyses [12]. Upon application of Masing rules the amount of energy dissipation is then approximated and reduced to overcome the physical amount of overdamping compared to laboratory test results (not to get confused with the term presented earlier in 2.2.1). Because the target response (hysteretic PySimple1 soil-pile springs) may be simulated prior, this chapter will focus on the exercise of back-calculating damping observed from plastic time-domain response. Please note that in practice the maximum level of spring extension is unknown before the analysis.

4.1 Classical Equivalent Damping Ratio

Considering the energy quantities from the balance of forces / equation of motion in equation 2.2, the equivalent damping ratio ζ (which represents the equivalence of the hysteretic damping mechanism) in equation 2.9 is derived. The total energy in the nonlinear single degree of freedom system (Figure 2.5) can be obtained by integrating the single degree of freedom equation of motion with respect to the displacement response [47]. Each (rewritten) term represents a different form of energy in the system: kinetic energy E_k, dissipated energy by the viscous damper E_d, dissipated energy by yielding and recoverable strain E_{y+s}, and imparted energy E_i, respectively:

$$E_k = m \int_0^t \ddot{u}(t)\dot{u}(t)dt = \frac{1}{2} m\dot{u}^2(t) \tag{4.1}$$

$$E_d = c \int_0^t \dot{u}^2(t)dt \tag{4.2}$$

$$E_{y+s} = \int_0^t f_s\left(u(t), \text{sign}(\dot{u}(t))\right)\dot{u}(t)dt \tag{4.3}$$

$$E_i = -m \int_0^t \ddot{u}_g(t)\dot{u}(t)dt \tag{4.4}$$

The energy dissipated by the hysteretic loop and of the system entering the nonlinear plastic regime can be obtained by subtracting the recoverable strain energy E_s.

$$E_s = \int_0^u ku(t)du = \int_0^t ku(t)\dot{u}(t)dt \tag{4.5}$$

$$E_y = E_{y+s} - E_s = \int_0^t f_s\left(u(t), \text{sign}(\dot{u}(t))\right)\dot{u}(t)dt - \int_0^t ku(t)\dot{u}(t)dt \tag{4.6}$$

The total energy dissipated in the nonlinear SDoF system subjected to a ground motion then yields:

$$E_y + E_d = \int_0^t f_s\left(u(t), \text{sign}(\dot{u}(t))\right)\dot{u}(t)dt - \int_0^t ku(t)\dot{u}(t)dt + c\int_0^t \dot{u}^2(t)dt \tag{4.7}$$

Equation 2.9 is then derived upon the major assumption that the steady-state displacement response is perfectly harmonic: $u(t) = U\cos(\omega t)$, upon which the velocity response is assumed perfectly harmonic as well: $\dot{u}(t) = -U\omega\sin(\omega t)$. The energy dissipated by a viscous damper in single degree of freedom formulation over one load cycle then yields:

$$E_d = \int_0^{\frac{2\pi}{\omega}} cU^2\omega^2\sin^2(\omega t)dt = \pi c\omega U^2 \tag{4.8}$$

Using the relationship of equivalent viscous critical damping (equation 2.4) the energy dissipated during one cycle can be expressed as:

$$E_d = 2\pi\zeta\sqrt{km}\omega U^2 = 2\pi\zeta\omega\omega_0 U^2 m = 2\pi\zeta\frac{\omega}{\omega_0}U^2 k \tag{4.9}$$

Considering the relationship of the maximum stored elastic energy for a purely linear spring (equation 4.5) one can derive and express the equivalent viscous damping ratio as the ratio between the energy dissipated by a viscous damper and maximum stored strain energy:

$$\zeta = \frac{1}{4\pi}\frac{\omega_0}{\omega}\frac{E_d}{E_s} \tag{4.10}$$

Apparently the equivalent viscous damping ratio of a linear single degree of freedom system does not only depend on ratio between the dissipated energy over maximum stored energy, but also on the ratio between natural frequency of oscillation and forcing frequency/frequency of excitation. The hysteretic damping to be approximated is generally frequency independent [29]. To overcome frequency dependency the assumption is made of $\omega = \omega_0$. Something which seems to be consistent throughout literature [19, 22, 34].

4.2 Equivalent Damper Coefficient

4.2.1 Peak Alignment

Dowgala et al. [15] presents an interesting yet plain method in obtaining mass-normalized equivalent viscoelastic damping coefficients based on known hysteretic response. A mass-normalized damping coefficient multiplied by the relative velocity is empirically added to the equation of motion to force the peak in the absolute acceleration to shift in time to align with the time instant the relative velocity is zero. Considering equation 2.2 for $F(t) = 0$ (free-vibrations), that should then be equal to the (mass-normalized) restoring force: $\ddot{u}(t) + \frac{c}{m}\dot{u}(t) = -\frac{k}{m}u(t)$. In the knowledge that the time instances where restoring force is peaked should be equal to the time instances that the relative velocity crosses zero the following equations can be solved for time and set equal to find the damping in the system. This procedure is demonstrated in equations 4.11 and 4.12 for an (underdamped) harmonic solution in equation 2.5. The result is the theoretical expression of critical damping presented earlier in equation 2.4. The method is demonstrated in Figure 4.1 for an arbitrary seismic signal applied to a single degree of freedom support.

$$\begin{gathered}\frac{d}{dt}\left[\ddot{u}(t)+\frac{c}{m}\dot{u}(t)\right]=0\longrightarrow tan(\omega t+\phi)^{(1)}=\frac{-3\zeta^2\omega_0^2\omega+2\frac{c}{m}\zeta\omega_0\omega+\omega^3}{\frac{c}{m}\zeta^2\omega_0^2-\zeta^3\omega_0^3+3\zeta\omega_0\omega^2-\frac{c}{m}\omega^2}\\ \dot{u}(t)=0\longrightarrow tan(\omega t+\phi)^{(2)}=\frac{\omega}{\omega_0\zeta}\end{gathered} \tag{4.11}$$

$$tan(\omega t+\phi)^{(1)}=tan(\omega t+\phi)^{(2)}\longrightarrow c=2m\zeta\omega_0\longrightarrow\zeta=\frac{c}{2m\omega_0}=\frac{c}{2\sqrt{km}} \tag{4.12}$$

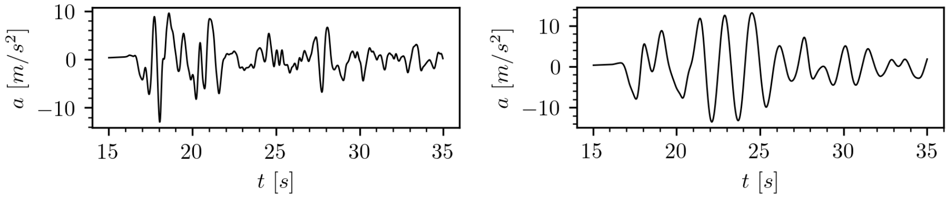

(a) Applied signal (b) Acceleration

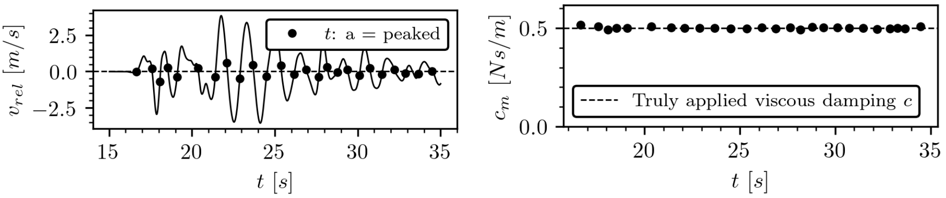

(c) Relative velocity (d) Back-Calculated c

Figure 4.1: Overview of the peak alignment procedure for applied viscous damping to a linear SDoF

4.2.2 Energy Quantities

Instead of relating the damping to the ratio of energy dissipation to recoverable strain energy in many situations it would make most sense to relate the damping directly to the true dynamic response, disregarding the thorough assumptions upon derivation of equivalent damping (4.1). Using a same energy based approach in derivation of equivalent damping, an equivalent damper coefficient c, can be calculated. The method is thus closely related to that of the prescribed one back in [12]. A damper coefficient is found by setting the energy dissipated by a viscous damper E_d (equation 4.2) equal to the energy dissipated by hysteresis E_h. We know that the latter is equal to the area enclosed by the unloading and reloading paths. Subsequently, an equivalent damper value can be solved for:

$$c_{eqe} = \frac{A_{loop}}{\int_{t=\tau-1}^{t=\tau+1} \dot{u}^2(t)dt} \tag{4.13}$$

Note that equation 4.13 depends directly on the response considered in the $t = [\tau - 1, \tau + 1]$ range, where $t = [\tau - 1, \tau + 1]$ represents the time for a single loop to close.

4.3 Method

4.3.1 Equivalent Viscous Damping Ratio

In relation towards the application of equivalent viscous damping on a structural system, (relative) displacement dependent equivalent damping ratio curves are usually constructed (or in the case of soil deposits, shear strain dependent curves) to address a single equivalent damping value based on a single equivalent relative displacement [12, 8, 56, 36, 29, 44, 52, 58, 60]. In practice, it is possible to construct hypothetical loops from a single backbone p-y curve adopting Masing rules. However, in approximation of arbitrary unloading-reloading behavior that deviates from Masing principle (unloading-reloading response that deviates from the backbone curve shape) one could construct curves based on the hysteretic steady-state response. The single degree of freedom system is loaded into the steady-state regime using an harmonic force with forcing frequency equal to the natural frequency (that of the initial stiffness, that is) of the single degree of freedom oscillator. The plastified steady-state displacement response amplitude is then measured for multiple displacement amplitudes (induced by conducting the same analysis for multiple harmonic forcing amplitudes) and linked to the loop area: the 'identified loop'. This procedure is visualized in Figures 4.2 and 4.3. Notice how in the steady-state only a maximum of $p = C_d * p_{ult}$ is possible, which is $p/p_{ult} = 1.0$ for sand and $p/p_{ult} = 0.3$ for clay.

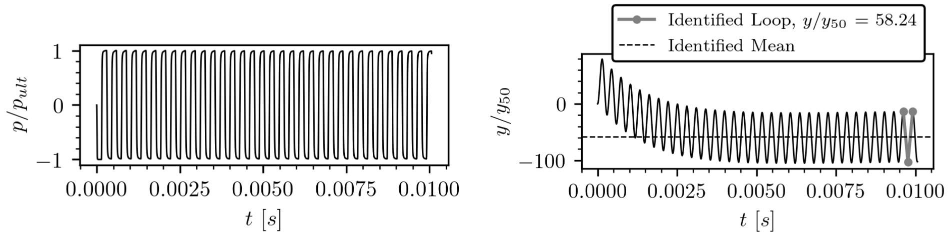

(a) Reaction force, sand (b) Displacement response, sand

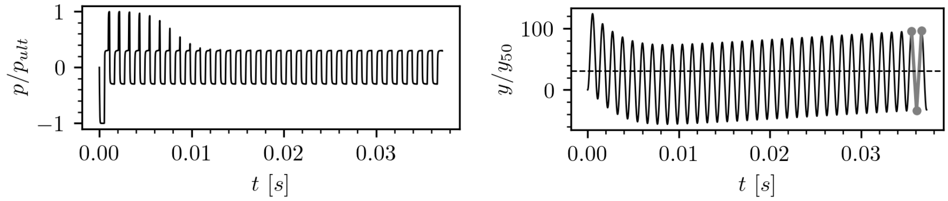

(c) Reaction force, clay (d) Displacement response, clay

Figure 4.2: Overview of the methodology in identifying hysteretic loop area

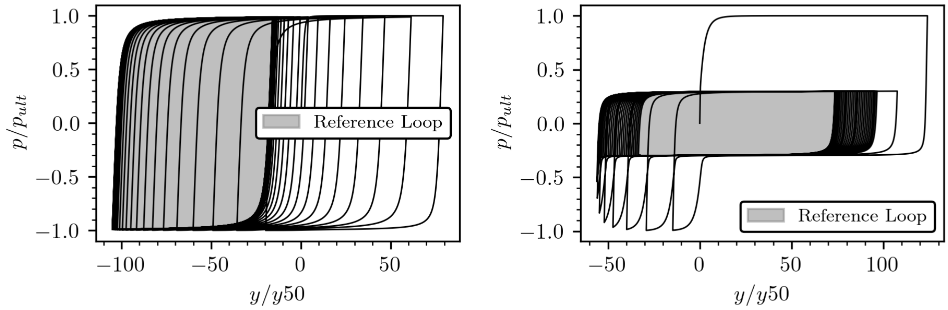

(a) Reference hysteretic loop, sand (b) Reference hysteretic loop, clay

Figure 4.3: Overview of the identified hysteretic loops

Permanent plastic displacements are clearly observable which can not be simulated during elastic analyses. On that note, the reference steady state displacement value is taken as the amplification relative to the mean value of steady-state (in this case plastified) displacement. Please note that significant plastified conditions are presented here and are only to demonstrate the method. In real-time soil-pile interaction analyses such significant permanent displacements are expected not to be of this magnitude. Repeating this same exercise for a range of forcing amplitudes one could measure associated reference loop area (or dissipated energy by hysteresis) and associated secant stiffness for each value of measured relative reference displacement. An equivalent viscous damping ratio is then found using equation 4.10 for every reference displacement. These results are visualized in Figure 4.4.

Indeed, the results associated with hard-coded sets for both sand and clay approximately follow the trends as observed earlier in 2.8. For both clay and sand the numerical effect of the drag force resistance parameter is directly observed and represented by a kink. This kink occurs after the ultimate capacity p_{ult} is reached in a previous load-cycle as earlier described in 3.3.1. For sand, the effect is a lot less dominant than for clay, directly related to the loop area observed in Figure 4.3. On top of that, the hard-coded backbone curve for clay has a longer initial elastic branch compared to sand (Figure 3.3). Such a long linear elastic branch seems to be inconsistent with literature.

4.3.2 Equivalent Damper Coefficient

Instead of computing the ratio of loop area to the recoverable strain energy (equation 2.9), the ratio is taken as loop area to the integral of velocity squared for an identified reference loop (equation 4.13). Upon multiplication of such equivalent damper coefficient with the velocity, an equivalent damping force is found in Figure 4.5. The damper coefficient gradually decays over increased speed of oscillation (increasing denominator, equation 4.13). The magnitude of the coefficient increases with soil stiffness. As a result of both decrease in loop area in the steady-state regime (because of gapping) and increase in integrand of squared velocity, the decay of the damper coefficient for clay soils happens more instantaneous and magnitude is lower overall compared to sand. The back-calculated damping force perfectly follows the equivalent damping ratio ζ observed earlier for sand. For clay the distribution tends to deviate after the ultimate capacity has been reached and the magnitude of (steady-state) damping force is significant lower than compared with sand. The latter is the numerical result of pinching/gaps: reduction of ultimate capacity in the steady-state regime compared to the maximum observed throughout the total timeseries.

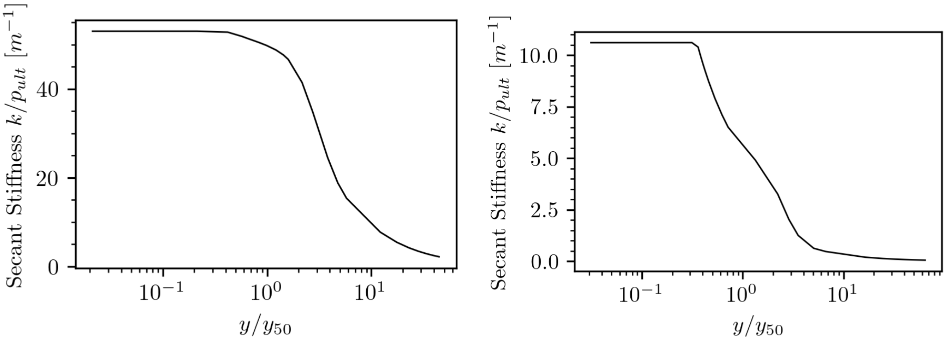

(a) Secant stiffness versus displacement sand

(b) Secant stiffness versus displacement clay

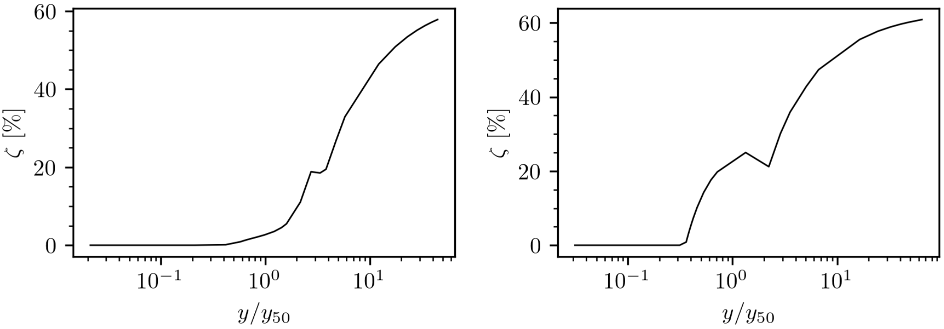

(c) Equivalent damping ratio for sand

(d) Equivalent damping ratio for clay

Figure 4.4: Overview of global equivalent damping ratio curves for the PySimple1 element

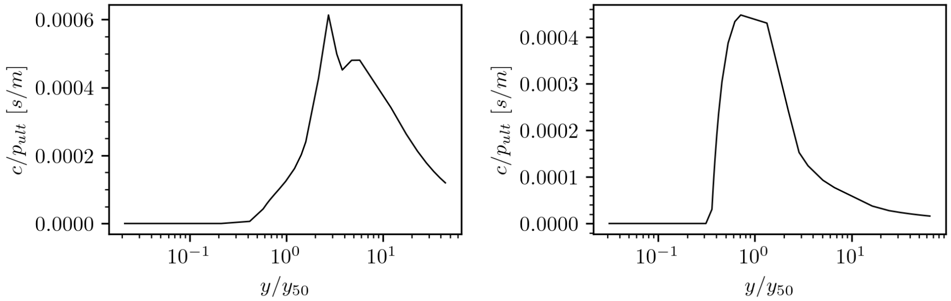

(a) Damper coefficient for sand

(b) Damper coefficient for clay

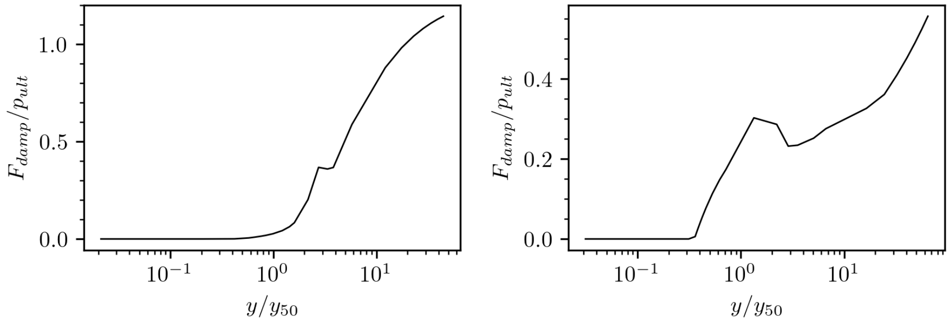

(c) Damping force ($F = c\dot{u}$) for sand

(d) Damping force ($F = c\dot{u}$) for clay

Figure 4.5: Overview of global equivalent damper coefficient curves for the PySimple1 element

4.3.3 Equivalent Viscous SDoF

Single degree of freedom response is compared in Figures 4.6 and 4.7 for an arbitrary harmonic forcing amplitude F_0. In order for the equivalent damping ratio ζ to be applied, it is chosen to apply (initial) stiffness proportional damping which is a modal damping where the damping ratio increases linearly over frequency. The (constant valued after relating the frequency equal to the (linear) natural frequency of the oscillator and stiffness equal to the initial stiffness of the nonlinear spring) damper coefficient then reads $c = \alpha_1 k_{ini}$ where $\alpha_1 = \frac{2\zeta}{\omega_0}$. Here, the reference equivalent damping value is taken from the constructed equivalent damping curves found in Figures 4.4 and 4.5 with reference displacement measured from the steady-state hysteretic response. Without the available information of ”true” hysteretic response, which is generally the case in practice, values for equivalent damping may be taken using relative displacements from an elastic case and applied in an iterative manner.

Upon comparison of the steady-state hysteretic response with equivalently damped response in Figures 4.6 and 4.7, it is observed that next to the fact that the steady-state hysteretic response provides permanent displacements, the back-calculated equivalent damping ratio ζ underestimates the response in application of a nonlinear but elastic spring. This is the result of upon derivation of equation 4.10 where the maximum stored energy is taken as that of a linear elastic secant stiffness. With nonlinear springs the stiffness is updated each time instance leading to an underestimation of maximum potential energy. An observation earlier made by [22, 19]. The equivalently damped linear elastic spring model provides good agreement. The same agreement is found in application of a back-calculated equivalent damper coefficient which is directly based on the hysteretic response. Both nonlinear but elastic and linear elastic springs provide good agreement when hysteretic velocity response is used in calculating c. Figure 4.6 provides the steady-state response of the models where the hysteretic model is subjected to permanent displacement. By substraction of the mean steady-state response in Figure 4.7, the agreement in amplification is verified.

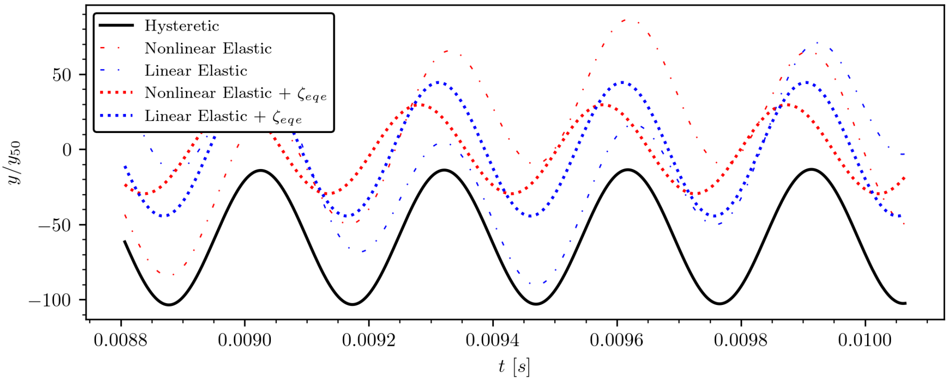

(a) Equivalent damping ratio ζ

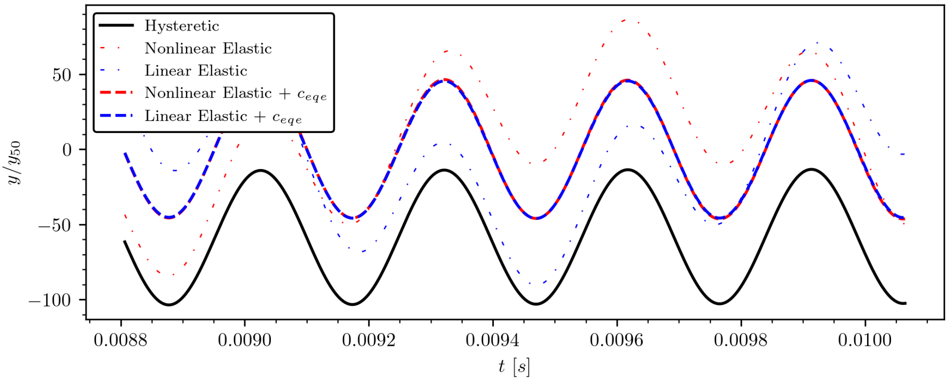

(b) Damper coefficient c

Figure 4.6: Comparison of time domain steady-state equivalent damping response

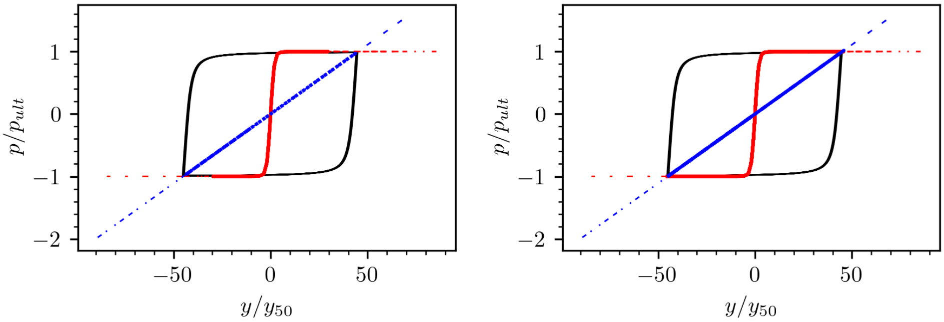

(a) Equivalent damping ratio ζ (b) Damper coefficient c

Figure 4.7: Associated force-displacement curves, with substraction of mean steady-state response

4.4 Arbitrary Excitation

Up until now, the assessment has been limited towards the identification of perfect harmonic oscillations and the identification of reference loops in the steady-state regime. In relation to multi-harmonic excitations, and especially in the case of stochastic seismic excitations, it is not always clear which loop area is to be taken as reference. To overcome this loss of information throughout the whole timeseries, [46] proposes a method that assesses each of the unloading and reloading branches individually (each half of a full loading cycle). The method enables the estimation of a damping ratio for each of the loading increments composing such half loops. As a result, a continuous variation of damping ratio with time can be evaluated. In that regard, the method provides valuable insight into which soil-structure interaction components (layers of soil deposits, essentially) are responsible for most of energy dissipation.

The proposed method relates the energy accumulated during an arbitrary stress-strain path $E_{acc,i}$ to the elastic energy $E_{el,i}$ within this region between two stress reversal points: $(\gamma_{rev}, \tau_{rev}), (\gamma_i, \tau_i)$. The accumulated energy and elastic energy in the region are:

$$E_{acc,i} = \int_{\gamma_{rev}}^{\gamma_i} (\tau - \tau_{rev}) d\gamma \tag{4.14}$$

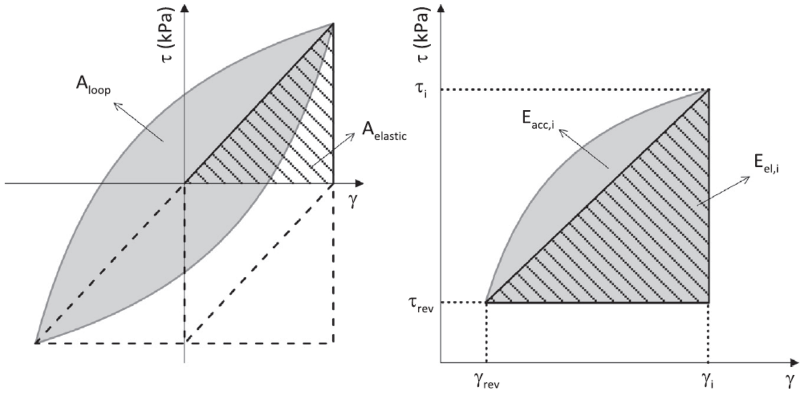

Figure 4.8: Areas used in the evaluation of the damping ratio and definition of accumulated energy and elastic energy [46]

$$E_{el,i} = \frac{1}{2}(\tau_i - \tau_{rev})(\gamma_i - \gamma_{rev}) \tag{4.15}$$

To extend the algorithm for a hypothetical full-cycle, the current stress-strain path (or p-y path for that matter) is related to a full loop area as is done in Figure 4.8. Please note that following this procedure it is assumed that to close a hypothetical full-cycle, the unloading or reloading branch is an inverted replica of the previous load-cycle. True cycles may deviate under large-strain stochastic vibrations. Still each cycle is assessed separately, and because both the loop area and integral of squared velocity are scaled by two this information loss remains limited (both the numerator and denominator are scaled by two). A back-calculated equivalent viscous damper coefficient is considered representative and valid for each separate load-cycle. In that way, the proposed method is insightful in stochastic excitations. The relations for a full cycle transform to:

$$E_h = A_{loop} = 2(E_{acc,i} - E_{el,i}) \tag{4.16}$$

$$E_p = A_{elastic} = \frac{E_{el,i}}{4} \tag{4.17}$$

Upon adoption of equations 4.10 and 4.13, the classical equivalent viscous damping ratio and damper coefficient assessed for each individual load-path then yield, respectively:

$$\zeta_{eqe,i} = \frac{1}{4\pi}\frac{E_h}{E_p} = \frac{1}{4\pi}\frac{2(E_{acc,i}-E_{el,i})}{\frac{E_{el,i}}{4}} = \frac{2(E_{acc,i}-E_{el,i})}{\pi E_{el,i}} \tag{4.18}$$

$$c_{eqe,i} = \frac{A_{loop}}{\int_{t=t-1}^{t=t+1}\dot{u}^2(t)dt} = \frac{2(E_{acc,i}-E_{el,i})}{2\int_{\gamma_{rev}}^{\gamma_i}\dot{\gamma}(t)d\gamma} \tag{4.19}$$

While the method may be adopted for arbitrary load-paths, the single-harmonic timeseries considered earlier in 4.3.3 is visualized first. To demonstrate the effectiveness of the algorithm and applicability independent of unloading-reloading rule, pinching (representing soil-pile separation) is included in the following results. This timeseries was presented earlier as the response for a clay spring in 4.3.1. The algorithm is adopted to identify the amount of equivalent damping present in the hysteretic timeseries. A single-degree of freedom system with an equivalent elastic spring in parallel with a constant equivalent viscous damper is able to accurately calculate the steady-state displacement amplification of an hysteretic system subjected to pinching, presented in Figure 4.9. The pinching effect only numerically occurs whenever the user-defined ultimate capacity is exceeded in an earlier load-cycle when using the PySimple1 material element (Figure 4.2). When conducting analyses while holding onto nonlinear but elastic backbone curve only, the reaction force in the steady-state regime will therefore be significantly overestimated without manual reduction of the ultimate capacity. This reduction of ultimate capacity is included in the linear elastic spring stiffness.

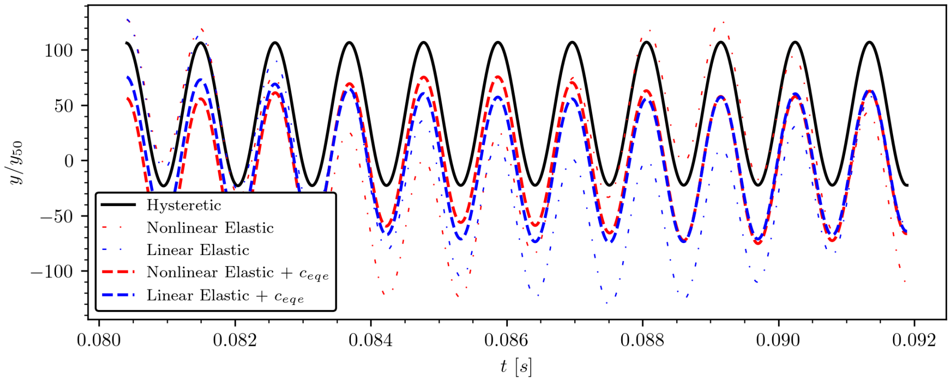

Figure 4.9: Hysteretic versus equivalently damped elastic steady-state displacement

The time varying energy quantities and related equivalent damping result are presented in Figure 4.10. Under a single harmonic force, the results follow the displacement response trend where eventually, in the steady-state regime convergence is found towards a single (peak) value of accumulated hysteretic energy, accumulated elastic energy, loop area, damping ratio, and damper coefficient. Any arbitrary hysteretic timeseries (which requires relative displacement, velocity, and reaction force as input) can be used to asses the time varying energy dissipation mechanism related to the timeseries in question using this aforementioned procedure.

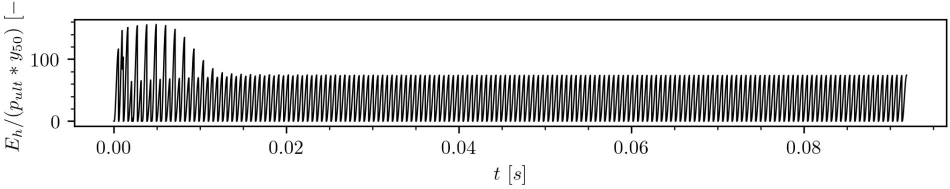

(a) Loop area

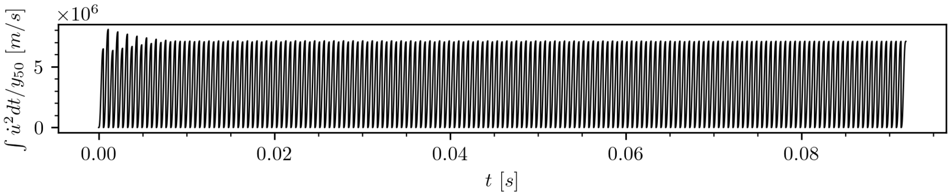

(b) Accumulated integrand of velocity squared

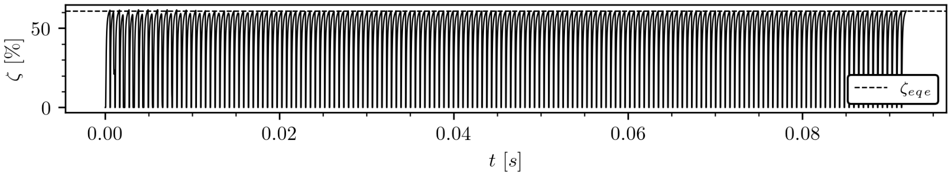

(c) Time varying equivalent damping ratio ζ

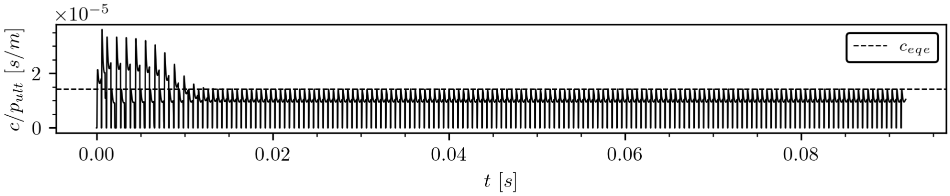

(d) Time varying equivalent damper coefficient c

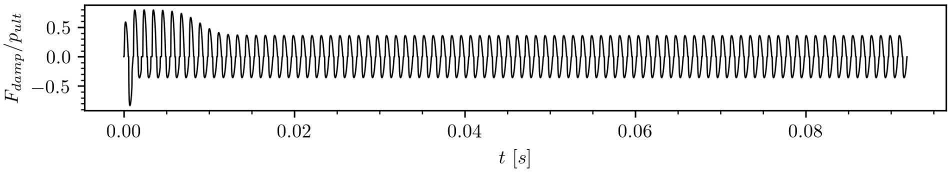

(e) Damping force

Figure 4.10: Time varying single harmonic energy dissipation and equivalent damping subjected to pinching

Chapter 5

Earthquake Response Analysis

To assess an equivalently damped elastic model that is supposed to represent the energy dissipation mechanism equivalent to an hysteretic model, we first need to know the amount of energy dissipation that each of the hysteretic soil-pile interaction springs produces. The amount of energy dissipation is directly related to the dynamic properties of the structure, calibration of the soil springs, but also to the applied input motion. Hence, it is difficult to know beforehand in practice how much energy dissipation to consider. Within this research the analysis results of the hysteretic model form the basis for determining the amount of energy dissipation on a local level to consider. Because the amount of damping is considered each spring separately, one could say that the damping is matched on a local-spring basis. Perfect agreement is therefore not to be expected. The following flowchart is presented to indicate the steps in formulation of the equivalently damped model:

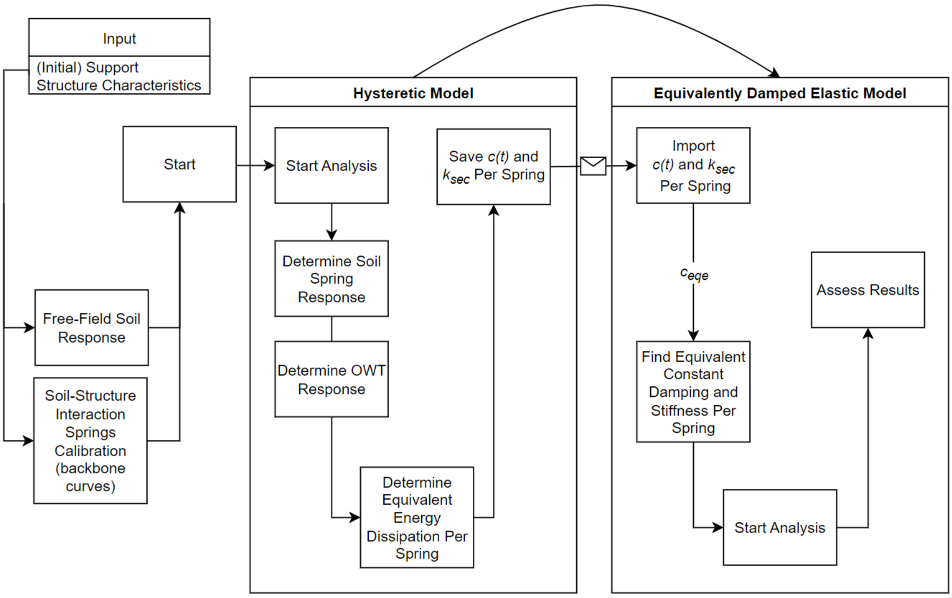

Figure 5.1: Flowchart of the adopted analysis procedure

5.1 Site Response Analysis

Three arbitrary but different signals were selected to asses the model. Because it is wrong to assume that a signal only applies to a single point or that the same signal applies for multiple points (or nodes), site response analysis is conducted to find depth-dependent input motions to be applied at each of the supports. The properties of the motions and results of the free-field site response to vertical shear wave propagation are presented below. Because the site response analysis is only considered as input to asses seismic response of the offshore wind turbine, no detailed attention is made towards the soundness and correctness of the free-field soil column response. In fact, the topic of site response analysis is something which is still thoroughly researched [36, 25, 55, 56, 57]. *ProShake* [16] is adopted to conduct one-dimensional equivalent linear frequency domain site-response analysis. For an extensive overview of the adopted equivalent linear frequency domain one-dimensional site response method, the interested reader is referred to [16].

5.1.1 Ground Motion at Bedrock

A seismic signal is applied at a bedrock layer connected to the bottom of a soil column with soil properties as given in Table 3.1. The following records were selected (Table 5.1 and Figure 5.2). It can be observed that the most important part of the motion, generally also known as the strong motion part approximately occurs between $t = 15s$ and $t = 30s$, $t = 15s$ and $t = 35s$, and $t = 15s$ and $t = 30s$, respectively. Considering the response spectra of the input motions, it can be observed that the frequency content of the acceleration input seeds are mainly contained between approximately $T = 0.1s$ and $T = 1s$ ($f = 1Hz$ and $f = 10Hz$).

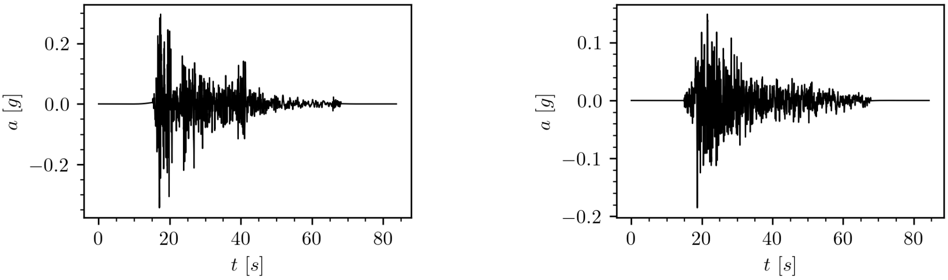

(a) Motion 1 at bedrock

(b) Motion 2 at bedrock

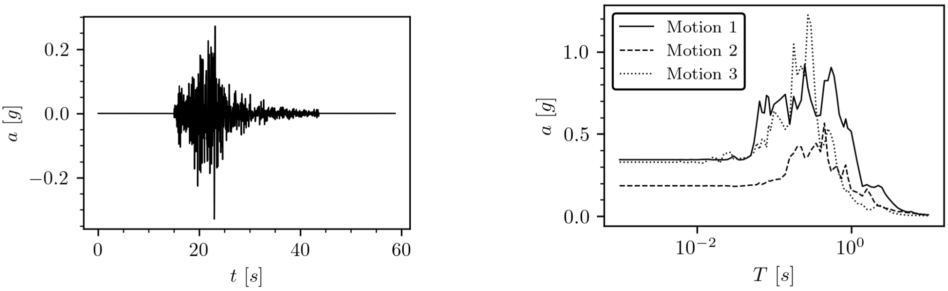

(c) Motion 3 at bedrock

(d) Response spectra

Figure 5.2: Overview of the applied signals at bedrock

	Event	M_w	PGA $[g]$
1	El Centro, California	6.95	0.344
2	Kern County, California	7.36	0.185
3	Northridge, California	6.69	0.329

Table 5.1: Selected ground motion records

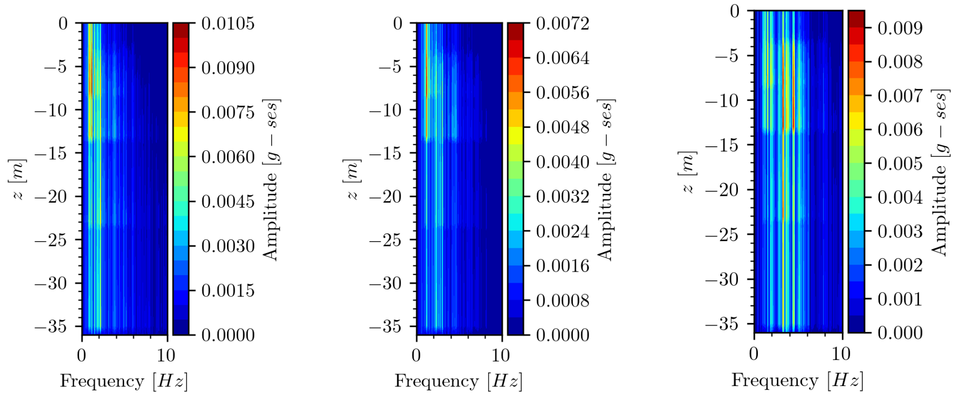

(a) Fourier spectrum over embedment depth, motion 1

(b) Fourier spectrum over embedment depth, motion 2

(c) Fourier spectrum over embedment depth, motion 3

Figure 5.3: Overview of the free-field frequency content

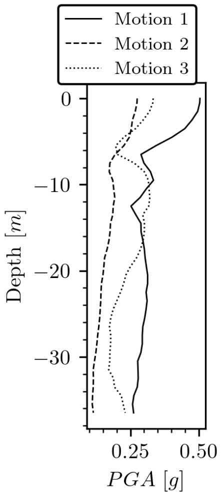

Figure 5.4: Overview of the free-field PGA response

5.1.2 Free-Field Response

Upon application of the selected seismic records from Table 5.1 onto a bedrock layer underlying the soil profile as presented in Table 3.1 the equivalent linear free-field response yields the following results to be applied and impose as motions onto the supports of the offshore wind turbine structure (Figures 5.3 and 5.4). Both the amplitude in terms of peak ground acceleration and the dominant frequency content vary according the geometric properties of the soil profile and the characteristics of the input motion.

5.2 Hysteretic Response Analysis

As the hysteretic beam on Winkler foundation model is considered to be the target model it is key that the model response, and especially the energy dissipation capabilities, is assessed extensively to substantiate, compare, and form a basis for any equivalently damped model. The depth-dependent free-field response of the different considered motions (5.1.2) are imposed as accelerations at the foundation model supports. No other source of damping is applied. The case of a single harmonic force with forcing frequency equal to the second natural frequency of the total structure (f_1: Table 5.2) applied just below mudline is discussed briefly first.

5.2.1 Single Harmonic Response

The depth-dependent identified hysteretic results of a single harmonic force applied just below mudline is found in Figure 5.5 using both equations 4.18 and 4.19. Because the amount of energy being dissipated by hysteresis is directly related to the loop area, one could argue that this energy dissipation mechanism is a function of both soil stiffness and relative displacement. Under the application of a single harmonic force just below mudline, the latter is found to increase gradually towards mudline and the soil stiffness decreases gradually towards mudline but is also soil type dependent. As a result, the identified value for a (depth-dependent) equivalent damper coefficient returns a shape which does not follow any of the aforementioned distributions. The observation was made earlier that for a clay-calibrated soil-spring a longer portion of linear elasticity is found, which is found again in the depth-dependent equivalent damper result. Because of this longer linear elastic branch, the sand calibrated soil-springs just beneath the clay layers may provide hysteresis where the first few clay layers still follow their linear-elastic branch. Whenever the clay layers do provide hysteresis, loop area is noticeably lower compared to that of sand because of lower ultimate spring capacity. In relation towards the Ultimate Limit State, back-calculated equivalent damping coefficients to be applied in equivalent damped analyses are found at the time-instance where the relative displacement response is peaked. These time-instances occur (in this case) simultaneously when the time-dependent nature of ζ is maximum, but not necessarily when the observed c is maximum.

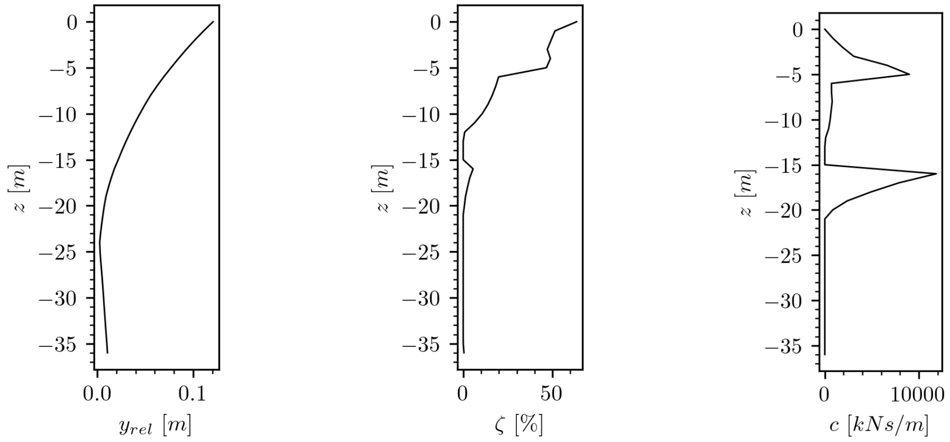

(a) Relative displacement

(b) Identified equivalent damping ratio ζ_{eqe}, eq. 4.18

(c) Identified equivalent damping c_{eqe}, eq. 4.19

Figure 5.5: Overview of the identified damping over embedment depth for sand

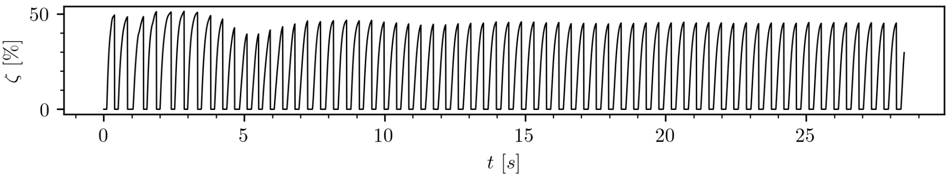

(a) Time varying equivalent damping ratio ζ_{eqe} at $z = -1m$, eq. 4.18

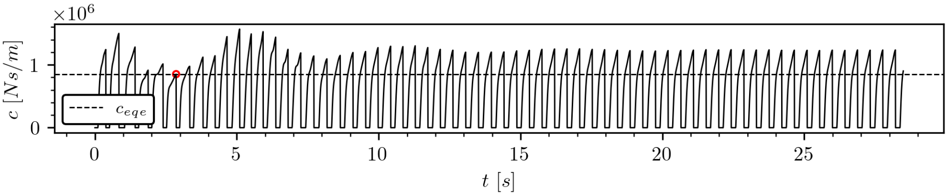

(b) Time varying equivalent damping c_{eqe} at $z = -1m$, eq. 4.19

Figure 5.6: Time varying single harmonic equivalent damping for the OWT model at $z = -1m$

For good reference, results on the soil spring just below mudline is shown in Figures 5.6 and 5.7. Here, the identified equivalent values are indicated. The amount of energy that is being dissipated over time is largest during the first few cycles between $t = 0 - 5s$: both observable in Figure 5.7 by the colorbar and in the time-dependent result. Afterwards, the response slowly converges towards a constant response amplitude which is found in both the p-y response and equivalent damping result. The same effect is found in the cumulative energy dissipation, where a kink is found after $\approx 40m$ of cumulative spring extension. After the kink, energy that is being dissipated approximately follows a linear distribution because the response converges towards a single peak value.

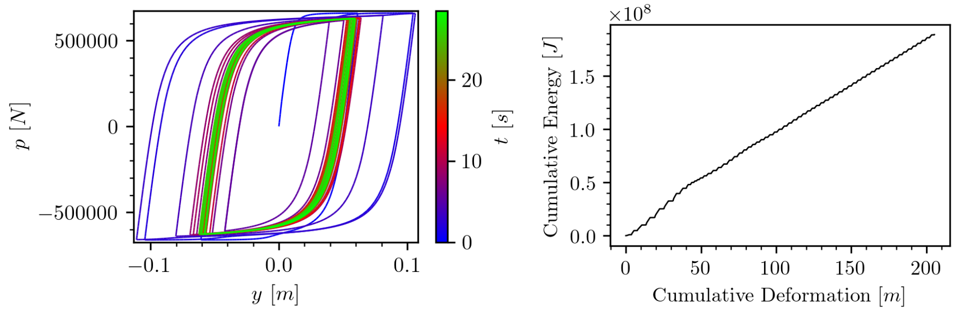

(a) P-Y response at $z = -1m$ (b) Cumulative dissipated energy at $z = -1m$

Figure 5.7: Overview of the energy dissipation for a single harmonic force at $z = -1m$

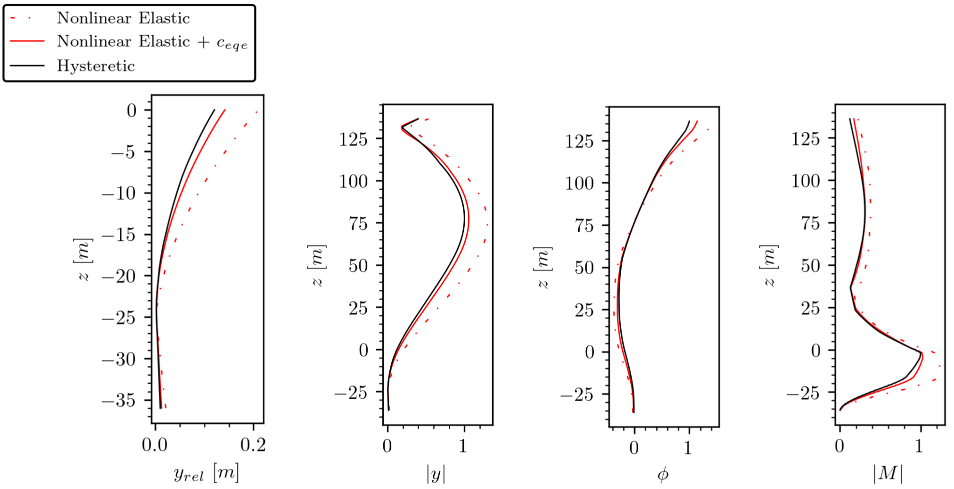

(a) Relative displacement (b) Lateral deflection (c) Rotation (d) Bending moment

Figure 5.8: Absolute maximum response of equivalently damped model to a single harmonic force

Under application of equation 4.19, a depth-dependent distribution of equivalent dashpot coefficients c_{eqe} is found. This is visualized in Figure 5.5. The dashpots are then applied in parallel with nonlinear but elastic springs which follow the same backbone curves as the initial load-path of the hysteretic springs. Very good and conservative agreement is found in the peak time-domain response to a single harmonic force. The peak time-domain results normalized with respect to the maximum observed hysteretic response of the two nonlinear models is compared in Figure 5.8. The applied load magnitude is still at a level where the maximum capacity of the clay soil layers have not yet been exceeded. No effects of soil-pile separation is observed within these layers. If this would this have been the case, effect would have been noticeable in both time varying nature of equivalent damping, p-y response, and cumulative energy dissipation. In the case of soil-pile separation, loop area (and therefore amount of damping by hysteresis) decreases. For the cumulative energy result in Figure 5.7 for instance, this implies that the kink is represented much more dominantly.

5.2.2 Seismic Response

The lateral hysteretic spring response is assessed to indicate the amount of energy dissipation of each of the individual embedded springs to seismic input. Upon application of the different imposed motions at the supports of the structure (5.1.2), the springs return different behavior as a result of the difference in frequency and amplitude characteristics of the applied motions (Figures 5.3 and 5.4). From the response of each hysteretic spring an equivalent damping c_{eqe} is found using equation 4.19 and applied in parallel with the equivalent elastic springs. Below in Figure 5.9 the force-displacement response and corresponding cumulative energy dissipation associated with the specific timeseries is summarized. Considering these results, it is consistently found that after the strong motion part has occurred (where plasticity is largest), the energy cumulative dissipation reaches a certain plateau because the response globally returns towards linear-elasticity. The magnitude and position of this plateau naturally varies per input motion.

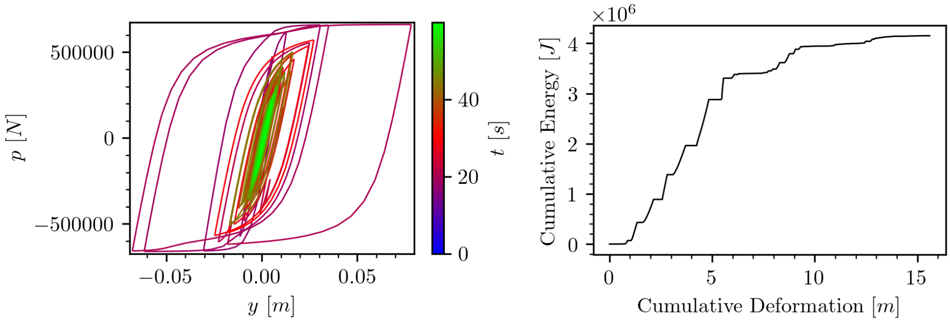

(a) P-Y response at $z = -1m$ for motion 1

(b) Cumulative dissipated energy at $z = -1m$ for motion 1

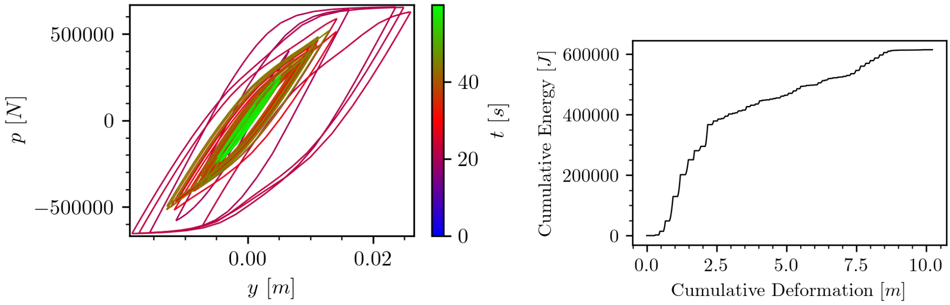

(c) P-Y response at $z = -1m$ for motion 2

(d) Cumulative dissipated energy at $z = -1m$ for motion 2

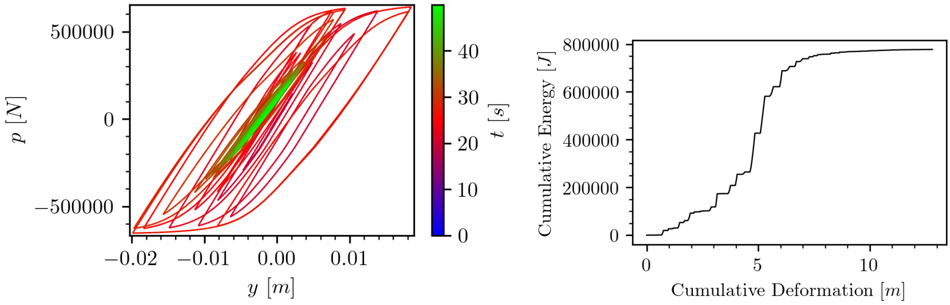

(e) P-Y response at $z = -1m$ for motion 3

(f) Cumulative dissipated energy at $z = -1m$ for motion 3

Figure 5.9: Overview of the energy dissipation for the three different motions

In Figure 5.8 the time-varying equivalent damping to the response just below mudline is visualized. In ζ versus time the observed equivalent damping is largest in the strong-motion parts of the seismic signal (when comparing with the time range indicated by colorbar in Figure 5.9). This is again not observed for c where the identified damper coefficient can differ quite substantially with the observed maximum throughout the total timeseries. Identified equivalent damping values are indicated in the figures at the timestep when relative displacement has reached its absolute maximum value. According to the computed equivalent damping response to motion 2, this does not necessarily imply that identified equivalent value ζ_{eqe} is at its peak value. When the relative displacement response to this specific motion at this specific spring is maximum, the subsequent reloading-path occurs at an earlier stage than other load-cycles. In relation towards the ultimate limit state, it is found that the single identified c_{eqe} using equation 4.19 at the timestep where relative displacement is largest can be used to reasonably represent the damping over a total timeseries. Repeating the same exercise for each individual soil spring, the total distribution of equivalent damping is found in Figure 5.9 for each of the considered motions. Apart from the magnitude of equivalent damping, the depth-dependent results show a fairly similar distribution over embedment depth. This result indicates that the distribution of energy dissipation over depth is frequency independent because of the observed deviations in frequency content of the input motions (Figure 5.3). Additionally, a secant stiffness distribution is found by the ratio of reaction force to relative displacement. This constant, identified secant spring stiffness may be used to support linear elastic analysis. To take permanent plastified displacements into account, the secant stiffness is computed for both observed minimum and observed maximum response and taken as average of both. Because of a larger load-level the identified secant stiffness to motion 1 is lowest, but the amount of identified damping is the largest relative to motions 2 and 3.

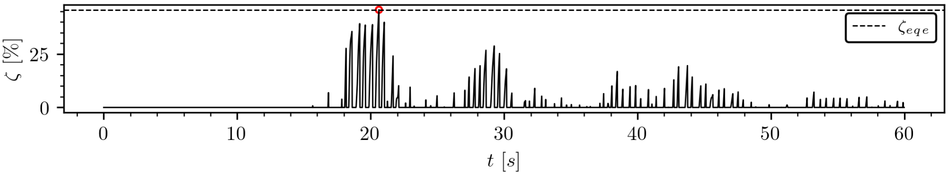

(a) Motion 1, ζ

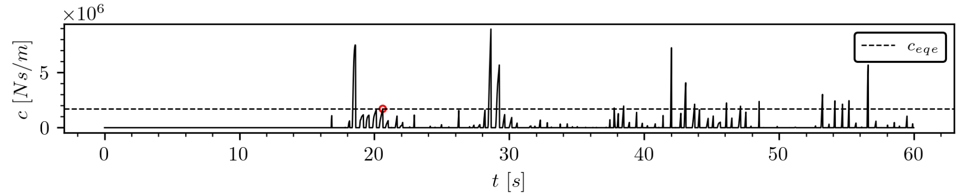

(c) Motion 1, c

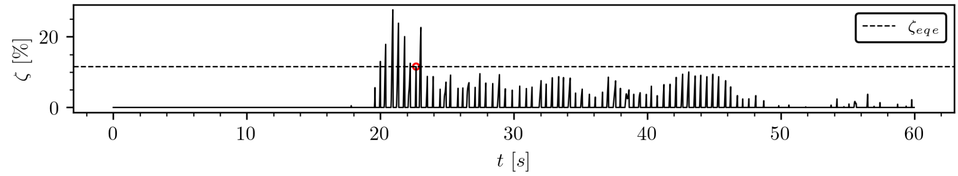

(d) Motion 2, ζ

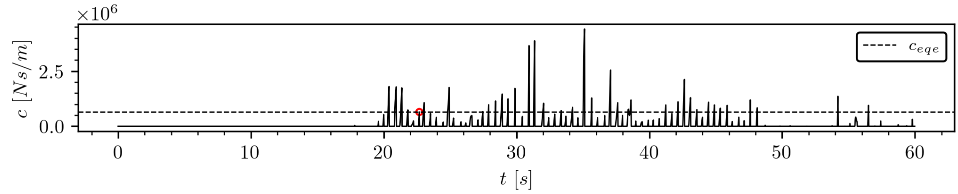

(e) Motion 2, c

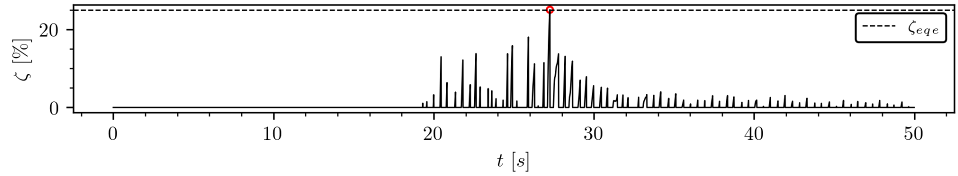

(f) Motion 3, ζ

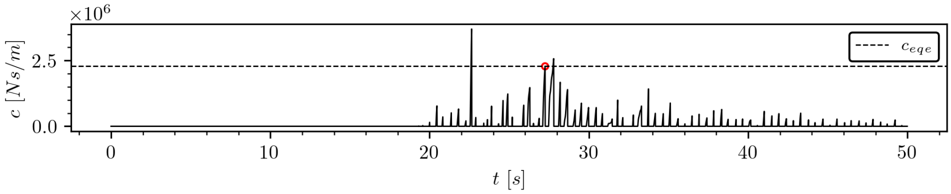

(c) Motion 3, c

Figure 5.8: Time varying equivalent damping results for motions 1, 2, and 3 at $z = -1m$

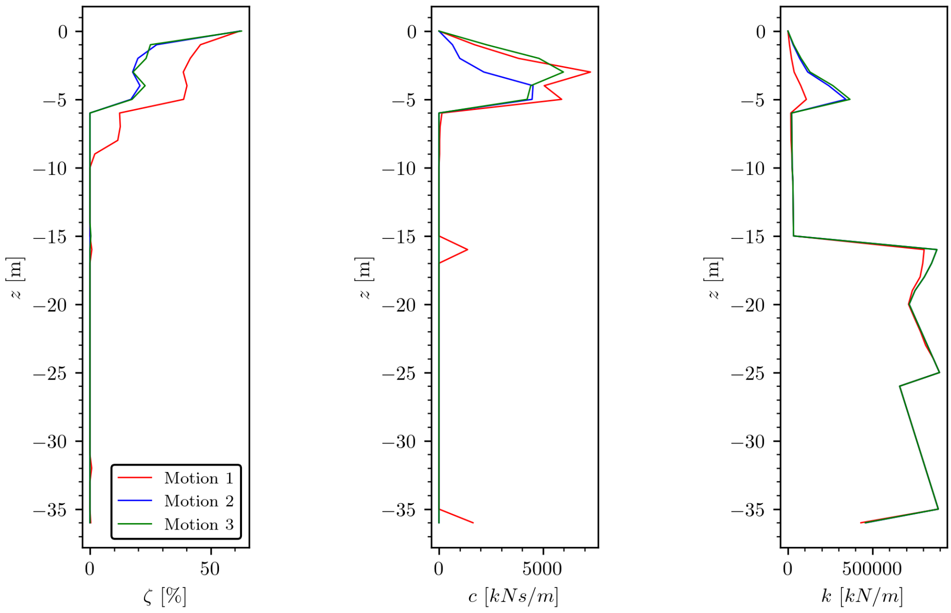

(a) ζ_{eqe} versus depth (b) c_{eqe} versus depth (c) k versus depth

Figure 5.9: Depth dependent equivalent results for motions 1, 2, and 3

5.3 Results

The response of the hysteretic and equivalently damped (both linear and nonlinear) models is analyzed and discussed. For reference purposes, non-damped (both linear and nonlinear) **but elastic** situations are considered as well. Values for the equivalent hysteretic dashpot coefficients to be applied in parallel with the soil springs along the monopile embedment depth have been derived according the procedure presented in 5.2.2 for the three considered input motions and are visualized in Figure 5.9 (b). Discussion will focus further on the results computed at mudline and at tower top.

5.3.1 Eigenproperties

Before imposing any loads, it is important to evaluate the dynamic properties of the offshore wind turbine model: perform an eigenvalue analysis. A generalized eigenvalue problem for two symmetric matrices $\mathbf{K}$ and $\mathbf{M}$ of size $n \times n$ is given by:

$$(\mathbf{K} - \boldsymbol{\lambda}\mathbf{M})\boldsymbol{\Phi} = \mathbf{0} \tag{5.1}$$

Where:

$\mathbf{K}$: is the (initial) stiffness matrix;

$\mathbf{M}$: is the mass matrix;

$\boldsymbol{\lambda}$: is the eigenvalue;

$\boldsymbol{\Phi}$: is the associated eigenvector.

The first four (lateral) bending modes of both the nonlinear and equivalent linear models are summarized in Table 5.2 and the first four (normalized) eigenvectors are visualized in Figure 5.10. The eigenproperties of the equivalent linear models differ by variation of the soil-spring stiffnesses. It is found that because of larger load level associated with motion 1, secant spring stiffness is lowest compared to the other models which results in different eigenproperties and a ”softer” modeshape. Because the load-level of applied motion 2 is lowest, observed secant stiffness is closest to the initial stiffness of the nonlinear model leading in eigenproperties close to that of the reference nonlinear model. The modeshapes for the nonlinear models have been derived using the initial stiffness matrix but in fact, the stiffness matrix changes each time increment due to the nonlinear nature of soil springs which is a simplification of true modal properties. Because the true focus of this work does not lie on evaluating the full and true modal properties of an offshore wind turbine structure, this will not be assessed any further.

	f_0	f_1	f_2	f_3	
Nonlinear	0.238	1.108	2.001	3.747	Hz
Motion 1	0.221	0.966	1.880	3.535	Hz
Motion 2	0.240	1.071	1.944	3.654	Hz
Motion 3	0.243	1.123	1.994	3.748	Hz

Table 5.2: Natural Frequency Characteristics

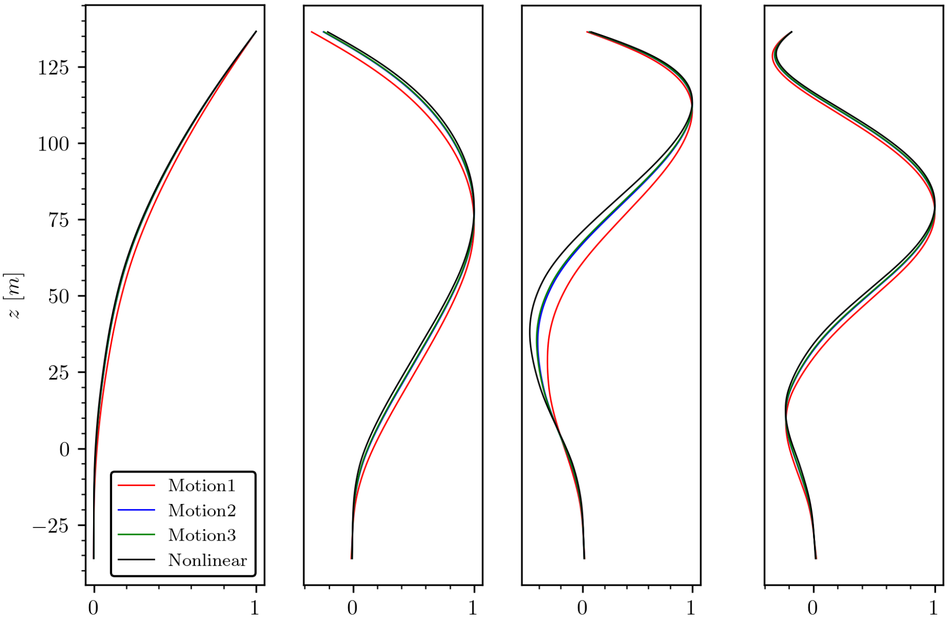

(a) Mode 1 (b) Mode 2 (c) Mode 3 (d) Mode 4

Figure 5.10: Overview of the first four normalized bending modes

5.3.2 Time-Domain Response Analysis

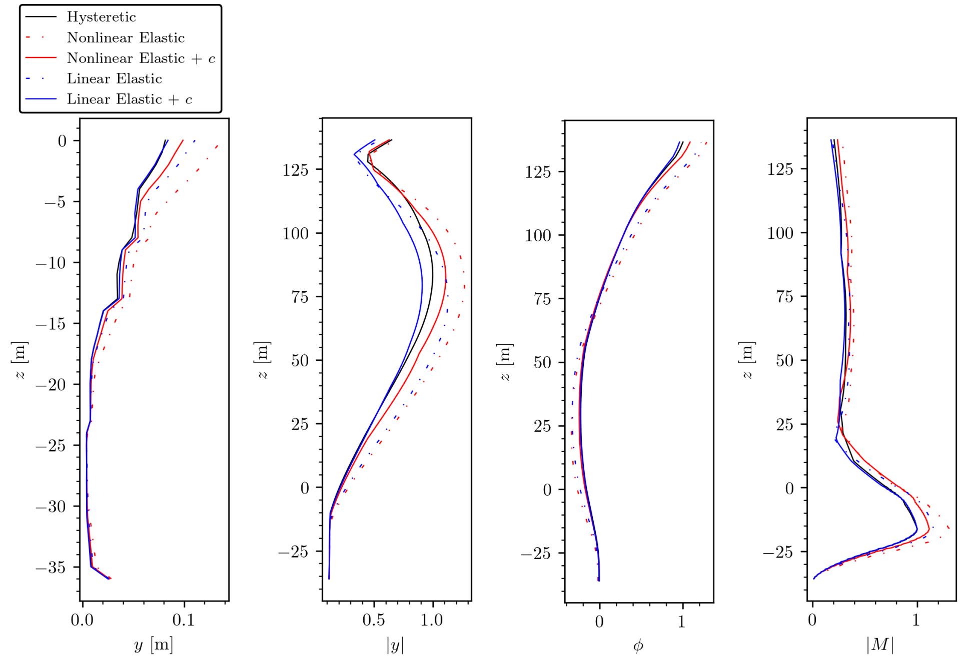

(a) Relative displacement (b) Lateral deflection (c) Rotation (d) Bending moment

Figure 5.11: Absolute maximum time-domain response to motion 1

The peak time-domain results are visualized in Figures 5.11, 5.12, and 5.13. All results have been normalized with respect to the observed peak hysteretic response of the quantity of interest. Except for relative displacements to indicate and compare the amount of plasticity present. Throughout all the three considered input motions it is found that for the equivalently damped nonlinear elastic model the relative displacements along the pile shaft and rotations along the structure total height are converging towards the hysteretic model and are consistently on the conservative side. Performance differs per input motion for lateral deflection and bending moment. Good agreement has been found for motions 1 and 3 in terms of bending moments, but motion 2 returns the same observed peak bending moment as the non-damped reference case. Good and conservative agreement is found for motions 1 and 2 in terms of peak lateral deflection, but not for motion 3 where closer towards tower top, the peak lateral deflection gets substantially underestimated. Because of linearization a perfect match for the equivalent linear model is not to be expected. Good agreement is found for motions 1 and 2 in terms of bending moment response. The lateral deflection is somewhat underestimated. For motion 3 the bending moments and lateral deflection are both underestimated using a linear elastic secant stiffness model.

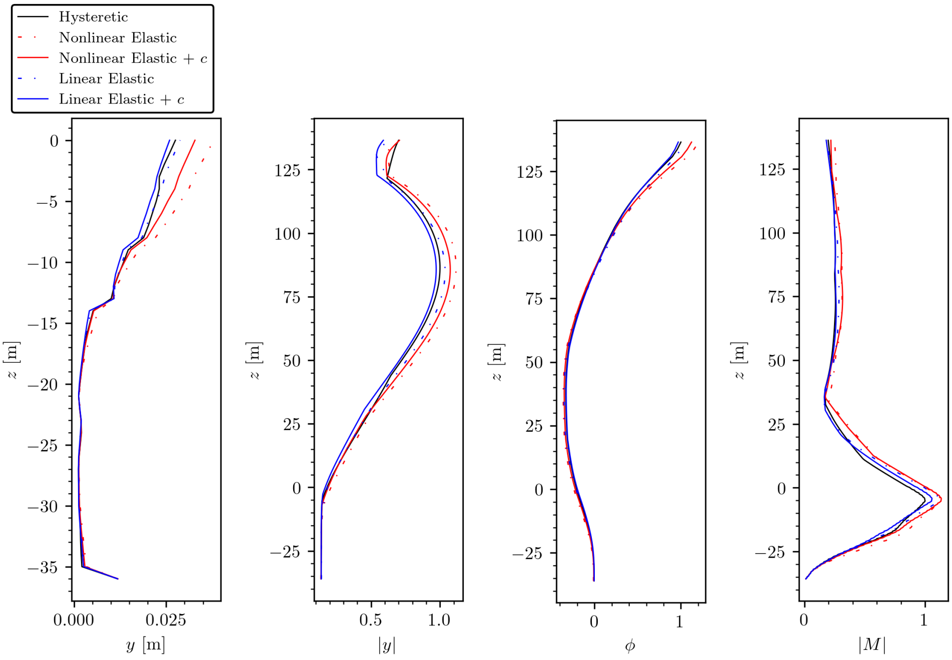

(a) Relative displacement (b) Lateral deflection (c) Rotation (d) Bending moment

Figure 5.12: Absolute maximum time-domain response to motion 2

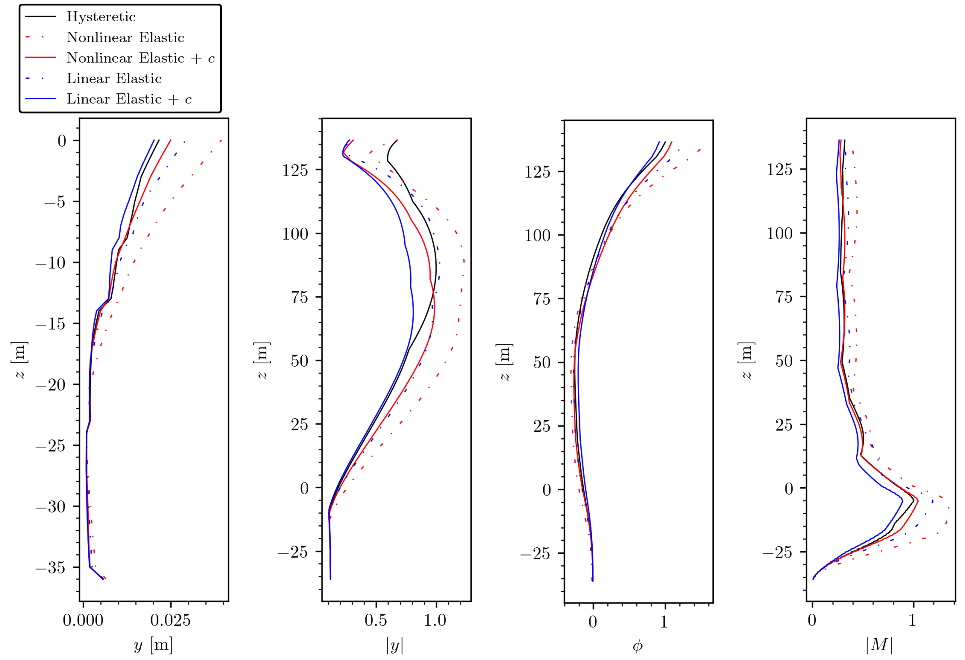

(a) Relative displacement (b) Lateral deflection (c) Rotation (d) Bending moment

Figure 5.13: Absolute maximum time-domain response to motion 3

Additional time-domain results are found in Appendix A where the (normalized) time history associated with bending moment and deflection at mudline and tower top is presented. Here it is found that looking beyond the observed peak values, all load-cycles get reduced to an acceptable level and show similar response to the reference hysteretic response. These results are discussed more extensively in 5.3.4.

5.3.3 Frequency Content Response Analysis

Different seismic signals vary in both amplitude and frequency content. Result is that different response characteristics can be encountered. Next to that, linearization has effects on the dynamic response and the response of the hysteretic model is subjected to permanent displacements which can not be simulated using our equivalent elastic models. A more common approach to assess the structural response is generally done in the frequency domain by investigating the dynamic amplification. The spectral ratio of bending moments and lateral deflections at mudline and tower top is visualized. Here, the (Fourier transformed) output quantity is normalized with the input motion applied at bedrock and normalized by the peak observed hysteretic response. Such a ratio is generally referred to as a transfer function to relate input with output. A similar procedure was earlier presented in Figure 2.4 (a). The total resulting magnification spread throughout the three different considered input motions is summarized in Figures 5.14 and 5.15 on both logarithmic and linear scale. The shaded areas indicate the range between observed minimum and maximum amplification for all three motions and the minimum and maximum non-damped reference cases are characterized by the dash-dotted lines. In Appendix A the (non-normalized with forcing input) amplification of the deflection and bending moment at mudline and at tower top on linear scale is presented separately for all input motions to enhance our understanding.

The bending moment response at mudline and tower top is mostly amplified around the second resonance frequency of the structure to all input seeds. However, at tower top amplification is dominated close to the third resonance frequency. Amplification is significant for the non-damped models around this frequency compared to the damped models. In application of equivalent dashpots in parallel with soil-pile interaction springs, bending mode amplification around both the second and third resonance frequency of the structure are effectively reduced. Because of low-frequency noise, normalization is taken from the peak observed hysteretic amplification in this second resonance frequency at mudline. Ignoring the presence of low frequency noise in the deflection spectral ratio, tower top deflection is dominated by the first resonance frequency of the structure. This result can be substantiated by looking at the eigenshape associated with this first resonance frequency: mode 1 in Figure 5.10. None of the equivalent elastic models seem to be able to capture the magnitude of peak hysteretic amplification at tower top. At mudline, the lateral deflection gets mainly amplified by the second resonance frequency which is equivalently damped to an acceptable level. Including the results from Appendix A, it is found that it is not possible to match amplification in the first mode with the equivalent elastic models. Except for motion 2 where applied load-level is low.

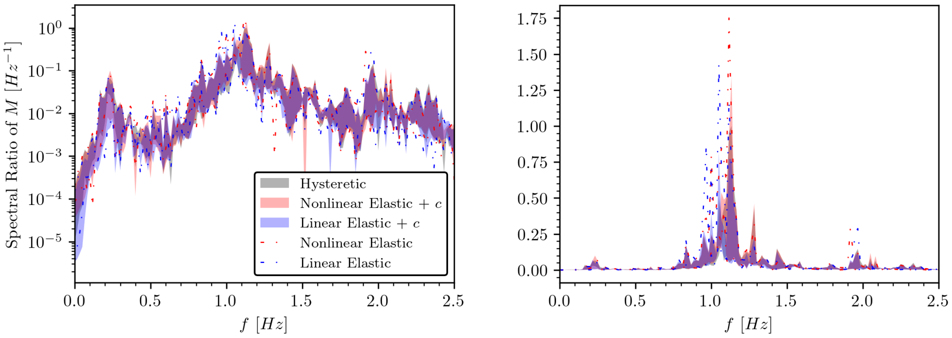

(a) Mudline bending moment, logarithmic scale (b) Mudline bending moment, linear scale

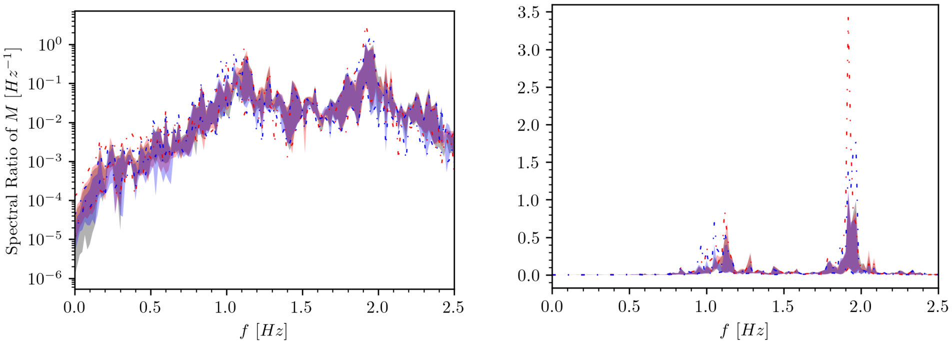

(c) Tower top bending moment, logarithmic scale (d) Tower top bending moment, linear scale

Figure 5.14: Spectral bending moment ratio

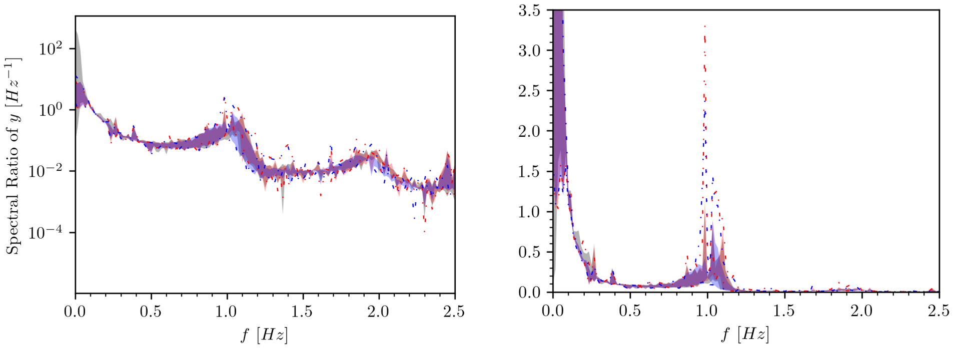

(a) Mudline deflection, logarithmic scale

(b) Mudline deflection, linear scale

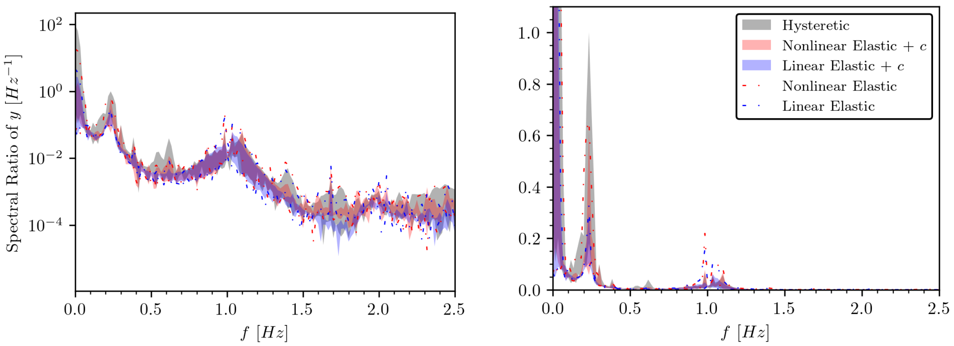

(c) Tower top deflection, logarithmic scale

(d) Tower top deflection, linear scale

Figure 5.15: Spectral deflection ratio

5.3.4 Discussion

Throughout this chapter, it is discussed that the dynamic behavior of the offshore wind turbine is complex. Assessing the dominance of frequency content is a critical design aspect, but assessing dynamic behavior of a structure against the stochastic nature of seismic input is an ambiguous process to begin with. Opposed to the nonlinear hysteretic model, the equivalent elastic models impose different dynamic characteristics because of a constant stiffness (linear elastic) and zero stiffness upon unloading (nonlinear elastic). The following observations made in this chapter are discussed:

It is found that the influence of higher bending modes are of utmost importance. In general, the structural response is mostly characterized by its second bending mode under the three considered seismic seeds. However, the third mode governs the bending moment response at tower top and the first mode governs the lateral deflection at tower top.

The application of equivalent dashpots in parallel with elastic springs seems to most effectively damp amplification around higher resonance frequencies of the structure. Looking at the normalized modeshapes of the structure in Figure 5.10, the soil-springs extend the most for higher bending modes and only a little for mode 1. Because of this, it is found to be difficult to match the amplification at tower top lateral deflection. This observation seems consistent throughout the three different input motions.

The time domain results have shown that it is complicated to capture the peak bending moments and peak deflection along the total structure. The dynamic amplification supporting the associated time histories has shown insight to why the match is so extremely disproportional at tower top deflection. The lateral deflection at tower top is characterized mostly by the first resonance frequency, and the elastic equivalently damped models have shown that converging to the dynamic amplification associated with this first resonance frequency is not possible. Only amplification of higher bending modes are effectively reduced to that of the hysteretic response. The response to motion 2 provides good agreement in terms of lateral deflection amplification at tower top however, permanent plastic displacements are negligible.

Permanent displacements have noticeable effect on the performance of the equivalently damped elastic models because this typical characteristic of hysteresis is not captured during elasticity. Large permanent displacements relative to the observed peak value are found in the response to motion 1 causing a large mismatch in peak tower top deflection: Figures A.5 and A.6.

During linear analysis, the complete stiffness matrix is simplified to act as a constant: a strict simplification that already alters the dynamic response. Overall, this has its effect on the performance compared to that of the nonlinear elastic model, where response results are underestimated in combination with equivalent damping. Motion 1 with larger plasticity compared to the response to the other two motions provides good agreement in the peak values using equivalently damped linear elastic springs. Permanent displacements are present but are relatively small compared to the peak values.

On the topic of the timeseries' results in Appendix A, it is observed that the equivalently damped models converge to the hysteretic response for all load-cycles at both mudline and tower top. This observation is a sign that looking beyond the ultimate limit state, an equivalently damped model yields potential in the fatigue limit state (FLS). To substantiate this, (normalized) cumulative response at mudline is visualized in Figure 5.16. Clearly, the equivalently damped models provide better agreement than the non-damped results and almost exactly follow the hysteretic response shape. The cumulative result computed with linearized stiffness does overestimate the amount of damping related to the bending moment response, however.

The discretization steps applied in this study to assess the offshore wind turbine structural response against the earthquake signals are far from reality. In real-time dynamic behavior bending modes would be highly influenced by the operational condition (either idling or fully operational), coupling of lateral and vertical modes, blade modes, and coupling of different lateral directions. Especially bending modes of the blades seem to have significant influence on the total response, but mostly at tower top [35], leaving the interpretation of the results found throughout this work and their representation of reality highly open for debate. This discrepency could lead to unrealistic inertial force distribution of the structure. The blades could even be the driving design factor [35], highlighting the actual importance of including such additional structural properties in the discretization. As stated by [29], the soil hysteretic damping contribution may vary over operational conditions and loading direction. Regarding the statement above, in realistic situations one must consider each of the loading-directions and operational conditions to conclude the peak critical loads.

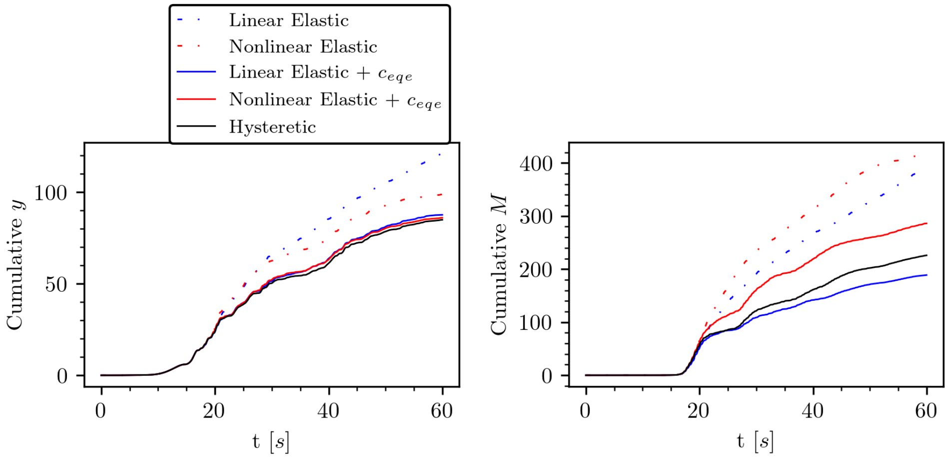

(a) Mudline deflection, motion 1 (b) Mudline bending moment, motion 1

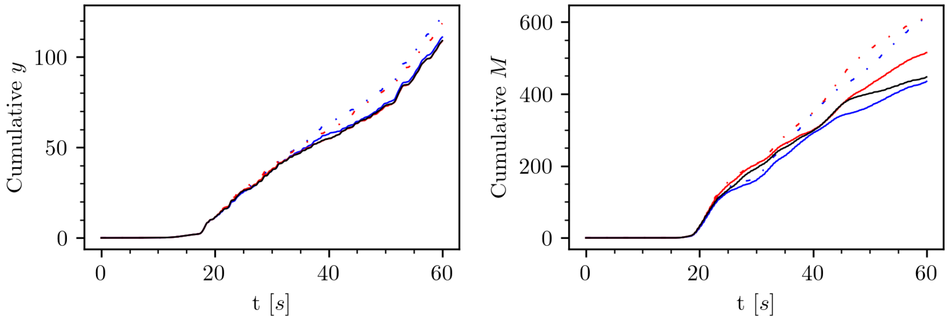

(c) Mudline deflection, motion 2 (d) Mudline bending moment, motion 2

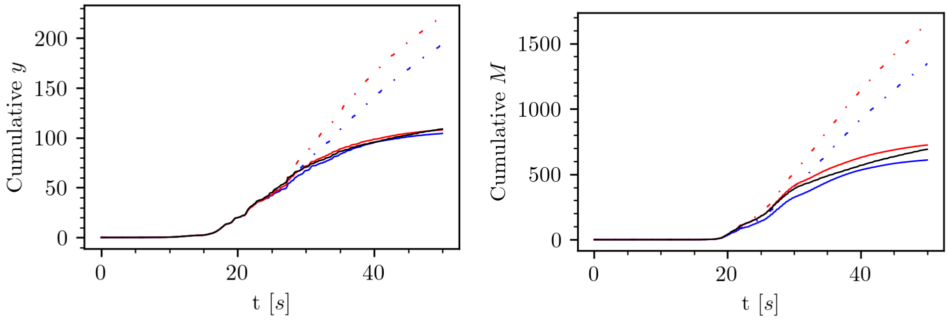

(e) Mudline deflection, motion 3 (f) Mudline bending moment, motion 3

Figure 5.16: Cumulative response at mudline

5.3.5 Relation to Recommended Practice

Local Approach

Results in this chapter were limited to the application of back-calculated dashpot coefficients c_{eqe}. However, in relation to practice where the amount of damping to be applied is generally expressed in % of critical damping [12], the time-domain equivalently-damped linear elastic models to motions 1, 2, and 3 under application of back-calculated ζ_{eqe} (Figures 5.8 (a), (c), (e)) are explored in Appendix B. The local dashpot coefficients are found by adopting stiffness proportional damping, with stiffness equal to the linearized soil-spring stiffness and frequency equal to the dominant frequency of the applied signal at bedrock. Results in Figure 5.17 show an approach closely related to that as described by recommended practice is capable of providing sensible results in terms of peak bending moment response. For a more extensive description and comparison of c_{eqe} with ζ_{eqe} is referred to Appendix B.

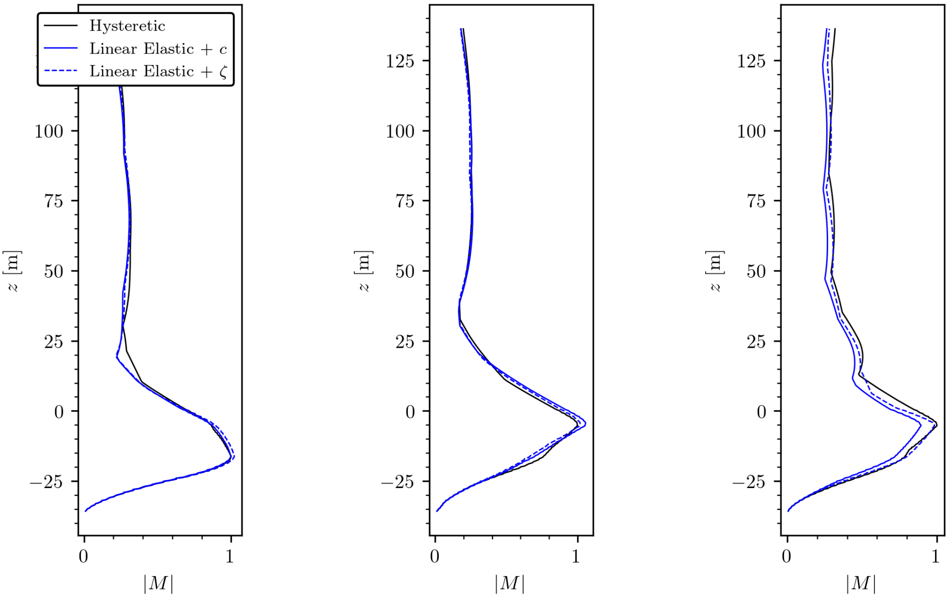

(a) Motion 1 (b) Motion 2 (c) Motion 3

Figure 5.17: Peak bending moment response

Global Approach

Additionally, recommended practice [12] prescribes the application of the soil material damping contribution on a global scale where logarithmic decrement damping is used. An amount of critical damping ζ is fit onto the general solution of free-vibration decay presented in equation 2.5. Tsouvalas et al. [47] claims that in earthquake engineering practice, the first mode is always one of the two modes chosen and the latter one being the second mode or a higher order one. The time-domain damping identification strategy is applied to indicate the damping ratio to the first and second bending mode in a procedure fully described in Appendix C. A displacement-dependent modal damping is found for the first two bending modes of the PySimple1 spring supported structure visualized in Figure 5.18.

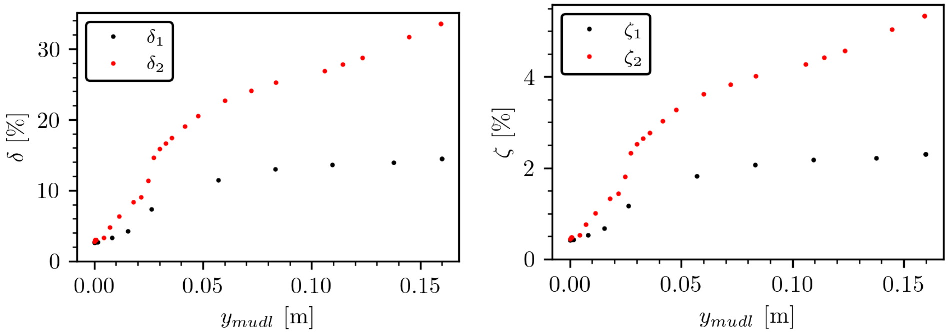

(a) δ (b) ζ

Figure 5.18: PySimple1 logarithmic decrement to bending mode 1 & 2

Using Rayleigh damping, a damping matrix as proportion to the mass and stiffness of the structure is then identified by the two vibration modes: equation 5.2. $\zeta(\omega)$ needs always to be considered to guarantee that damping is in fact positive and reasonable. Following observed mudline displacements at motion 1 (Figure 5.11), values for ζ_1 and ζ_2 are found using Figure 5.18 (b) and applied in equation 5.2. The modal damping ratio is visualized over frequency in Figure 5.19 using equation 5.5. While the amount of damping follows ζ_1 and ζ_2, higher bending modes than the second are disproportionally damped in this specific case. One must therefore carefully assess which modes to consider which are usually the bending modes expected to participate the most.

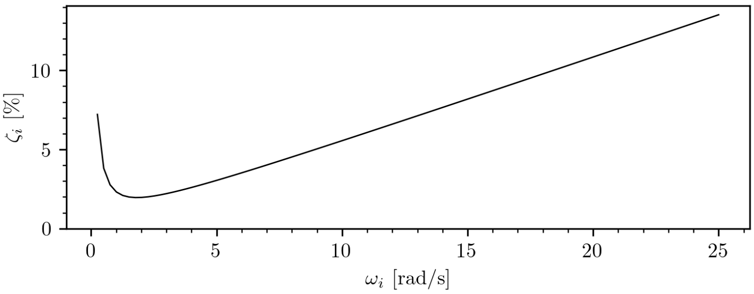

Figure 5.19: Identified Rayleigh damping to mode 1 & 2

$$\mathbf{C} = a_0\mathbf{M} + b_0\mathbf{K} \tag{5.2}$$

$$a_0 = \frac{2\omega_1\omega_2(\zeta_1\omega_2 - \zeta_2\omega_1)}{\omega_2^2 - \omega_1^2} \tag{5.3}$$

$$b_0 = \frac{2(\zeta_2\omega_2 - \zeta_1\omega_1)}{\omega_2^2 - \omega_1^2} \tag{5.4}$$

$$\zeta_i = \frac{a_0}{2\omega_i} + \frac{b_0\omega_i}{2} \tag{5.5}$$

Chapter 6

Conclusions and Recommendations

6.1 Conclusions

Soil-structure interaction has shown to be a very complex process. Regarding the associated complexities, reasonable accuracy is achievable using a full nonlinear three-dimensional Finite Element model. Such modelling is not only computationally demanding, but also lacks convenience due to many modelling considerations. On that note, it is common practice to simplify the soil continuum into one-dimensional springs connected to the foundation. These foundation springs can vary in type: from linear elastic to nonlinear hysteretic. Soils exhibit hysteresis during seismic loading. Such hysteresis provides damping: the dissipation of energy. This damping has therefore positive contribution to the dynamic response, as it limits the response amplitude. The inclusion of nonlinear hysteresis implies computational demand: each of the nonlinear unloading-reloading cycles has to be simulated separately. To do so, the nonlinear spring stiffness must be updated each timestep. In addition, general consensus is yet to be reached for sets of unloading-reloading rules in the simulation accurate seismic soil-monopile interaction. Practice therefore prefers the application of soil damping in an equivalent way, either local or global. For this reason, the main objective of this research is:

How to establish an engineering method that assesses soil material damping during seismic motions in the large-strain regime and integrate this into an equivalently damped dynamic offshore wind turbine model?

6.1.1 Review of the Research Questions

- Industry typically represents the soil-monopile interaction mechanism by one-dimensional depth-dependent soil reaction curves. When the structure is subjected to a seismic event, the soil-structure interaction mechanism is characterized by substantially more components rather than merely a description of static lateral resistance. Realistically, hysteresis must be accounted for under the presence of dynamic loading. Measurement and numerical data related to offshore wind turbines indicates the importance of additional rate effects, ratcheting, gapping, stiffness degradation, and strength deterioration [4, 7, 9, 30]. Soil material damping is typically characterized by the area enclosed by these unloading-reloading paths. For an accurate representation of soil material damping, accurate unloading-reloading rules are therefore of paramount importance. However, general consensus is yet to be reached for correct unloading-reloading rules and thus an accurate representation of soil material damping.

- A simplified contribution of soil material damping is applied either in local or global fashion. To account for soil material damping on a global level, logarithmic decrement damping is typically used based on experimental and numerical measurement data. To account for soil material damping on a local level, equivalent damping curves (lateral deflection versus % of critical damping, ζ) are constructed under prescription of [12] and applied in parallel with the linearized soil stiffness. These curves are typically constructed using Masing rules which provide an unrealistically large amount of damping under large soil-strains compared to measurement data (60% versus 20-30%). These curves may therefore be effectively reduced under provision of [36, 37].

- To gain insight in the soil material damping mechanism during seismic motions, the amount of energy that is being dissipated is captured on a local scale. The equation that describes the amount of equivalent damping on a local level by recommended practice (equation 2.9) holds little reliability when applied to stochastic, non-symmetrical load-paths. To incorporate the effects of permanent hysteretic displacements in finding the local energy dissipation, a method is employed that assesses each loading-cycle separately. The amount of equivalent damping is then calculated based on the amount of energy dissipation by an equivalent viscous damper on single-degree of freedom scale.

- When omitting hysteresis and the soil-structure interaction mechanism is modelled in an equivalent elastic procedure, the offshore wind turbine seismic response imposes generally different dynamic characteristics. In the hysteretic PySimple1 spring element adopted in this study (initial) stiffness is maintained upon unloading-reloading. During nonlinear but elastic modelling, the stiffness at this instance is zero. When adopting equivalent linear elastic springs, the stiffness is constant. Therefore, conclusions on the explored methods are presented hereafter in 6.1.3.

6.1.2 Conclusions on the Method

- An equivalent elastic strategy is not able to simulate the effect of permanent displacement which is a typical effect of hysteresis. Therefore, it is not possible to perfectly match time-domain response in the presence of relatively large (compared to the observed peak value) permanent displacements. However, results on a single-degree of freedom scale (4.3.3 and 4.4) show that frequency-domain amplification is accurately captured.

- Based on the assumptions related in derivation of the ”classical” equation of ζ_{eqe}: equation 2.9, it does not always hold in combination with arbitrary elastic systems and arbitrary forcing input. When the forcing frequency is larger than the natural frequency of the system, the amount of damping gets overestimated and vice-versa. In combination with an elastic but nonlinear system, the equation underestimates the recoverable strain energy when taken as that of an equivalent linear spring which subsequently overestimates the damping.

- The application of a single dashpot coefficient c_{eqe}: equation 4.13, derived by setting the energy dissipation of hysteresis equal to that of a viscous damper, has proven to provide a good and conservative match of steady-state displacement response under a single harmonic force for both nonlinear and linear equivalently damped elastic models compared with the employed hysteretic spring element (PySimple1) on a single-degree of freedom scale. This is verified for both hard-coded sets of sand and clay. The latter is subjected to pinching, physically representing soil-pile separation (gapping) hence verifying that the adopted method is not limited to Masing type hysteresis only.

- The employed method approximates the amount of equivalent soil hysteretic damping on local spring level in a multi-degree of freedom offshore wind turbine model where the response of the nodes is coupled. It is therefore not possible to match the amplification of all bending modes at the same time with a local equivalent soil damping strategy. Frequency-domain results (Figures 5.14, 5.15, and A.7 - A.9) show that both equivalently damped elastic models (linear and nonlinear) effectively damp the amplification in higher bending modes. More specifically, amplification around the second and third resonance frequency. Amplification around the first resonance frequency is not successfully captured using equivalent elastic models and therefore, tower top deflection is not accurately approximated. The mismatch is larger when permanent plastic displacements are substantial, mostly observed in the response to motion 3 where tower top deflection is significantly underestimated for both elastic models.

6.1.3 Conclusions on the Equivalently Damped OWT

- Good and conservative agreement is found using equivalent nonlinear elastic modelling for observed time-domain peak deflection and bending moment along the total structure when subjected to single harmonic loading. However, during such load-case, permanent displacements are typically negligible and hysteretic loops remain fairly symmetric (Figure 5.7 (a)).

- The time-domain response to the different seismic motions considered in this research shows that equivalent nonlinear elastic soil springs with the inclusion of local equivalent viscous dashpots (constant coefficients obtained using equation 4.19) consistently provide effective and conservative results in terms of peak time-domain relative displacement/spring extension along the embedded monopile shaft. Over the course of the three different motions the peak time-domain bending moment response and lateral deflection is therefore captured with reasonable agreement. Equivalent linear elastic springs in combination with local equivalent viscous dashpots consistently underestimates the peak time-domain relative displacement. A strategy with equivalent linear elastic springs therefore mostly underestimates the peak time-domain response.

- As mentioned in 6.1.2, permanent displacements are not simulated using equivalent elastic strategies. Therefore, frequency-domain response provides better insight. Despite not able to accurately capture the peak time-domain response, bending moment and lateral deflection amplification at mudline and bending moment amplification at tower top are reasonably captured for both linear elastic and nonlinear elastic models over the course of the three input motions. An equivalent local damping strategy effectively damps amplification around the second and third resonance frequency of the structure. Next to a shift of resonance frequency in the linearized model, amplification is more effectively damped in the linear model. Linearization already reduces the peak response in both time- and frequency-domain. The adopted local strategy is not able to converge towards hysteretic tower top deflection which amplification is significantly dominated by the first resonance frequency.

- According the cumulative time-domain response computed at mudline, equivalent elastic modelling shows potential in the fatigue limit state. A constant identified equivalent damper coefficient per soil spring is capable of closely converging to the total hysteretic cumulative deflection at mudline for both equivalent elastic nonlinear and linear elastic models. Performance differs for both elastic models in the cumulative mudline bending moment response where the response gets underestimated using linear elastic springs in parallel with viscous dashpots.

- Both equivalent elastic strategies in combination with equivalent hysteretic damping provide sensible results when compared to a reference hysteretic supported model subjected to seismic excitations. In both strategies, the dynamics of the structure are mostly characterized by the second and third bending mode which get effectively damped to a comparable level between the two elastic models. Given that nonlinear time-domain analyses are computationally expensive and the response is comparable between both equivalent models, an equivalently damped strategy shows great potential to be used in support of linearized frequency-domain analyses. Results in this research show and conclude that given the assumptions made, a locally equivalently damped elastic strategy is capable of accurately capturing the damping originating from the hysteretic soil-pile interaction mechanism during seismic excitations in the second and third bending mode.

- Given the computed time-domain and frequency-domain response, a local equivalent damping strategy is capable of reasonably capture the total foundation deflection and bending moment response, typically characterized by higher bending modes.

- The local approach is not limited to the application of c_{eqe} based on the true hysteretic velocity response, equation 4.19. Local dashpot coefficients derived using equivalent stiffness proportional damping (equation B.1) in parallel with linear elastic springs with % of critical damping derived according equation 4.18 show reasonable agreement in time-domain and frequency-domain response. Hence, it is verified that the application of equivalent linear analysis in support of a set of depth-dependent local modulus reduction curves and equivalent damping curves, a solution strategy as prescribed by recommended practice [12], can be an effective solution strategy.

6.2 Recommendations

The topic of equivalent (hysteretic) soil damping is full of uncertainties because of the complexity regarding the soil-structure interaction mechanism. This research only contributes partly in increasing our understanding in soil-monopile interaction. Recommendations for further work and topics that require further investigation are classified in two parts: a review of the ways to improve the method addressed in this thesis and points that are not considered in this work but could be important to look into. Recommendations regarding the method adopted in this study are:

- The throughout this thesis developed and adopted algorithm thrives on the core assumption that each of the subsequent unloading-reloading cycles are inverted replicas of each other. An assumption which is consistent with Masing principle, described in 2.1.1. Furthermore, the algorithm assumes that the integral of velocity squared is equal for both the true cycle and the hypothetical cycle so that the numerator and denominator are scaled by the same factor: information of each loading cycle is therefore obtained separately. For further research it is recommended to include information of the subsequent loading cycle in derivation of c_{eqe}. To do so, focus on finding an innovative method that closes an hypothetical loop based on related unloading-reloading rules.

- By using % of critical: ζ_{eqe} instead of the application of c_{eqe}, to keep close relation towards recommended practice [12], it is recommended for further research to reduce the amount of critical damping towards realistic values of soil hysteretic damping as found in measurement data using reduction factors prescribed by [37, 36].

- The algorithm in its current form identifies the amount of equivalent damping at the timestep where the relative displacement / spring extension is largest. This does not necessarily imply that the related load-path provides the largest amount of damping as seen in Figure 5.8 (d). For further research it is recommended to stick to a formulation in % of critical damping as this is widely adopted throughout research and to compute the amount of ζ_{eqe} from an hysteretic timeseries it is recommended to use the timestep where the observed critical damping ζ is largest.

Points that are not considered in this research and are potentially interesting further research possibilities are:

- Application of dashpot coefficients in this study are 'tuned' on local level: using local hysteretic spring response. Therefore, matching modal amplification (which is global) is not possible for every mode of excitation simultaneously. Matching of the damping on a global level is normally done in the modal domain: per mode of vibration. The turbine manufacturing industry is no exception to this where logarithmic decrement damping is frequently used. To extend gained knowledge in this research, a next research step should be made to translate such equivalent hysteretic damping per mode of vibration. In 5.3.5 and Appendix C a first attempt is made to find logarithmic-decrement damping for the first two bending modes. Versteijlen et al. [50] has shown that damping measurement in the frequency-domain by adopting the Q-factor (quality factor) method shows significant potential. It is a rather fast and accurate technique which allows identification of damping of multiple frequencies in a signal, as opposed to the time-domain logarithmic-decrement method.

- OpenSees is open source which makes it possible to alter the material object and its constitutive behaviour. Following the critical review about the PySimple1 material object (after Boulanger et al. [5]) used in this study, which relies on hard-coded parameters, it is recommended for further practice to rewrite the source code and to specify more accurate (for instance calibrated against 3D FE or following measurement data) backbone p-y curves and innovative unloading-reloading rules to strive for accurate values of soil damping in relation towards measurement data.

- It is recommended for further research to validate if the current adopted method holds for different soil-profiles, input motions, structural characteristics, and unloading-reloading rules in a similar procedure as presented in this study to act as a stepping stone towards clear and detailed guidelines in the application of equivalent soil hysteretic damping.

- In addition to the simulation of realistic soil-pile interaction and structural response: a logical step to take for further research would be the exploration of pore-pressure effects on the soil hysteretic damping mechanism. Previous research agrees that these effects are of utmost importance regarding seismic soil-pile interaction [53]. Additionally, it is recommended to include the dynamic effects of the rotor nacelle assembly and blades to explore the effects of operational state on the hysteretic soil damping mechanism and contribution which may vary [29].

- Lastly, the algorithm has proven its worth in identifying the amount of energy that is being dissipated in the soil-monopile interaction mechanism. A potential very interesting research possibility lies in the identification of soil-structure interaction components for offshore wind turbine structures subjected to seismic excitations. An interesting step for further research would therefore be to firstly, identify if the algorithm is capable to be applied directly in field measurement data and secondly, used to identify the amount of equivalent viscous damping present in the soil-monopile interaction mechanism directly from this measurement data.

Appendix A

Additional Results

A.1 Additional Time-Domain Results

Additional time-domain time-history results are presented in Figures A.1, A.2, A.3, A.4, A.5, A.6 to support the peak time-domain results along the total structure height in 5.3.2. Despite not always being able to converge towards the peak response (of interest when conducting analyses in the ultimate limit state), overall good agreement is found for the equivalently damped elastic models throughout the total observed timeseries. All individual load-cycles are reduced to a level close to that of the hysteretic response. Except for the lateral deflections at tower top where the response to motion 1 and 3 either gets significantly amplified (motion 1), or damped (motion 3). This result is also visible in the frequency-domain results presented in A.2. Because load-level from motion 2 is relatively low, permanent plastified displacements remain low and lateral deflection at tower top is captured to reasonable accuracy. It is clearly visible that the response to motion 3 provides plastified permanent displacements providing the mismatches in Figure 5.13.

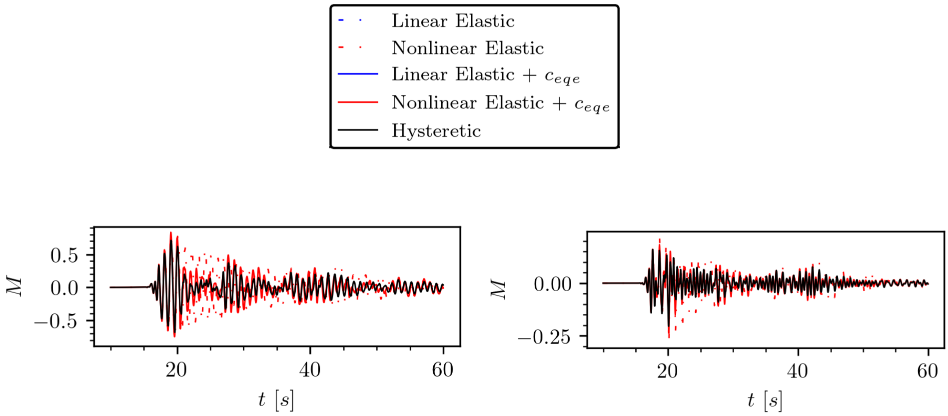

(a) Bending moment at mudline

(b) Bending moment at tower top

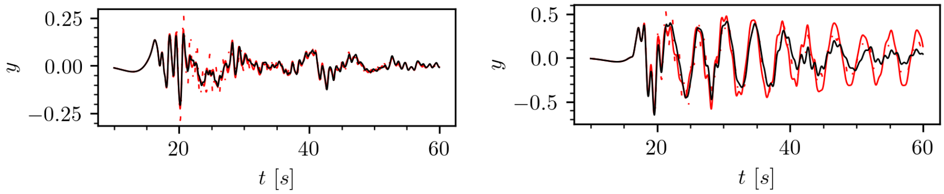

(c) Lateral deflection at mudline

(d) Lateral deflection at tower top

Figure A.1: Equivalently damped nonlinear elastic model time-history to motion 1

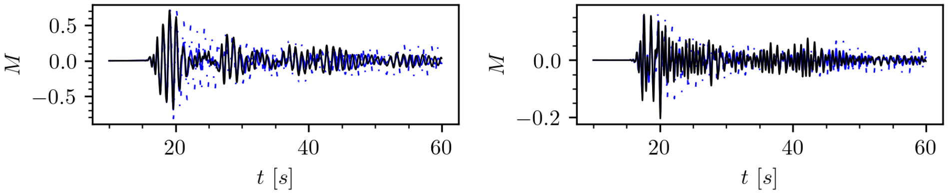

(a) Bending moment at mudline

(b) Bending moment at tower top

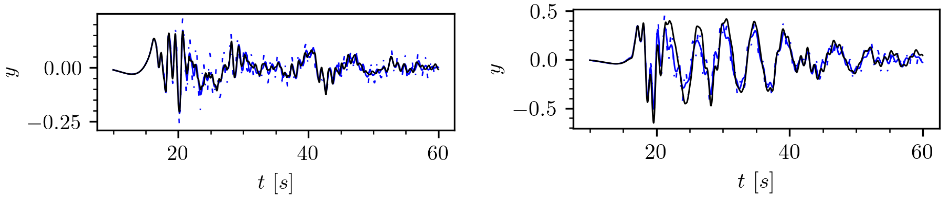

(c) Lateral deflection at mudline

(d) Lateral deflection at tower top

Figure A.2: Equivalently damped linear elastic model time-history to motion 1

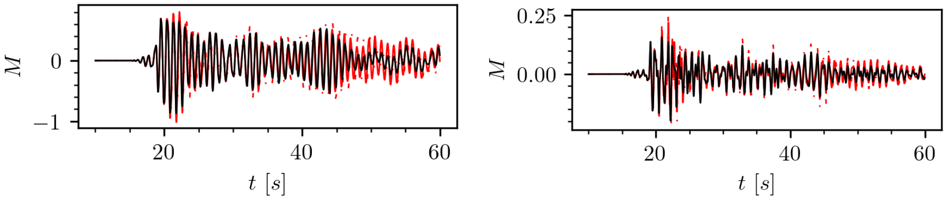

(a) Bending moment at mudline (b) Bending moment at tower top

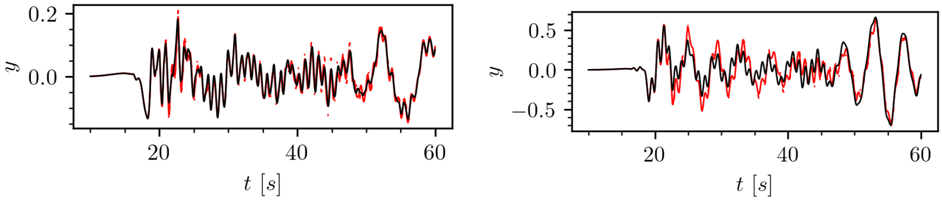

(c) Lateral deflection at mudline (d) Lateral deflection at tower top

Figure A.3: Equivalently damped nonlinear elastic model time-history to motion 2

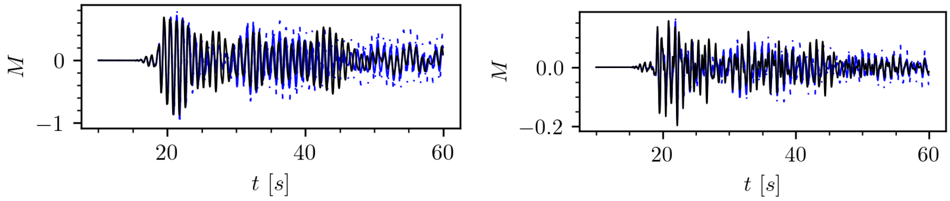

(a) Bending moment at mudline

(b) Bending moment at tower top

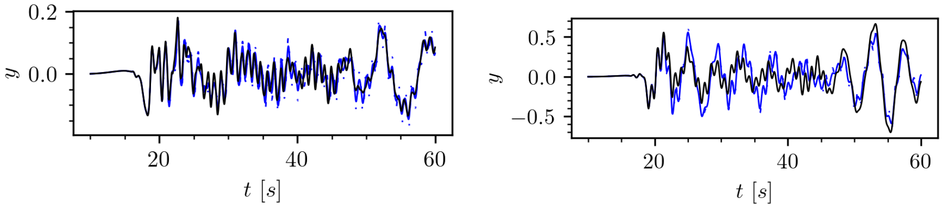

(c) Lateral deflection at mudline

(d) Lateral deflection at tower top

Figure A.4: Equivalently damped linear elastic model time-history to motion 2

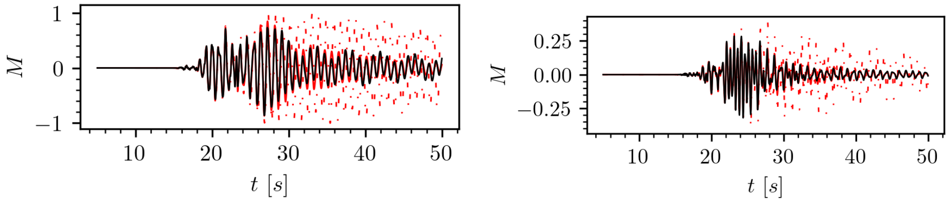

(a) Bending moment at mudline

(b) Bending moment at tower top

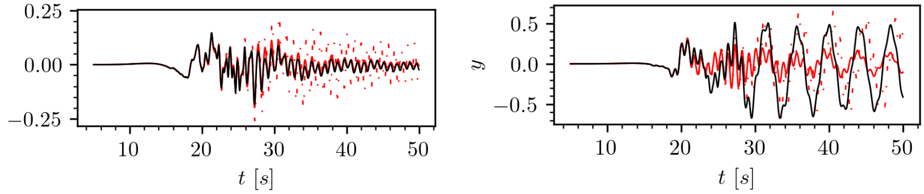

(c) Lateral deflection at mudline

(d) Lateral deflection at tower top

Figure A.5: Equivalently damped nonlinear elastic model time-history to motion 3

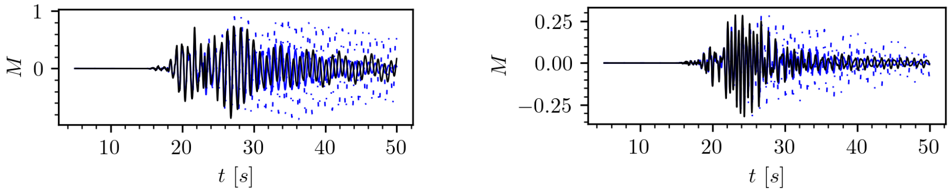

(a) Bending moment at mudline

(b) Bending moment at tower top

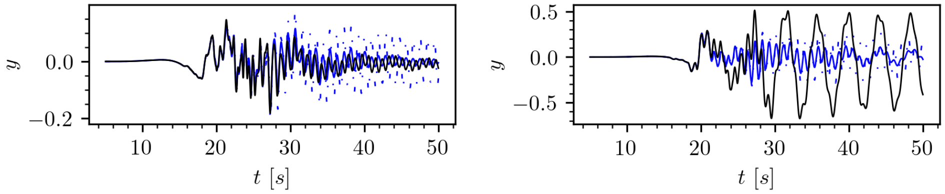

(c) Lateral deflection at mudline

(d) Lateral deflection at tower top

Figure A.6: Equivalently damped linear elastic model time-history to motion 3

A.2 Additional Frequency-Domain Results

The (normalized to the hysteretic response) Fourier transform of the response on linear scale focused up until the first three bending modes is presented in Figures A.7, A.8, and A.9. Throughout the plots, using vertical dotted lines the first few identified bending modes of the reference linear elastic secant stiffness model are indicated (Table 5.2). Here, higher bending modes are significantly underestimated for motion 1 compared to the nonlinear models (amplification peak occurs after vertical dotted lines). The second amplification peak of these nonlinear models consistently occurs after the vertical dotted line. Considering the time-history response of the soil-pile interaction springs one can observe that the response for motion 1 is significantly more influenced by plasticity (Figure 5.9) compared to that of the two other motions. Taking the simplification of a linear (initial) stiffness in computing the eigenproperties of the dynamic system into account, strong plasticity and a strong subsequent degradation in stiffness will lead to stronger deviations in the true dynamic response compared to that of the initial system and cause a shift in resonance frequency. One could say that the (nonlinear) resonance frequency is dependent on the load level.

The bending moment response of the two points of interest is mostly influenced by the second bending mode of the structure for both of the considered points of interest. However, the third bending mode seems to get significantly amplified at tower top and, governing the response for motions 1 and 3. The non-damped models (both linear and nonlinear) all provide larger peak bending moment amplification than the reference models. Except for tower top bending moments due to motion 1. Here the non-damped nonlinear elastic model already underestimates the peak bending moment response close to the third resonance frequency. Apart from this mismatch, the equivalently damped models overall provides a good match in terms of bending moment amplification compared to the hysteretic model. In relation to the deflection spectra the following is observed. Naturally, at tower top amplification is largest (as found in 5.10) and regarding the amplification response at mudline, perfect agreement is found. For the amplification response at tower top, only the second bending mode gets converged towards the hysteretic response. The tower top deflection gets significantly amplified during motion 1, but during motion 3 this happens exactly the other way around: the amplification in the first mode gets significantly reduced. The amplification results of the equivalent linear elastic models show that motion 1 and motion 3 provide a too large reduction in amplification in terms of bending moments at both mudline and tower top. In terms of deflection, it is found that the amplification at tower top is underestimated. This observation is the only observation of significance which is on the contrary with the equivalently damped nonlinear model. Except for the bending moment response to motion 2 where the linear elastic equivalently damped model seems to underestimate the response only slightly. All models without plasticity, are not able to simulate the amount of amplification at tower top around the first resonance frequency. To motion 3, this effect is significant which was already visible during the time-domain results.

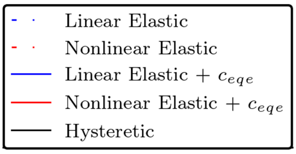

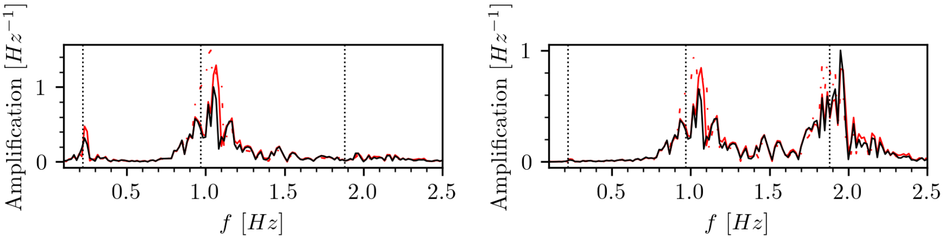

(a) Mudline bending moment, NE

(b) Tower top bending moment, NE

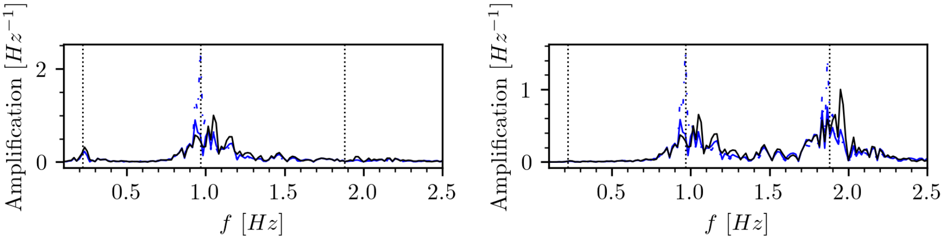

(c) Mudline bending moment, LE

(d) Tower top bending moment, LE

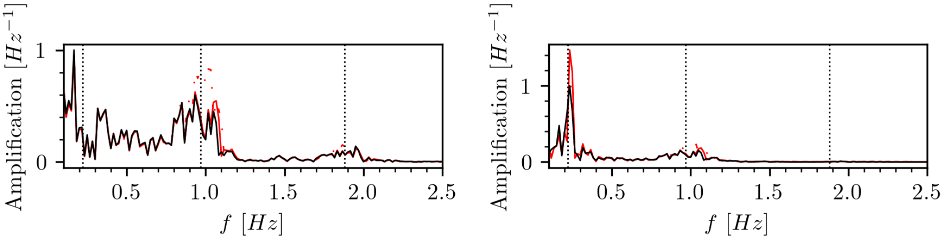

(e) Mudline deflection, NE

(f) Tower top deflection, NE

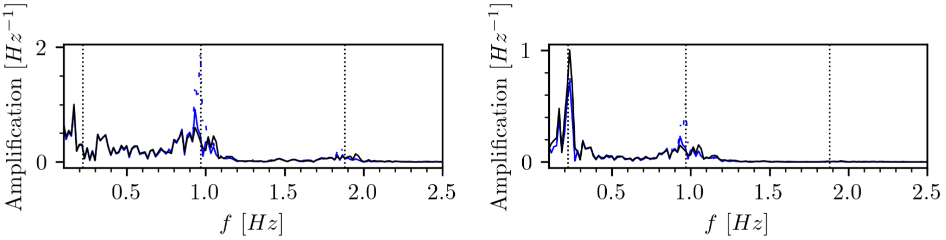

(g) Mudline deflection, LE

(h) Tower top deflection, LE

Figure A.7: Equivalently damped models spectra to motion 1

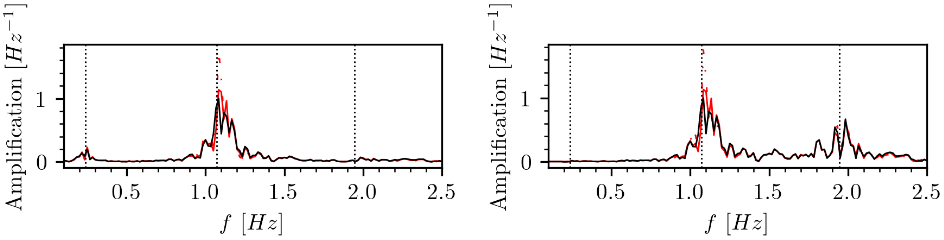

(a) Mudline bending moment, NE (b) Tower top bending moment, NE

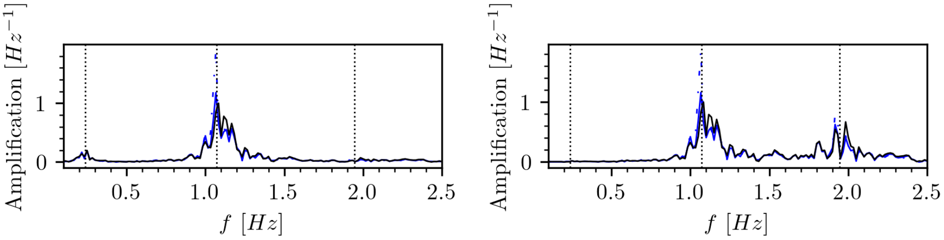

(c) Mudline bending moment, LE (d) Tower top bending moment, LE

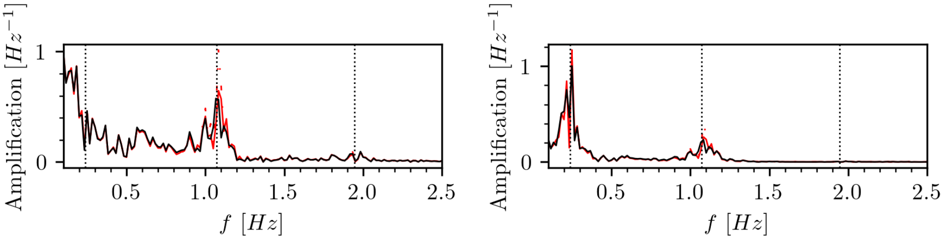

(e) Mudline deflection, NE (f) Tower top deflection, NE

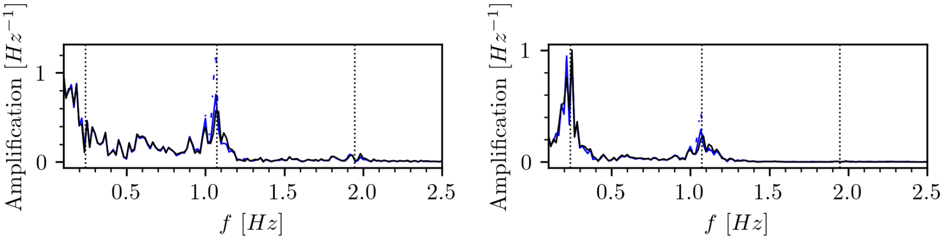

(g) Mudline deflection, LE (h) Tower top deflection, LE

Figure A.8: Equivalently damped models spectra to motion 2

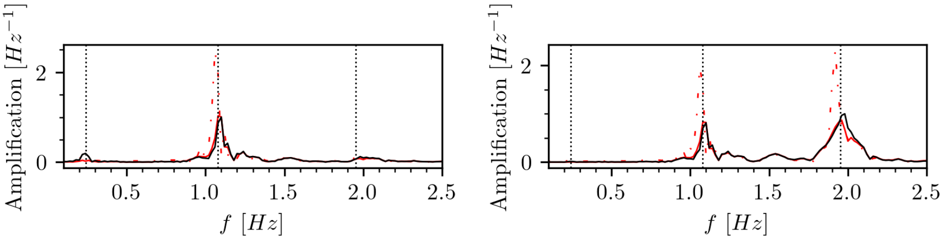

(a) Mudline bending moment, NE

(b) Tower top bending moment, NE

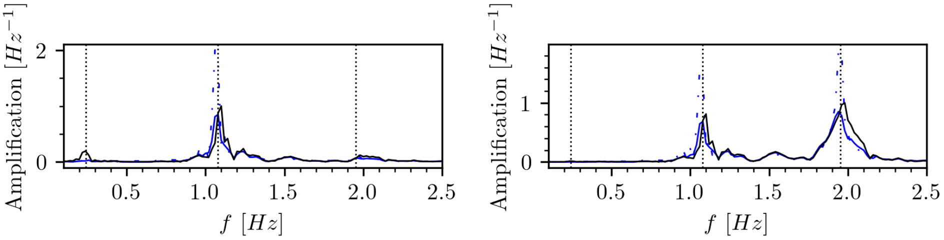

(c) Mudline bending moment, LE

(d) Tower top bending moment, LE

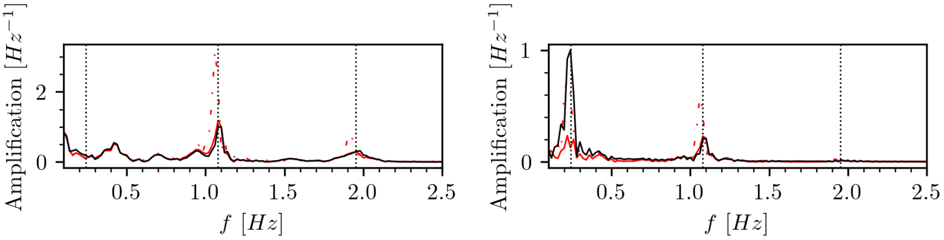

(e) Mudline deflection, NE

(f) Tower top deflection, NE

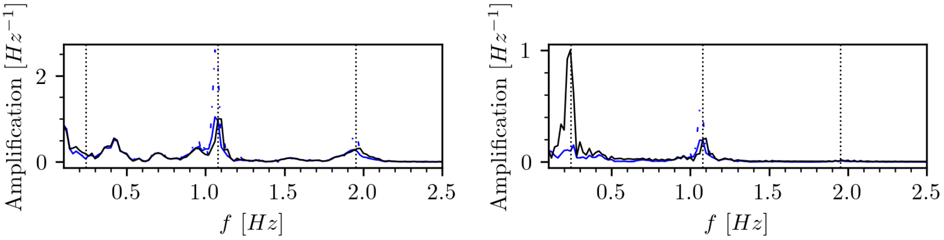

(g) Mudline deflection, LE

(h) Tower top deflection, LE

Figure A.9: Equivalently damped models spectra to motion 3

Appendix B

Equivalent Local Hysteretic Damping: the Practical Approach

For reference purposes, the recommended practice under prescription of DNV [12] for application of foundation damping is adopted. As mentioned in 2.4.4, the soil material damping contribution may be applied in percentage of critical damping. Throughout the seismic response the amount of critical damping to be applied per soil-pile interaction spring ζ_{eqe} is already visualized: Figures 5.8. Gazetas et al. [17] describes the horizontal response of piles in layered soils presenting an approach on derivation of both material (hysteretic) dashpot coefficients and radiation dashpot coefficients. The equivalent dashpot coefficients are related to the soil stiffness, in mechanical formulation represented by the soil-pile interaction springs. An equivalent damper coefficient c is then related to the percentage of critical damping ζ by adopting stiffness proportional damping:

$$c = 2k\frac{\zeta}{\omega} \tag{B.1}$$

The adoption of a damping as described using equation B.1 is in fact a modal damping where the amount of critical damping varies per mode of vibration in oscillatory systems: ζ_i and ω_i. Despite [17] presents the application of equivalent hysteretic damping using a single dashpot at pile head, recommended practice [12] prescribes the application of equivalent dashpots in parallel with the lateral soil-pile interaction springs. The throughout this research developed and adopted algorithm indicates the percentage of critical damping per embedded hysteretic soil-pile interaction element over the course of a total timeseries. Gazetas et al. [17] indicates that the fundamental frequency of the soil column may be applied in B.1 however, in derivation of equation 4.10 forcing frequency is already assumed equal to the natural frequency. On that note, results presented hereafter are presented in adoption of the dominant frequency of the applied signal at bedrock.

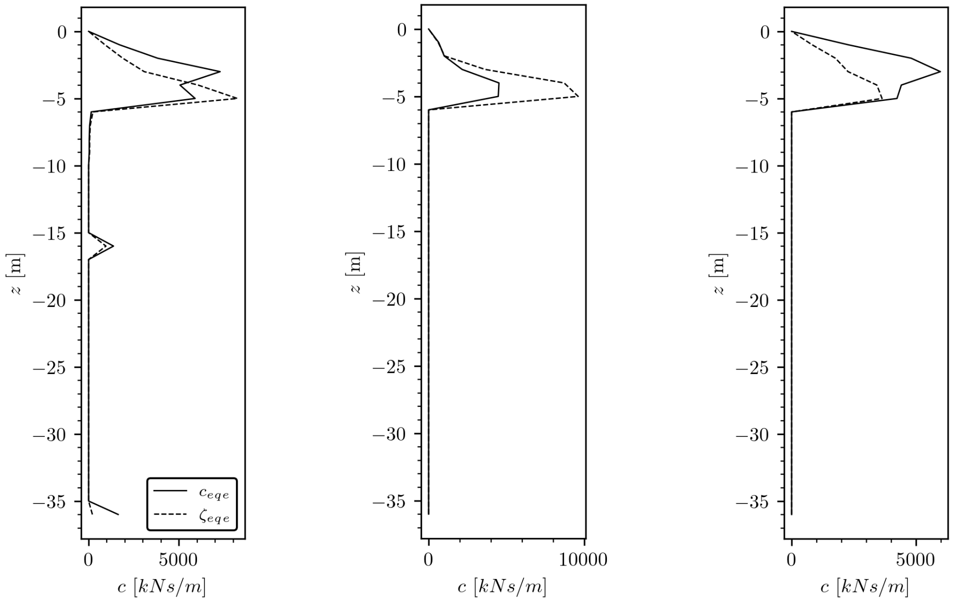

(a) Motion 1 (b) Motion 2 (c) Motion 3

Figure B.1: Equivalent dashpot coefficients

Results in Figure B.1 shows that the computed dashpot coefficients using equation B.1 differ quite substantially over the course of the three different input motions compared to the results according equation 4.13 because the amount of damping to consider is substantially determined by the dominant forcing frequency of the signal applied at bedrock. Comparing Figure B.1 with observations made in Figures 5.11, 5.12, and 5.13 one could argue that the adoption of the practical approach where equivalent damping coefficients are function of input motion soil stiffness yields more desirable results. Equivalent damping in motion 1 is still approximated with similar magnitude, but the equivalent damping to motion 2 and motion 3 is now approximated to be larger and smaller, respectively. In comparison of the observations made earlier in the time-domain results approximated using equation 4.13, better agreement is found in terms of time-domain peak bending moment response along the total structure (Figure B.2), but difference in bending moment amplification at mudline and tower top remains limited (Figure B.3, here Δ indicates the observed difference in amplification):

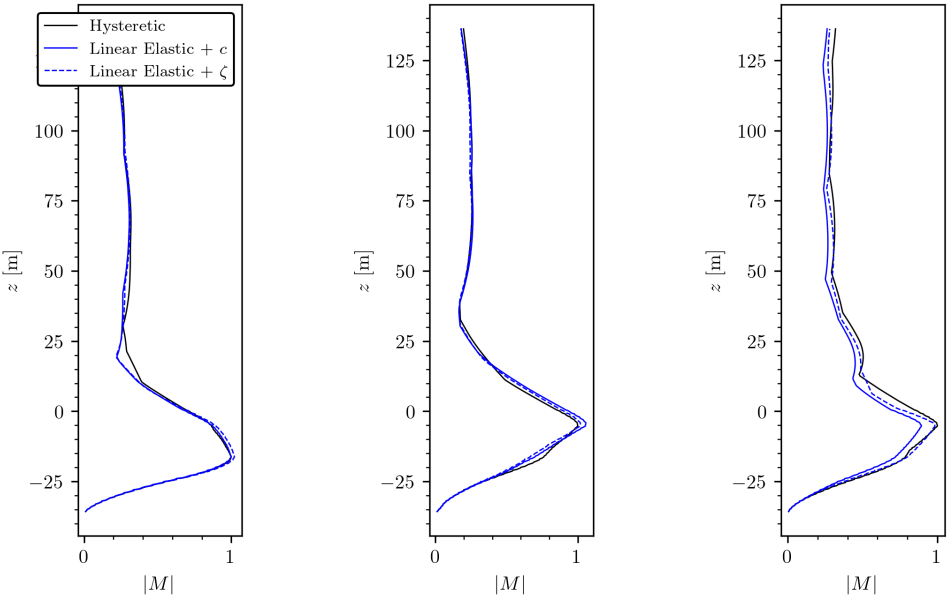

(a) Motion 1 (b) Motion 2 (c) Motion 3

Figure B.2: Peak bending moment response

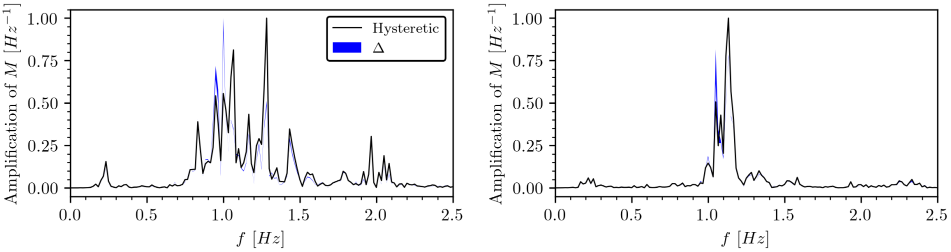

(a) Motion 1, mudline

(b) Motion 2, mudline

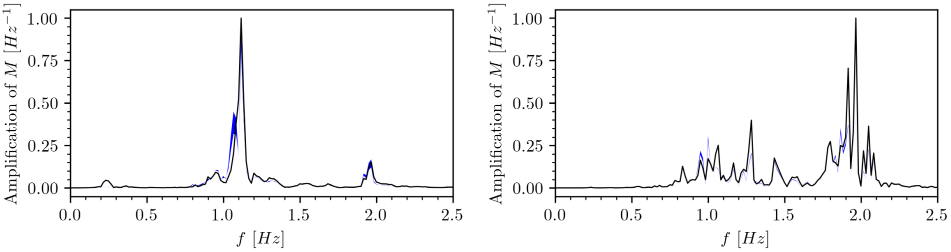

(c) Motion 3, mudline

(d) Motion 1, tower top

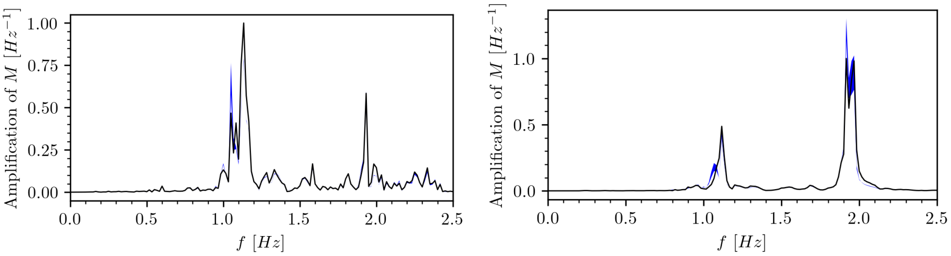

(e) Motion 2, tower top

(f) Motion 3, tower top

Figure B.3: Bending moment amplification

Appendix C

Logarithmic Decrement

In the turbine manufacturing industry, logarithmic decrement damping is frequently used [12]. This time-domain technique is theoretically associated with the free-vibration decay of a single degree of freedom system (2.2.1) and is in fact a linear damping estimation technique. A value for ζ is found under the assumption that the vibration decays according equation 2.5. It directly follows the definition of damping as the decrease in peak amplitude displacement response over time is measured and is limited to one particular frequency at a time. The logarithmic decrement of the displacement response is described by equation C.1:

$$\delta = \frac{1}{n} \ln \left(\frac{A_0}{A_n} \right) \tag{C.1}$$

Here, n depicts the number of peaks, A_0 the initial amplitude, and A_n the amplitude at the last measured peak. Subsequently, an adequate damping ratio is found from the value of logarithmic decrement, equation C.2:

$$\zeta = \frac{1}{\sqrt{1 + \left(\frac{2\pi}{\delta}\right)^2}} \tag{C.2}$$

The identification of damping values is not always as straightforward. The damping ratio is strongly dependent on the logarithmic decrement which in turn is strongly dependent on the amplitude of the free vibration response peaks. Higher initial amplitude possibly results in stronger decrement of the peaks over time. Conclusions must therefore be made with care as the values are strongly dependent on the loading environment. Additionally, in application of a multi degree of freedom system results yield little reliability since nodal response is subjected to excitation in multiple frequencies. Even more so when response is influenced by the nonlinear nature of springs. An attempt is made to apply the same theory to find the % of critical damping for the first two modes of vibration, ζ_1 and ζ_2 of the total structure for the PySimple1 supported hysteretic spring model in an approach which is divergent from the so-called 'rotor-stop' test. To measure the amount of logarithmic decrement in the first bending mode of the structure, the structure is excited at tower top (amplification at tower top is largest in the first bending mode, Figures 5.10) with a single-harmonic force with forcing frequency equal to the first natural frequency of the total structure. After a certain while the load is removed, and subsequent decrement of displacement peaks is measured. The same is done for the second bending mode, which is at a certain height around the "belly" of the structure: $\approx 75m$. At tower top, amplification is strongly dominated around the first natural frequency of the total structure. However, at the belly of the structure, the response amplifies in both the first but predominantly the second resonance frequency. The logarithmic-decrement method is limited to a single frequency so under adoption of a high-pass filter amplification below the second bending mode is filtered.

The logarithmic-decrement method "fits" the amount of damping ζ into a (in amplitude) decreasing timeseries. By taking the mean over all the observed peaks it is found that this fit is not always perfect. A good fit is possible providing the associated displacement level at which the load is removed is still at an acceptable level and a limited amount of peaks is considered. The decrement test is taken and measured over a limited number of 7 peaks and repeated for multiple forcing amplitudes applied at the points of interest. The fitted decrement is related to the observed maximum displacement at mudline as reference value. The maximum obtained time-domain result to the first and second bending mode are presented in Figure C.1.

The total set of observed decay and damping using equations C.1 and C.2 is then visualized in Figure C.2. As such, a displacement-dependent equivalent modal damping is found for the first two bending modes.

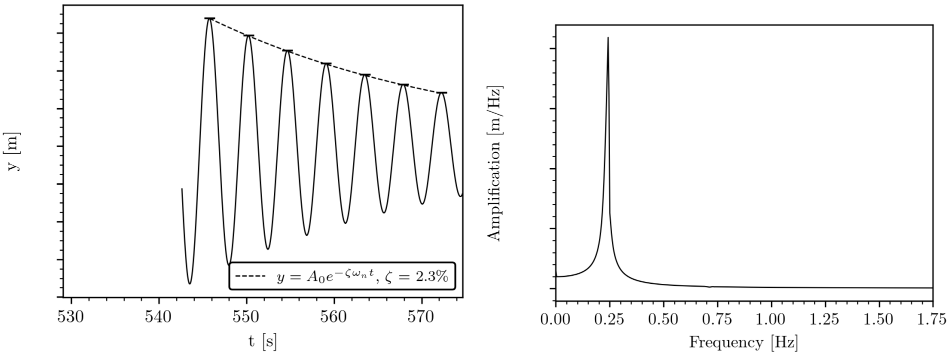

(a) Time-domain decrement at tower top

(b) Frequency domain representation at tower top

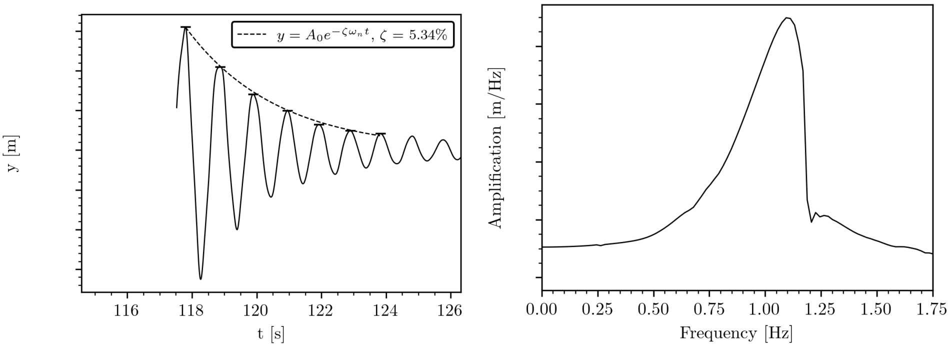

(c) Time domain decrement at ”belly”

(d) Frequency domain representation at ”belly”

Figure C.1: PySimple1 decrement to mode 1 & 2

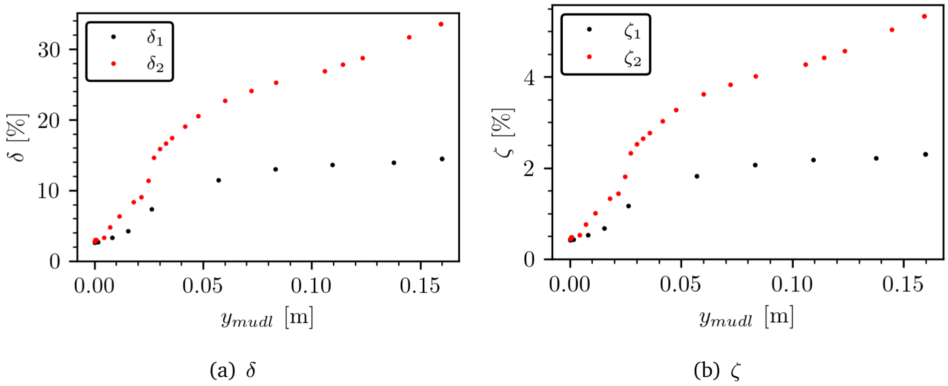

(a) δ (b) ζ

Figure C.2: PySimple1 logarithmic decrement to bending mode 1 & 2

Bibliography

[1] A.C.W.M. Vrouwenvelder. *CT5145 Random Vibrations*. TU Delft, Delft, 2004.

[2] N. Allotey and M.H. El Naggar. A numerical study into lateral cyclic nonlinear soil–pile response. *Canadian Geotechnical Journal*, 45(9):1268–1281, September 2008.

[3] American Petroleum Institute. Recommended Practice for Planning, Designing and Constructing Fixed Offshore Platforms—Working Stress Design, 2007.

[4] W.J.A.P. Beuckelaers. *Numerical Modelling of Laterally Loaded Piles for Offshore Wind Turbines*. PhD thesis, University of Oxford, 2017.

[5] R.W. Boulanger, C.J. Curras, B.L. Kutter, D.W. Wilson, and A. Abghari. Seismic Soil-Pile-Structure Interaction Experiments and Analyses. *Journal of Geotechnical and Geoenvironmental Engineering*, 125(9):750–759, September 1999.

[6] T Bouman. A Winkler Model for the Seismic Analysis of Monopile Foundations. Master's thesis, TU Delft, Delft, 2018.

[7] B.W. Byrne. PISA: New Design Methods for Offshore Wind Turbine Monopiles. In *Smarter Solutions for Future Offshore Developments*. Society for Underwater Technology, 2017.

[8] W. Carswell. *Soil-Structure Modeling and Design Considerations for Offshore Wind Turbine Monopile Foundations*. PhD thesis, University of Massachusetts Amherst, 2015.

[9] S. Corciulo, O. Zanoli, and F. Pisanò. Supporting the Engineering Analysis of Offshore Wind Turbines Through Advanced Soil-Structure 3D Modelling. In *Volume 9: Offshore Geotechnics; Torgeir Moan Honoring Symposium*, Trondheim, Norway, June 2017. American Society of Mechanical Engineers.

[10] M. Damgaard, V. Zania, L.V Andersen, and L.B. Ibsen. Effects of soil–structure interaction on real time dynamic response of offshore wind turbines on monopiles. *Engineering Structures*, 75:388–401, September 2014.

[11] R. De Risi, S. Bhattacharya, and K. Goda. Seismic performance assessment of monopile-supported offshore wind turbines using unscaled natural earthquake records. *Soil Dynamics and Earthquake Engineering*, 109:154–172, June 2018.

[12] Det Norske Veritas DNV. Dnv-rp-0585 recommended practice: Seismic design of wind power plants, 2021.

[13] L.D. Dilas. Estimation of Soil Damping Contribution on Offshore Monopiles Using Plaxis 3D Approach. Master's thesis, TU Delft, Delft, 2018.

[14] Y. Dong, N. Lu, and J.S. McCartney. Scaling Shear Modulus from Small to Finite Strain for Unsaturated Soils. *Journal of Geotechnical and Geoenvironmental Engineering*, 144(2), February 2018.

[15] J.D. Dowgala. *Detecting and Quantifying Damage in Buildings Using Earthquake Response Data and Capacity Curves*. PhD thesis, Purdue University, West Lafayette, Indiana, 2013.

[16] EduPro Civil Systems, Inc. ProShake: Ground Response Analysis Program, 2017.

[17] G. Gazetas and R. Dobry. Horizontal Response of Piles in Layered Soils. 1984.

[18] G. Gazetas and R. Dobry. Simple Radiation Damping Model for Piles and Footings. *Journal of Engineering Mechanics*, 110(6):937–956, June 1984.

[19] T. Heitz, C. Giry, B. Richard, and F. Ragueneau. How Are the Equivalent Damping Ratios Modified by Nonlinear Engineering Demand Parameters? In *Proceedings of the 6th International Conference on Computational Methods in Structural Dynamics and Earthquake Engineering (COMPDYN 2015)*, pages 2362–2380, Rhodes Island, Greece, 2017. Institute of Structural Analysis and Antiseismic Research School of Civil Engineering National Technical University of Athens (NTUA) Greece.

[20] J. R. Hutchinson. Shear Coefficients for Timoshenko Beam Theory. *Journal of Applied Mechanics*, 68(1):87–92, January 2001.

[21] W. D. Iwan. On a Class of Models for the Yielding Behavior of Continuous and Composite Systems. *Journal of Applied Mechanics*, 34(3):612–617, September 1967.

[22] L.S. Jacobsen. Damping in Composite Structures. In *Proceedings of the 2nd World Conference on Earthquake Engineering*, pages 1029–1044, 1960.

[23] T. Kagawa and L.M. Kraft. Lateral Load-Deflection Relationships of Piles Subjected to Dynamic Loadings. *Soils and Foundations*, 20(4):19–36, December 1980.

[24] D. Kallehave, B.W. Byrne, C.L. Thilsted, and K.K. Mikkelsen. Optimization of monopiles for offshore wind turbines. *Philosophical Transactions of the Royal Society A: Mathematical, Physical and Engineering Sciences*, 373(2035), February 2015.

[25] E. Kausel and D. Assimaki. Seismic Simulation of Inelastic Soils via Frequency-Dependent Moduli and Damping. *Journal of Engineering Mechanics*, 128(1):34–47, January 2002.

[26] A.M. Kaynia. Seismic considerations in design of offshore wind turbines. *Soil Dynamics and Earthquake Engineering*, 124:399–407, September 2019.

[27] R.A. Kjørlaug and A.M. Kaynia. Vertical earthquake response of megawatt-sized wind turbine with soil-structure interaction effects: Vertical Response of a Megawatt-Sized Wind Turbine. *Earthquake Engineering & Structural Dynamics*, 44(13):2341–2358, October 2015.

[28] R.A. Kjørlaug, A.M. Kaynia, A. Elgamal, and N. As. Seismic Response of Wind Turbines due to Earthquake and Wind Loading. 2014.

[29] A. Malekjafarian, S. Jalilvand, P. Doherty, and D. Igoe. Foundation damping for monopile supported offshore wind turbines: A review. *Marine Structures*, 77, May 2021.

[30] H. Matlock. Correlations for Design of Laterally Loaded Piles in Soft Clay. Dallas, 1970.

[31] S. Mazzoni, McKenna, F., M. H. Scott, and Fenves, G. L. *OpenSees Command Language Manual*. University of California, Berkeley, Berkeley, 2006.

[32] M.M. Memarpour, M. Kimiaei, and M. Shayanfar. Simplified numerical model for analysis of offshore piles under cyclic lateral loading. 2011.

[33] M.M. Memarpour, M. Kimiaei, M. Shayanfar, and M. Khanzadi. Cyclic lateral response of pile foundations in offshore platforms. *Computers and Geotechnics*, 42:180–192, May 2012.

[34] A.V. Metrikine. *Dynamics, Slender Structures and an Introduction to Continuum Mechanics CT 4145*. Delft.

[35] M.L.R. Gonzalez. Seismic Analysis on Monopile Based Offshore Wind Turbines Including Aero-Elasticity and Soil-Structure Interaction. Master's thesis, TU Delft, Delft, July 2016.

[36] C. Phillips and Y.M.A. Hashash. Damping formulation for nonlinear 1D site response analyses. *Soil Dynamics and Earthquake Engineering*, 29(7):1143–1158, July 2009.

[37] C.A. Phillips. *Dynamic Soil Modeling in Site Response and Soil-Large Pile Interaction Analysis*. PhD thesis, Urbana, Illinois, 2012.

[38] R. M. Pyke. Closure to “Nonlinear Soil Models for Irregular Cyclic Loadings”. *Journal of the Geotechnical Engineering Division*, 106(11):1281–1282, November 1980.

[39] A. Rahmani, M. Taiebat, L.W.D. Finn, and C.E. Ventura. Evaluation of p-y Curves Used in Practice for Seismic Analysis of Soil-Pile Interaction. In *Geo-Congress 2012*, pages 1780–1788, Oakland, California, United States, March 2012. American Society of Civil Engineers.

[40] A. Rahmani, M. Taiebat, L.W.D. Finn, and C.E. Ventura. Evaluation of p-y springs for nonlinear static and seismic soil-pile interaction analysis under lateral loading. *Soil Dynamics and Earthquake Engineering*, 115:438–447, December 2018.

[41] A. Rahmani, M. Taiebat, W.D.L. Finn, and C.E. Ventura. Determination of Dynamic p-y Curves for Pile Foundations Under Seismic Loading. 2012.

[42] L.C. Reese and W.F. van Impe. *Single piles and pile groups under lateral loading*. 2nd edition, 2011.

[43] J. Simon. Parameter identification for dynamic analysis of pile foundation using non- linear p-y method. In *Second Conference of Junior Researchers in Civil Engineering*. BME, Department of Structural Engineering.

[44] B. Stuyts. Revised Soil Damping Using Realistic Pile-Soil Interaction Models. 2022.

[45] S.K. Suryasentana and B.M. Lehane. Updated CPT-basedp – y formulation for laterally loaded piles in cohesionless soil under static loading. *Géotechnique*, 66(6):445–453, June 2016.

[46] D.M.G. Taborda, D.M. Potts, and L. Zdravković. On the assessment of energy dissipated through hysteresis in finite element analysis. *Computers and Geotechnics*, 71:180–194, January 2016.

[47] A. Tsouvalas. *CIE5260 Structural Response to Earthquakes*. TU Delft, Delft, 2020.

[48] B.J. Turner, S.J. Brandenberg, and J.P. Stewart. Influence of Kinematic SSI on Foundation Input Motions for Bridges on Deep Foundations. November 2017.

[49] R.P. Verlinde. Capturing 3D Continuum Effects in a 1D Soil-Structure Interaction Model for Seismic Analysis of Offshore Wind Turbines. Master's thesis, TU Delft, Delft, 2019.

[50] W.G. Versteijlen. Estimation of the Vibration Decrement of an Offshore Wind Turbine Support Structure Caused by its Interaction with Soil. Master's thesis, TU Delft, Delft, 2011.

[51] W.G. Versteijlen. *Identification of effective 1D soil models for large-diameter offshore wind turbine foundations based on in-situ seismic measurements and 3D modelling*. PhD thesis, Delft University of Technology, 2018.

[52] M Vucetic and R Dobry. Effect of Soil Plasticity on Cyclic Response. *Journal of Geotechnical Engineering*, 1991.

[53] L. Wang and T. Ishihara. New p-y model for seismic loading prediction of pile foundations in non-liquefiable and liquefiable soils considering modulus reduction and damping curves. *Soils and Foundations*, 62(5), October 2022.

[54] L. Wang and T. Ishihara. A semi-analytical one-dimensional model for offshore pile foundations considering effects of pile diameter and aspect ratio. *Ocean Engineering*, 250, April 2022.

[55] S. Yniesta and S.J. Brandenberg. Unloading-Reloading Rule for Nonlinear Site Response Analysis. 2015.

[56] N. Yoshida. DYNEQ: A computer program for DYNamic response analysis of level ground by EQuivalent linear method, 2020.

[57] N. Yoshida, S. Kobayashi, I. Suetomi, and K. Miura. Equivalent linear method considering frequency dependent characteristics of stiffness and damping. *Soil Dynamics and Earthquake Engineering*, 22(3):205–222, April 2002.

[58] J. Zhang, R.D. Andrus, and C.H. Juang. Normalized Shear Modulus and Material Damping Ratio Relationships. 2005.

[59] Q. Zhang, Y. Zhang, H. Lin, and L. Feng. Numerical investigation on bearing capacity of OWT foundation with large diameter monopile under Seismic load. *Applied Ocean Research*, 108, March 2021.

[60] Y. Zhang, K.K. Aamodt, and A.M. Kaynia. Hysteretic damping model for laterally loaded piles. *Marine Structures*, 76, March 2021.

[61] Y. Zhang, K.H. Andersen, P. Jeanjean, A. Mirdamadi, A.S. Gundersen, and H.P. Jostad. A Framework for Cyclic p-y Curves in Clay and Application to Pile Design in GoM. In *Offshore Site Investigation Geotechnics 8th International Conference Proceedings*, pages 431–440. Society of Underwater Technology, January 2017.

TU Delft Delft University of Technology

SIEMENS Gamesa RENEWABLE ENERGY